

**AD 50150**

# **Armed Services Technical Information Agency**

**Reproduced by  
DOCUMENT SERVICE CENTER  
KNOTT BUILDING, DAYTON, 2, OHIO**

Because of our limited supply, you are requested to  
RETURN THIS COPY WHEN IT HAS SERVED YOUR PURPOSE  
so that it may be made available to other requesters.  
Your cooperation will be appreciated.

**NOTICE: WHEN GOVERNMENT OR OTHER DRAWINGS, SPECIFICATIONS OR OTHER DATA  
ARE USED FOR ANY PURPOSE OTHER THAN IN CONNECTION WITH A DEFINITELY RELATED  
GOVERNMENT PROCUREMENT OPERATION, THE U. S. GOVERNMENT THEREBY INCURS  
NO RESPONSIBILITY, NOR ANY OBLIGATION WHATSOEVER; AND THE FACT THAT THE  
GOVERNMENT MAY HAVE FORMULATED, FURNISHED, OR IN ANY WAY SUPPLIED THE  
SAID DRAWINGS, SPECIFICATIONS, OR OTHER DATA IS NOT TO BE REGARDED BY  
IMPLICATION OR OTHERWISE AS IN ANY MANNER LICENSING THE HOLDER OR ANY OTHER  
PERSON OR CORPORATION, OR CONVEYING ANY RIGHTS OR PERMISSION TO MANUFACTURE,  
USE OR SELL ANY PATENTED INVENTION THAT MAY IN ANY WAY BE RELATED THERETO.**

**UNCLASSIFIED**

*FC*

AD No. 60700  
ASTIA FILE COPY

OFFICE OF NAVAL RESEARCH  
CONTRACT N50RI-76 PROJECT ORDER **X**

---

NR-014-903

TECHNICAL MEMORANDUM  
NO. 34

THEORY AND DESIGN OF AN END-FIRE  
DIRECTIVE SOUND SOURCE

BY  
MIGUEL C. JUNGER  
SEPTEMBER 21, 1954

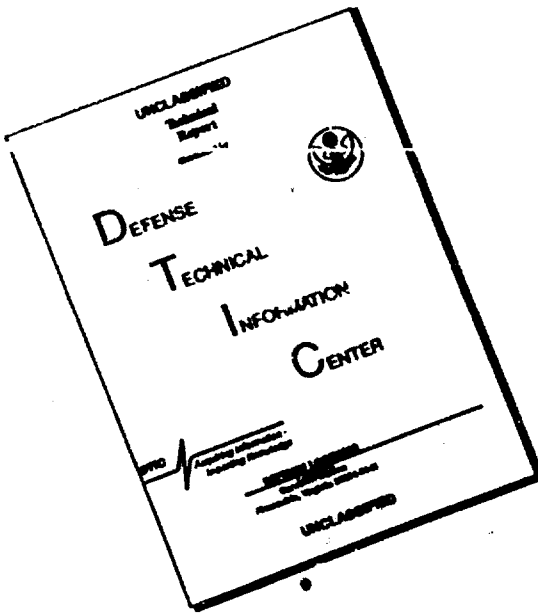
*60150*

---

---

ACOUSTICS RESEARCH LABORATORY  
DIVISION OF APPLIED SCIENCE  
HARVARD UNIVERSITY-CAMBRIDGE, MASSACHUSETTS

# **DISCLAIMER NOTICE**



**THIS DOCUMENT IS BEST  
QUALITY AVAILABLE. THE COPY  
FURNISHED TO DTIC CONTAINED  
A SIGNIFICANT NUMBER OF  
PAGES WHICH DO NOT  
REPRODUCE LEGIBLY.**

Office of Naval Research

Contract N5ori-76

Project Order X

---

---

Technical Memorandum No. 34

Theory and Design of an End-Fire Directive Sound Source

by

Miguel C. Junger

September 21, 1954

Abstract

A radially pulsating cylindrical sound source gives rise to broadside radiation if all its elements move in phase. However, when a progressive phase shift between elements along the cylinder is introduced (by means of waves propagating along the cylinder, or of standing waves), the radiation can be "steered." When the phase velocity of these waves is equal to the sound velocity in the surrounding medium the radiation pattern resembles that of an end-fire directive array of point sources. The high directivity thus achieved is independent of the ratio of source diameter to wavelength and, over a large range, of frequency. Experimental results verifying the mathematical analysis are presented. High directivity can also be achieved by means of a battery of staggered, partly occluded, cylindrical sources with a phase velocity half that of sound. Another advantage of the source is that its radiating surface area can be conveniently made much larger than that of a piston-type source. In practice for use under water, this source may be in the form of an elastic rod or shell, or of a mass- or stiffness-controlled hose filled with a fluid under pressure (in order to prevent cavitation at the transducer surface). Comparing the merits of these different approaches to the design of a low-frequency source producing an end-fire directive, frequency-independent directivity pattern (over the operating range), it is found that the most interesting one is the mass-controlled hose filled with sea water.

---

---

Acoustics Research Laboratory

Division of Applied Science

Harvard University, Cambridge, Massachusetts

Table of Contents

Principal Symbols Used.....	i
Chapter I: General Features of the End-Fire Source.....	1
Description.....	1
Advantages .....	2
Qualitative description of the operating principle of the end-fire source.....	4
Chapter II: Theory of the End-Fire Source: Parameters Determining the Directivity Pattern.....	7
Analysis of the travelling-wave source.....	7
Analysis of the standing-wave source.....	11
An end-fire source in the form of a battery of partly occluded cylinders.....	14
Chapter III: Experimental Verification of the Theory	
Nature of the experiments.....	23
Description of the experimental end-fire source.....	23
Instrumentation .....	25
Observed directivity patterns.....	26
Discussion of experimental results.....	27
Chapter IV: Design of an End-Fire Source for Use under Water.....	30
Nature of the design problem .....	30
Solid cylindrical rods.....	31
Cylindrical shells.....	34
The stiffness-controlled hose.....	36
The mass-controlled hose.....	46
Summary: Comparison of the designs.....	50
Appendix: Analysis of the End-Fire Source Problem by Means of the Green's Function.....	53
Statement of the problem.....	53
Derivation of the Green's function.....	53
Evaluation of the distant field .....	60
Bibliography.....	63

## Principal Symbols Used

(N. B.: Other symbols are defined in the Text.)

$a$	radius of cylinder
$c_b$	$\sqrt{E/\rho_b}$ , bar velocity ( $\rho_b$ is the density of the bar material)
$c_i$	phase velocity of axially symmetrical waves propagating in the direction of the cylindrical axis
$c_o$	sound velocity of surrounding medium
$c_s$	sound velocity of the fluid in the fluid-filled hose (equal to $c_i$ when the hose wall is infinitely rigid or massive)
$c_w$	$\sqrt{\frac{E}{\rho_w(1-\nu^2)}}$ , longitudinal wave velocity in an elastic plate (or wall of cylindrical shell) at low frequencies
$c_z$	$= c_i$
$E$	Young's modulus
$E_r$	total radiated power
$E_s$	total power lost by cylindrical source
$f$	frequency
$h$	half-thickness of hose or shell wall
$j$	$-\sqrt{-1}$
$k_i, k_o, k_z$	$\omega/c_i, \omega/c_o, \omega/c_z$ , wave numbers
$L$	length of cylindrical source
$n$	$L/\lambda_i$ , length of source measured in wave lengths
$p(\bar{R})$	sound pressure
$r$	mass ratio of helium to air in gaseous mixture
$\bar{R}$	space vector

$R, \theta$	spherical coordinates
$r, \phi, z$	cylindrical coordinates
$S$	p/u stiffness of hose wall
$t$	time
$\dot{u}$	radial velocity of cylindrical surface
$u, v$	radial and axial displacements of cylindrical surface, respectively
$U$	amplitude of radial displacement of a surface element at the driving end of the cylindrical source (i.e., at $z = 0$ )
$\dot{V}(z)$	strain energy flow through the cylindrical cross section located at $z$
$\dot{W}(z)$	fluid energy flow through the cylindrical cross section located at $z$
$x_w$	specific reactance of hose wall
$z_w$	specific impedance of tube wall
$\delta_1(x)$	$\tan^{-1} \left[ \frac{J_1(x)}{N_1(x)} \right]$
$\lambda_i, \lambda_o$	$c_i/f, c_o/f$ , wave lengths
$\mu$	logarithmic decrement per wave length of a wave travelling along the cylindrical surface
$\nu$	Poisson's ratio
$\rho_i, \rho_o, \rho_w$	density of fluid in fluid-filled hose, of surrounding medium, and of hose wall, respectively
$\psi$	phase angle defined in Eqs. (II. 26)
$\Psi(R)$	velocity potential
$\omega$	circular frequency

Definition of certain functions

Bessel and related functions

$J_m(y)$       Bessel function of order  $m$

$N_m(y)$  Neumann function of order  $m$

$H_m^{(2)}(y)$   $J_m(y) - jN_m(y)$ , Hankel function of the second kind

$J'_m(y)$ , etc.  $\frac{dJ_m(y)}{dy}$ , etc.

Dirac delta-function  $\delta(y-y')$ :

$$\int_{-\infty}^{\infty} F(y') \delta(y-y') dy' = F(y)$$

Fourier Transform:

$$F(\zeta) = \int_{-\infty}^{\infty} f(z) e^{j\zeta z} dz$$

Inverse Fourier Transform:

$$f(z) = \frac{1}{2\pi} \int_{-\infty}^{\infty} F(\zeta) e^{-j\zeta z} d\zeta$$

**THEORY AND DESIGN OF AN END-FIRE DIRECTIVE SOUND SOURCE**

by

Miguel C. Junger

Acoustics Research Laboratory, Harvard University  
Cambridge, Massachusetts

**Chapter I**

**General Features of the End-Fire Source**

**Description**

The end-fire source is in the form of a long cylinder which radiates sound energy into the surrounding medium by means of axially symmetrical waves travelling in the direction of its axis. These waves are generated by a transducer injecting energy into the cylinder at one of its ends (cf. Fig. I.1) and are attenuated as they progress by the effects of acoustic radiation. Another form of this source utilizes attenuated standing waves (cf. Fig. I.2). The essential difference between the end-fire source and the conventional piston-type source is this: In the latter, the directivity pattern is determined entirely by the ratio of source diameter to wavelength. There is thus a lack of flexibility which gives the designer very little freedom, and which imposes a strong frequency dependence on the performance of the source. The end-fire source, on the contrary, has a directivity pattern which depends on three parameters: (1) the ratio of the phase velocity  $c_i$  of the travelling waves to the sound velocity  $c_0$  in the surrounding medium, (2) the attenuation  $\mu$  per wave length of the waves on the cylindrical surface, (3) the length  $n$  of the cylinder measured in wave lengths, (i.e., the ratio  $L/\lambda_i$ ). The former two parameters depend only indirectly on the frequency and the source diameter. As to the third parameter, it defines a frequency dependence only in so far as the source must measure a minimum number of wavelengths; hence, the frequency dependence is limited to the statement of a lower limit, determined by the actual length of the source,

below which the source does not operate efficiently. The designer has therefore greater control over the performance of the source, and considerable freedom in obtaining the desired directivity patterns without being hampered by frequency and source diameter requirements.

Having determined the functional relation between the three above-mentioned parameters ( $c_i/c_o, \mu$ , and  $n$ ) and the directivity pattern, the engineering problem to be solved is essentially how to generate most practically surface waves fulfilling the conditions which result in the desired directivity pattern. This technical memorandum presents (1) the theoretical analysis of the functional relation between the system parameters and the directivity pattern. (Chap. II and Appendix); (2) experimental results verifying these theoretical conclusions (Chap. III); and (3) a preliminary investigation of practical designs for use in water (Chap. IV). For the latter purpose the most promising design is in the form of a water filled, pressurized hose, made of a flexible, strong material; the hose would measure approximately twenty wavelengths, and its diameter would be a small fraction of a wavelength. Pressure waves injected at the driving end propagate along the fluid column. Owing to the finite impedance of the hose wall, these pressure waves are associated with axially symmetrical ripples progressing along the hose.

#### Advantages

The greater flexibility of performance of the end-fire source results in three specific advantages over the piston-type source. The most important one is that high end-fire directivity can be achieved even when the diameter of generator and cylinder are but a small fraction of a wavelength, provided the three controlling parameters fulfill certain conditions. This feature is of great interest if it is desired to propagate sound energy over great ranges under water. For this purpose, low-frequency sound waves are preferable, since they are absorbed to a lesser extent than high-frequency waves, absorption being in general proportional to the square of the frequency. However, little is gained by using a non-directive low-frequency source because the sound wave is, in this case, attenuated by geometric spreading. Since a narrow sound beam is produced by a piston-type source only if the source diameter measures at least two wavelengths, these sources can be

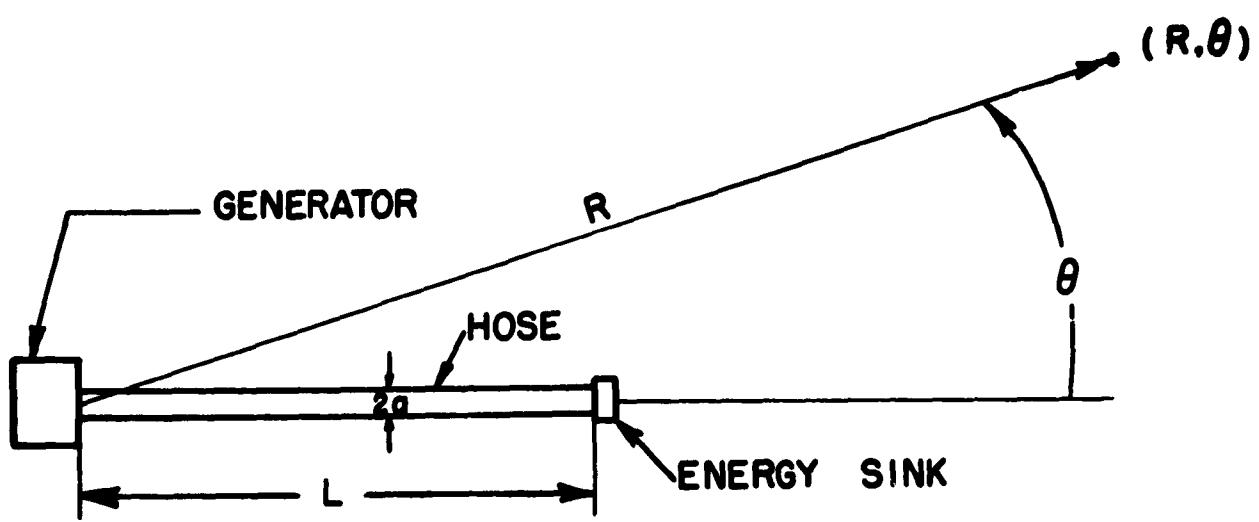


Fig. I.1. Elements of the end-fire source terminated by an energy sink, (i.e., using traveling waves).

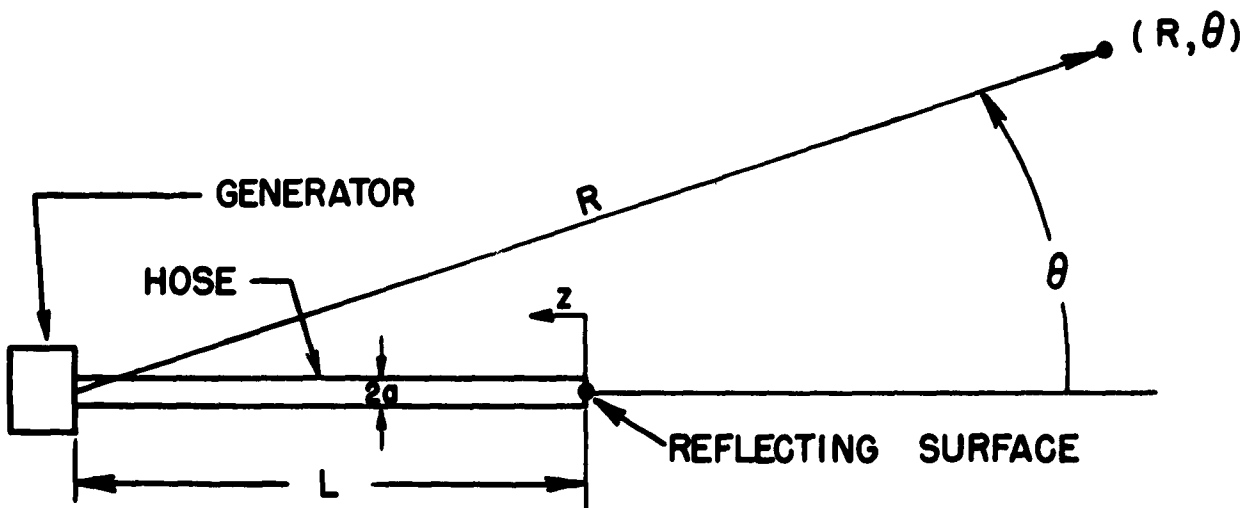


Fig. I.2. Elements of the end-fire source terminated by a reflecting surface (i.e., using standing waves).

adapted to low-frequency use only when their diameter is increased accordingly. It can be verified immediately that even for moderately low frequencies the dimensions of a piston-type source are prohibitively large. The most important practical advantage of the end-fire source is therefore the feature mentioned above, viz., that contrariwise to the piston-type source, it permits low-frequency sound energy to be radiated in a narrow beam with a source diameter of only a fraction of a wavelength. For that purpose, the characteristic parameters of the source must fulfill the following conditions: (a) The phase velocity  $c_i$  of the pressure waves must be approximately equal to the sound velocity  $c_o$  in the surrounding medium. (b) The attenuation per wavelength  $\mu$  must be relatively small. (c) The length  $n$  of the hose measured in wavelengths must exceed a certain minimum quantity which is determined by  $\mu$ . (For example, when  $\mu$  is 8 per cent, the source length should be of the order of 20 wavelengths.) Nothing is gained by using a source length greater than this optimal number of wavelengths.

Requirement (a) can be circumvented by using, instead of a single cylinder, a battery of cylinders displaying the proper phase shifts in space and time and using propagating waves such that  $c_i = 1/2 c_o$ , instead of  $c_i = c_o$ , as for the single cylinder (cf. Chap. II). This is, however, a cumbersome arrangement and one of the principal aims of the designer will probably be to achieve condition (a) in a single cylinder source. Having complied with this condition, an almost arbitrary degree of end-fire directivity can be achieved by raising requirements (b) and (c), i.e., by decreasing the attenuation and increasing the source length in proportion. This process is only limited by attenuation from internal friction and viscous losses. It should be added that requirement (a) may be modified if, instead of a highly directive pencil-shaped beam, a directivity pattern in the form of two symmetrical prongs is desired (cf. Fig. II.4); the condition required for this purpose is that  $c_i$  be slightly larger than  $c_o$ .

The second advantage of the end-fire source is that, for the proper design, its directivity pattern is essentially frequency-independent over large frequency ranges. This is in contrast with the performance of the piston-type source whose directivity pattern is determined by the ratio of

source diameter to wavelength. Any appreciable change in frequency will therefore alter the pattern radiated. In the end-fire source, a change in frequency affects the pattern only indirectly, through the three controlling parameters ( $c_1/c_0$ ,  $\mu$  and  $n$ ). The restriction on the quantity  $n$  imposes a lower frequency limit on the range of frequencies over which the source can be used. For frequencies larger than the minimum frequency, frequency independence can be achieved: Neglecting viscous and other frictional losses (which are small compared to the loss by sound radiation),  $\mu$  is essentially frequency-independent. If the same is to hold for the parameter  $c_1/c_0$ , one must use for propagation along the cylinder a type of wave whose dispersion curve is flat in the intended operating range of the end-fire source. Several types of wave propagation in elastic rods, in the walls of hollow, cylindrical shells, and in mass- and stiffness-controlled fluid-filled hoses are discussed in Chapter IV. The fluid-filled hose seems to be the most practical possibility.

Another advantage of the end-fire source is that it permits the application of measures inhibiting cavitation, and thus constitutes a convenient outlet for powerful transducers. If the fluid-filled hose design is used, the water in the hose can be placed under considerable hydrostatic pressure to retard the onset of cavitation in the vicinity of the transducer. Cavitation at the cylindrical surface radiating into the ambient medium is not a serious problem, because the area available for transfer of sound energy is, in general, much greater than the area of any practical piston-type source. By selecting a hose wall having a sufficiently large reactance the amplitude of the most intense surface waves, in the vicinity of the transducer, can be kept below the cavitation level. If cavitation does occur in this region, the effective length of the source will merely have been reduced by the length of this region, which is shielded from the ambient medium by a pressure release surface of cavitation bubbles.

Qualitative Description of the  
Operating Principle of the End-Fire Source

Having thus described the general features of the end-fire source, it seems desirable to give a qualitative description of its working principle, which is analyzed in detail and rather rigorously in the next chapter. Con-

sider an infinitely long cylindrical surface whose entire surface is covered by axially symmetrical waves travelling with a phase velocity  $c_i$ . When this velocity is extremely large, great segments of the cylinder move in phase; each of these segments radiates sound energy in the fashion of a long uniformly pulsating, cylindrical surface, i.e., radially outward<sup>1</sup> [cf. Fig. I.3(1)].

If the phase velocity  $c_i$  is reduced until it is of the same order of magnitude but larger than the sound velocity  $c_o$ , the outgoing waves progress in a direction having a component along the cylindrical axis. Wave fronts travelling in the direction of propagation are spaced at intervals  $\lambda_o = c_o/f$ ; the traces of these wave fronts on the cylindrical surface must match the waves travelling along this surface, which are spaced at intervals  $\lambda_i = c_i/f$ . This matching can only occur when the direction of propagation makes an angle  $\cos^{-1}(c_o/c_i)$  with the cylindrical axis.<sup>2</sup> The outgoing waves thus propagate in directions which form a conical surface having this vertex angle. If sound is radiated from the cylindrical surplus by means of standing instead of travelling waves, there are of course two such cones (cf. Fig. I.3 (2)). The trace of such a conical wave in the horizontal plane forms the two prongs mentioned above as being characteristic of directivity patterns for the condition  $c_i/c_o > 1$ .

When this ratio is allowed to become unity, the vertex angle of the cone vanishes and the conical waves degenerate into a system of plane waves traveling along the cylindrical axis (cf. Fig. I.3 (3)).<sup>3</sup> The two prongs of the preceding case have merged into one. This is the condition for end-fire directivity of the finite end-fire source. For the infinite cylinder, the radial intensity gradient grows steadily as the ratio  $c_i/c_o$  is varied from unity to

<sup>1</sup>Figure (I.3) as well as the general line of thought in the remainder of this chapter are taken from reference (1), where this problem is considered in detail.

<sup>2</sup>The same reasoning applies when analyzing the well-known problem of flexural waves excited in an elastic plate by an obliquely incident sound wave; cf., for example, reference (2).

<sup>3</sup>The wave fronts of these waves are plane, but they differ from ordinary plane waves in that their intensity decreases rapidly as one moves radially outward from the cylindrical boundary. They thus resemble Rayleigh surface waves; the similarity is heightened by the fact that the fluid particle displacements is elliptical for  $c_i < c_o$ ; this, of course, is also the case for the Rayleigh waves (cf., for example, reference (3), p. 21).

zero, thus suggesting an increase of end-fire directivity. In this range, the similarity between the infinite and the finite cylindrical source does not hold, as the directivity pattern of the finite source becomes rapidly less directive as  $c_1$  is decreased from  $c_0$  to zero.

Having thus explained in a crude way the principle underlying the end-fire source, a more rigorous analysis of the finite source will be presented in the next chapter.

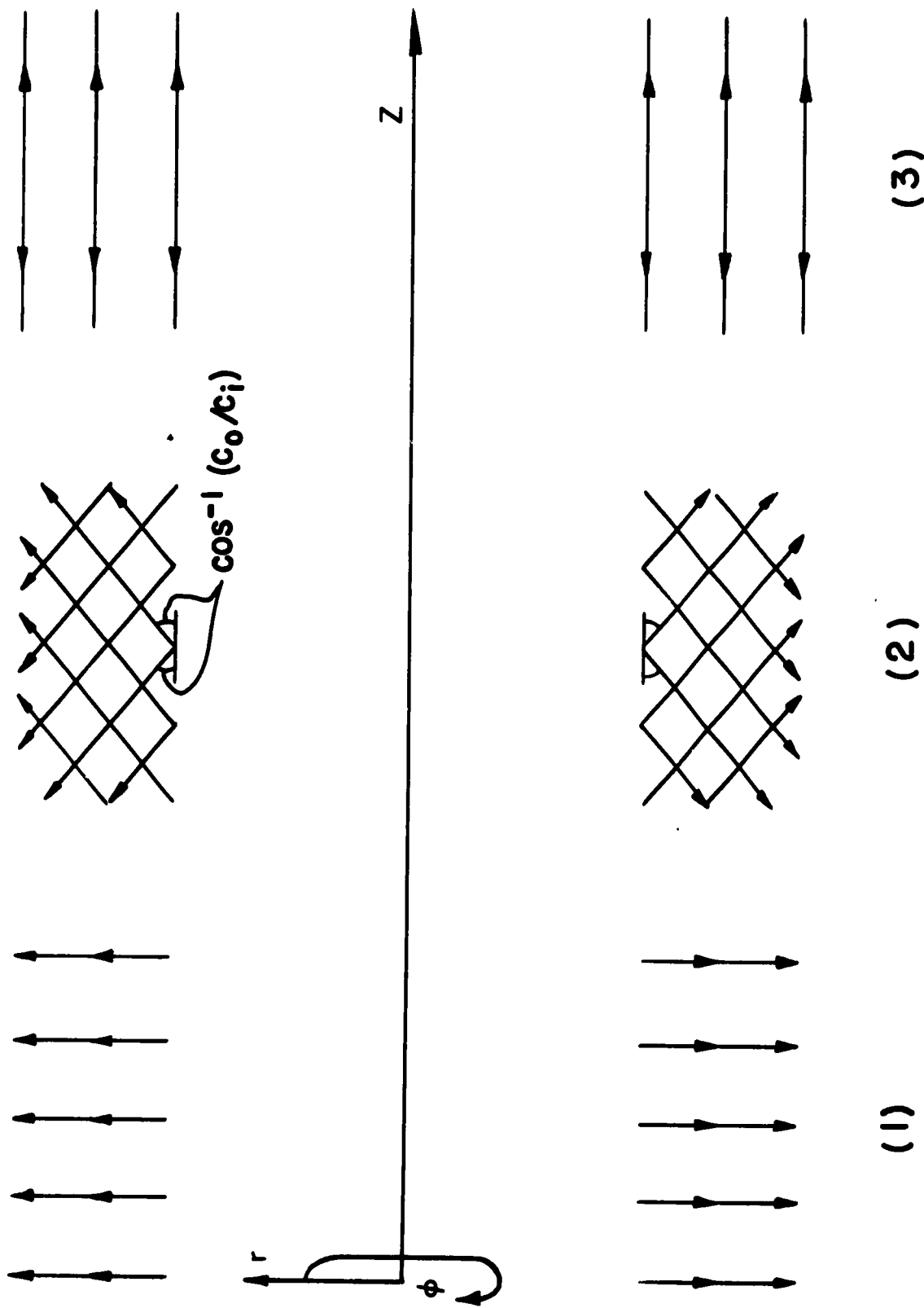


Fig. I.3. Types of waves excited by a vibrating, infinite cylindrical surface.

## Chapter II

Theory of the End-Fire SourceParameters Determining the Directivity PatternAnalysis of the Travelling-Wave Source

A rigorous analysis of the cylindrical source of finite length is not at present available.\* However, an excellent approximation of the far field can be obtained if the finite cylinder is replaced by an infinite one having the same axis and diameter; the surface of the infinite cylinder is rigid except along the segment coinciding with the finite source, where its dynamic configuration is the same as that of the finite source (Fig. II.I). It is to be expected that the distant field produced by this fictional source is very similar to the one generated by the actual finite cylinder. The reason for this similarity is that the distant field is not affected appreciably by the two cylindrical cores prolonging the finite source to infinity; it is therefore immaterial whether these cores consist of the fluid medium (as they actually do) or of a rigid material (as in the case of the fictional, infinite cylinder). Experimental results have shown that this approach yields satisfactory results (cf. Chap. III).

The mathematical model used in this approximate solution is thus an infinite cylinder whose dynamic configuration is described by the following boundary conditions:

$$\dot{u}(z) = 0, \quad \text{for } z < 0 \text{ and } z > L,$$

$$\dot{u}(z) = U \exp\left[-\frac{\mu k_i}{2\pi} z + j(\omega t - k_i z)\right], \quad \text{for } 0 < z < L. \quad (\text{II. 1})$$

The non-homogeneous boundary condition represents attenuated travelling

\*Such an analysis requires the solution of a Fredholm integral equation of the first kind. A variational technique has been applied to this integral equation. At the time of writing, the solution had been completed except for the evaluation of certain contour integrals.

waves, limited to the region  $0 < z < L$ . The formal problem is thus to determine the velocity potential  $\psi(r, \phi, z)$  [or, using the space vector  $\bar{R}$ ,  $\psi(\bar{R})$ ] which satisfies the boundary condition  $\dot{u}(z)$  defined above:

$$\frac{\partial \psi(\bar{R})}{\partial r} \Big|_{r=a} = \dot{u}(z). \quad (\text{II. 2})$$

The problem where Neumann boundary conditions [i.e., conditions of the type in Eq. (II.2)] are prescribed on an infinite cylinder was solved by Laird and Cohen (4) by matching boundary conditions. However, it is felt that the alternative approach to this problem by means of the Green's function method is of sufficient interest to be presented here. The analysis, as given in this section, is greatly condensed; intermediate steps can be found in the Appendix.

The general form of the Green's function for outgoing waves in cylindrical coordinates is given by Levine and Schwinger (5). Since Neumann boundary conditions, Eq. (II.2), are prescribed, the particular form of this Green's function appropriate for the present problem should satisfy the condition (cf. Appendix)

$$\frac{\partial G(\bar{R}, \bar{R}')}{\partial r'} \Big|_{r'=a} = 0. \quad (\text{II. 3})$$

This form is found by a procedure parallel to the one used by Papas (6) in obtaining a Green's function satisfying the condition  $G(\bar{R}, \bar{R}')|_{r'=a} = 0$ , required in problems where Dirichlet boundary conditions are prescribed. For the Neumann problem, the desired form of the Green's function is found to be

$$G(\bar{R}, \bar{R}') = -\frac{j}{8\pi} \sum_{\mu=-\infty}^{\infty} e^{-jm(\phi-p')} \int_{-\infty}^{\infty} \frac{H_m^{(2)}(\sqrt{k_0^2 - \xi^2} r')}{H_m^{(2)*}(\sqrt{k_0^2 - \xi^2} a)} \quad (\text{II. 4})$$

$$[H_m^{(2)}(\sqrt{k_0^2 - \xi^2} a) J_m(\sqrt{k_0^2 - \xi^2} r') - H_m^{(2)*}(\sqrt{k_0^2 - \xi^2} r') J_m(\sqrt{k_0^2 - \xi^2} a)] e^{-j\xi(z-z')} d\xi$$

where  $r'>$ ,  $r'<$  indicate, respectively, the larger and the smaller of the coordinates  $r$ ,  $r'$ , and where the apostrophe denotes differentiation. Setting  $r' = a$ , the Green's function on the boundary surface becomes

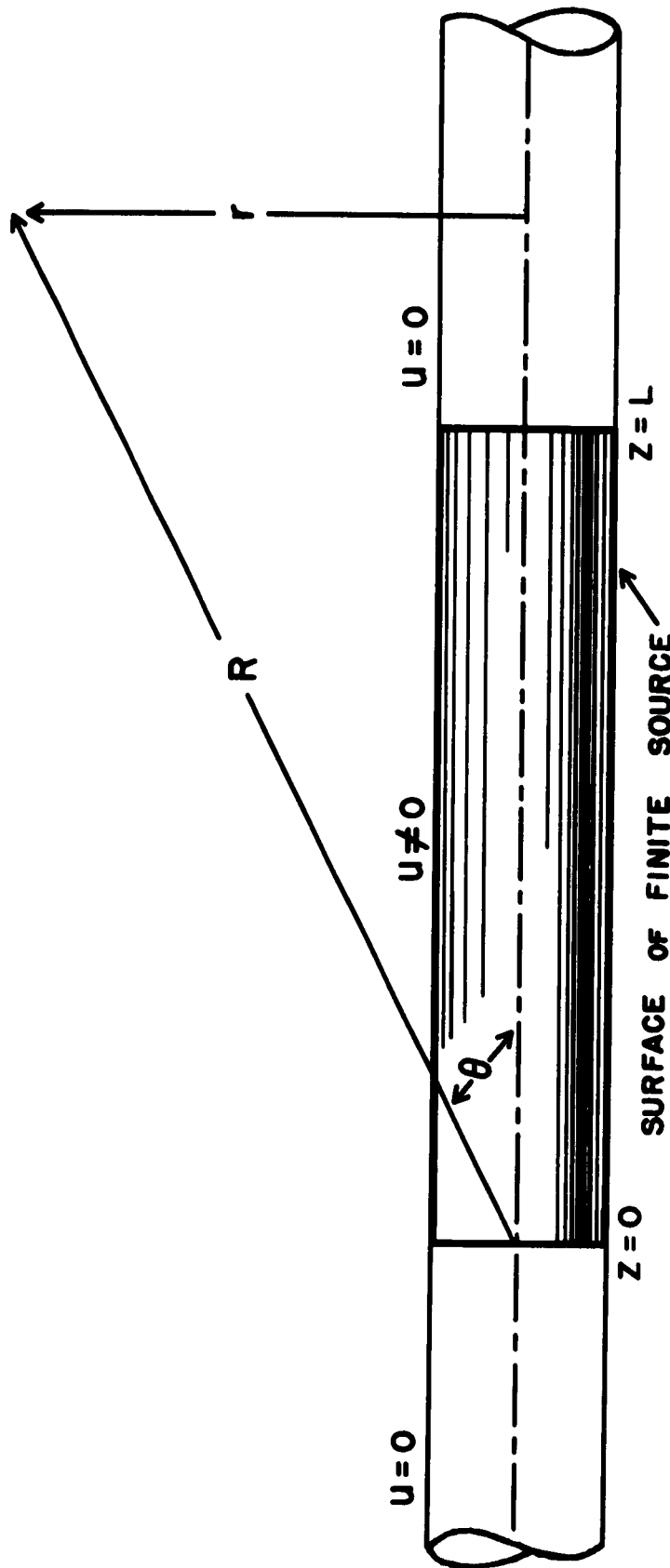


Fig. II.1. Mathematical model used in the analysis of the end-fire source.

$$G(\bar{R}, \bar{R}') = \frac{-1}{4\pi^2 a} \sum_{m=-\infty}^{\infty} \int_{-\infty}^{\infty} \frac{H_m^{(2)}(\sqrt{k_o^2 - \zeta^2} r) e^{-jm(\phi - \phi')} e^{-j\zeta(z - z')}}{\sqrt{k_o^2 - \zeta^2} H_m^{(2)'}(\sqrt{k_o^2 - \zeta^2} a)} d\zeta \quad (\text{II. 5})$$

The solution to the problem is formally given by the integral

$$\Psi(\bar{R}) = a \int_{-\infty}^{\infty} \int_0^{2\pi} G(\bar{R}, \bar{R}') r' = a \int_0^{2\pi} \int_{-\infty}^{\infty} \dot{u}(\phi', z') d\phi' dz' \quad (\text{II. 6})$$

Switching to spherical coordinates, i.e., setting  $r = R \sin \theta$  and  $z = R \cos \theta$ , and using the asymptotic expression for the Hankel function of large argument (i.e., assuming that  $R$  is large), the solution reduces to a form which can be integrated by means of the method of stationary phase (cf. Appendix). Introducing the boundary condition (II. 1) and noting that  $p(\bar{R}) = j\omega \rho \Psi(\bar{R})$ , the following expression for the sound pressure is obtained:

$$p(R, \theta) = \frac{\rho_o c_o e^{-jk_o R}}{\pi R \sin \theta H_o^{(2)'}(k_o a \sin \theta)} \dot{u}(k_o \cos \theta) \quad (\text{II. 7})$$

where  $\dot{u}(k_o \cos \theta)$  is the Fourier transform of the boundary condition

$$\begin{aligned} \dot{u}(\zeta) &= U e^{j\omega t} \int_0^L \exp\left(-\frac{\mu k_i}{2\pi} - jk_i + j\zeta z\right) dz \\ &= \frac{jU e^{j\omega t}}{k_i} \frac{1 - \exp[-n\mu - 2n\pi j(1 - \zeta/k_i)]}{(1 - \zeta/k_i) - j\mu/2\pi} \end{aligned} \quad (\text{II. 8})$$

evaluated at  $\zeta = k_o \cos \theta$ .

Upon substitution of this transform in Eq. (II.7), the final expression for the sound pressure becomes

$$\begin{aligned} p(R, \theta) &= \frac{\rho_o c_o U \exp\left[j(\omega t - k_o R + \beta(\theta) + \delta_1(k_o a \sin \theta) - \gamma(\theta))\right]}{\pi k_i \left[\left(1 - \frac{c_i}{c_o} \cos \theta\right)^2 + \left(\frac{\mu}{2\pi}\right)^2\right]^{1/2} R \sin \theta H_1^{(2)}(k_o a \sin \theta)} \\ &\quad [1 + e^{-2n\mu} - 2e^{-n\mu} \cos 2n\pi \left(1 - \frac{c_i}{c_o} \cos \theta\right)]^{1/2} \end{aligned} \quad (\text{II. 9})$$

where

$$\delta_1(k_o a \sin \theta) = \tan^{-1} [-J_1(k_o a \sin \theta)/N_1(k_o a \sin \theta)]$$

$$\beta(\theta) = \tan^{-1} \frac{\mu}{\frac{c_i}{c_o} \cos \theta}$$

$$\gamma(\theta) = -\tan^{-1} \left\{ \sin 2n\pi \left( 1 - \frac{c_i}{c_o} \cos \theta \right) / [e^{\mu n} - \cos 2n\pi \left( 1 - \frac{c_i}{c_o} \cos \theta \right)] \right\}$$

The angular distribution of sound energy is obtained by normalizing this expression with respect to the on-beam pressure:

$$\left| \frac{p(R, \theta)}{p(R, 0)} \right|^2 = \left[ \frac{2}{\pi k_o a \sin \theta |H_1^{(2)}(k_o a \sin \theta)|} \right]^2 \frac{(1 - \frac{c_i}{c_o})^2 + (\frac{\mu}{2\pi})^2}{(1 - \frac{c_i}{c_o} \cos \theta)^2 + (\frac{\mu}{2\pi})^2} \quad (\text{II.10})$$

The four parameters which determine this ratio are  $k_o a$ ,  $c_i/c_o$ ,  $n$ , and  $\mu$ . The effect of  $k_o a$  is negligible as seen from Figs. II.2 and II.3. Even though these patterns were computed for a semi-infinite source (i.e.,  $n = \infty$ ), this general conclusion will be shown to hold for a finite source. The fundamental feature of the end-fire source, i.e., that its pattern is essentially independent of frequency and source diameter, is thus established.

These two figures also illustrate the other fundamental fact that end-fire directivity is achieved only when  $(c_i/c_o)$  is approximately equal to unity. When  $c_i/c_o$  is as little as 15 per cent off, as for the pattern in Fig. II.3, radiation becomes non-directive. When  $c_i/c_o$  is larger than unity, the pattern has two prongs, as shown in Fig. II.4 (and as discussed in Chap. I). Even in a source only 15 or 20 wavelengths long, the angular separation between the two prongs approaches very closely the value of twice the vertex angle of the conical wave generated by an infinite cylinder (i.e.,  $\cos^{-1} c_o/c_i$ ).

The absolute value of the length of the source is not as significant as the quantity  $n = L/\lambda$ ; i.e., the length of the source measured in wavelengths. If maximum directivity is desired, and assuming that  $c_i/c_o \approx 1$ , there is a certain optimal source length  $n$  which yields essentially as much directivity as a semi-infinite source. It is therefore not economical to use a source which is larger than this optimal length; one might say that any additional

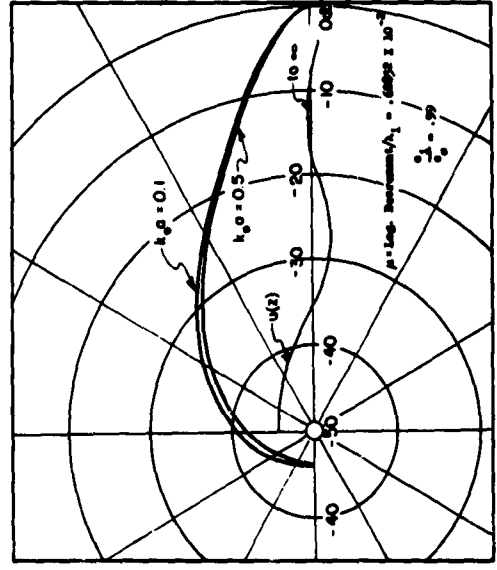


Fig. II.2. Directivity patterns of a semi-infinite, travelling-wave source, for  $c_1/c_0 = 0.99$ ,  $k_0 a = 0.1$  and  $0.5$ , and  $\mu = 0.00628$ . The directivity is seen to be high when  $c_1 \approx c_0$ , in spite of the small values of  $k_0 a$ .

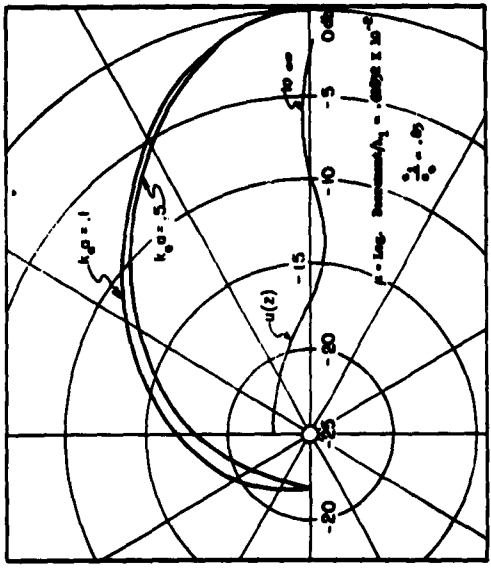


Fig. II.3. Directivity patterns of a semi-infinite, travelling-wave source, for  $c_1/c_0 = 0.85$ ,  $k_0 a = 0.1$  and  $0.5$ , and  $\mu = 0.00628$ . The directivity is seen to be low when  $c_1$  is considerably less than  $c_0$ .

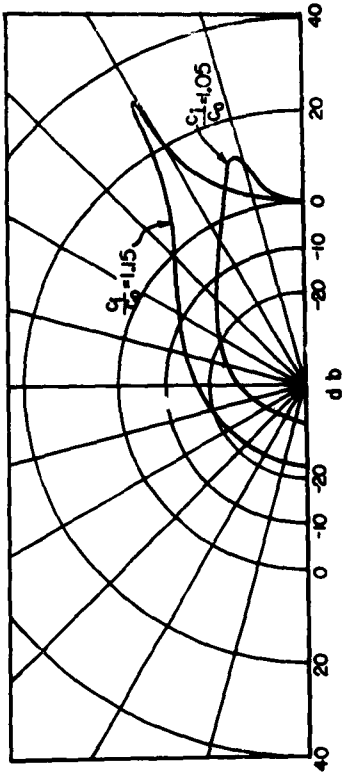


Fig. II.4. Directivity patterns of a semi-infinite, travelling-wave source, for  $c_1/c_0 = 1.05$  and  $1.15$ ,  $k_0 a = 0.1$ ,  $\mu = 0.00628$ . The pattern embodies two prongs whose separation increases as the ratio  $c_1/c_0$  is increased, when  $c_1/c_0 > 1$ .

source length is of sub-marginal utility. If the source is to operate over a certain frequency range, its absolute length  $L$  must be great enough so that  $n$  will not be smaller than this optimal value even for the lowest operating frequency. This is illustrated quantitatively in Fig. II.5 (a) and (b). These graphs also indicate that the optimal source length is greater when  $\mu$  is smaller; consequently, as a crude rule of thumb, the optimal value of the product ( $n\mu$ ) can be taken to be roughly a constant. The effect of source length on the directivity is also illustrated in Fig. II.6, where the value of the marginal length increase is clearly shown.

The effect of the attenuation  $\mu$  is such that a directive source becomes more directive when it is decreased, provided the reduction in  $\mu$  is accompanied by an increase in  $n$ . This effect is illustrated in Fig. II.7. A reduction in  $\mu$  has a slightly unfavorable effect if the source length is not increased correspondingly. In the case of a two-pronged pattern, a reduction in  $\mu$  causes the prongs to become more slender and more pronounced.

#### Analysis of the Standing-Wave Source

Consider now a source in the form of a cylinder terminated by a reflective end (Fig. II.2). The pressure distribution along the cylinder is in the form of attenuated standing waves. Such a source is inherently more efficient than the travelling-wave source since, neglecting frictional losses, all the energy provided by the transducer will eventually be radiated in the form of sound instead of being absorbed in viscous losses. The new difficulty that arises is that of backfiring, which is insignificant in the travelling-wave source, but which may become important in the standing-wave source, for sufficiently small attenuation. However, the nature of the termination has little effect if most of the energy is dissipated before the wave has reached the end of the cylinder, so that no appreciable backfiring occurs when the product ( $n\mu$ ) is sufficiently large.

The standing-wave pressure  $p(z)$  in a "lossy" tube terminated by a perfectly reflective surface is (cf. for example, Section VI.23 of reference (7)),

$$p(z) = 2P_0 e^{j\omega t} \cosh k_i \left( \frac{\mu}{2w} + j \right) z \quad (\text{II.11})$$

where, for convenience, the reflective end of the source has been taken as the origin of  $z$ ; hence the pressure amplitude  $2P_0$  would be measured at the reflective end. Setting  $z = L$  it is found that the pressure amplitude on the surface of the transducer, at the driving end of the cylindrical source, is

$$|p(L)| = 2P_0 (\cosh^2 n\mu \cos^2 2nw + \sinh^2 n\mu \sin^2 2nw)^{\frac{1}{2}} \quad (\text{II.12})$$

The dynamic configuration of the source obeys the same functional relations with the variables  $z$  and  $t$  as the pressure  $p(z)$ . Proceeding as for the travelling-wave source the far field is obtained by considering an infinite cylindrical surface having non-homogeneous boundary conditions in the region  $0 < z < L$ :

$$\begin{aligned} \dot{u}(z) &= 2\dot{U}e^{j\omega t} \cosh k_i \left( \frac{\mu}{2\pi} + j \right) z \text{ for } z < 0, z > L \\ \dot{u}(z) &= 0 \end{aligned} \quad (\text{II.13})$$

The Fourier transform of the boundary condition is obtained by introducing the exponential form of the hyperbolic cosine:

$$\begin{aligned} \dot{u}(\zeta) &= \dot{U} e^{j\omega t} \int_0^L \left\{ \exp[k_i \left( \frac{\mu}{2\pi} + j \right) z] + \exp[-k_i \left( \frac{\mu}{2\pi} + j \right) z] \right\} e^{j\zeta z} dz \\ &= - \frac{j\dot{U}e^{j\omega t}}{k_i} \left\{ \frac{1 - \exp[-n\mu - 2jn\omega(1 - \frac{\zeta}{k_i})]}{-j \frac{\mu}{2\pi} + (1 - \frac{\zeta}{k_i})} - \frac{1 - \exp[n\mu + 2jn\omega(1 + \frac{\zeta}{k_i})]}{-j \frac{\mu}{2\pi} + (1 + \frac{\zeta}{k_i})} \right\} \end{aligned} \quad (\text{II.14})$$

Setting  $\zeta = k_o \cos \theta$  and substituting the corresponding value of the transform in Eq. (II.7), one obtains an expression which, after much manipulation, reduces to

$$p(R, \theta) = p(R, \theta)_+ + p(R, \theta)_- \quad (\text{II.15})$$

In this expression,  $p(R, \theta)_+$  coincides with Eq. (II.9) associated with a wave travelling in the  $+z$ -direction;  $p(R, \theta)_-$ , which corresponds to a wave travelling in the opposite direction, is also derived from Eq. (II.9) by using  $-c_i$ ,  $-k_i$  and  $-n$ . The expression for the pressure can be written in polar form as follows:

$$p(R, \theta) = \left\{ |p(R, \theta)_+|^2 + |p(R, \theta)_-|^2 - 2 |p(R, \theta)_+| \cdot |p(R, \theta)_-| \cos[\gamma(\theta)_+ - \gamma(\theta)_- - \beta(\theta)_+ + \beta(\theta)_-] \right\}^{\frac{1}{2}} \exp[j(\omega t - k_o R + \delta_1(k_o a \sin \theta) - \epsilon(\theta))] \quad (\text{II.16})$$

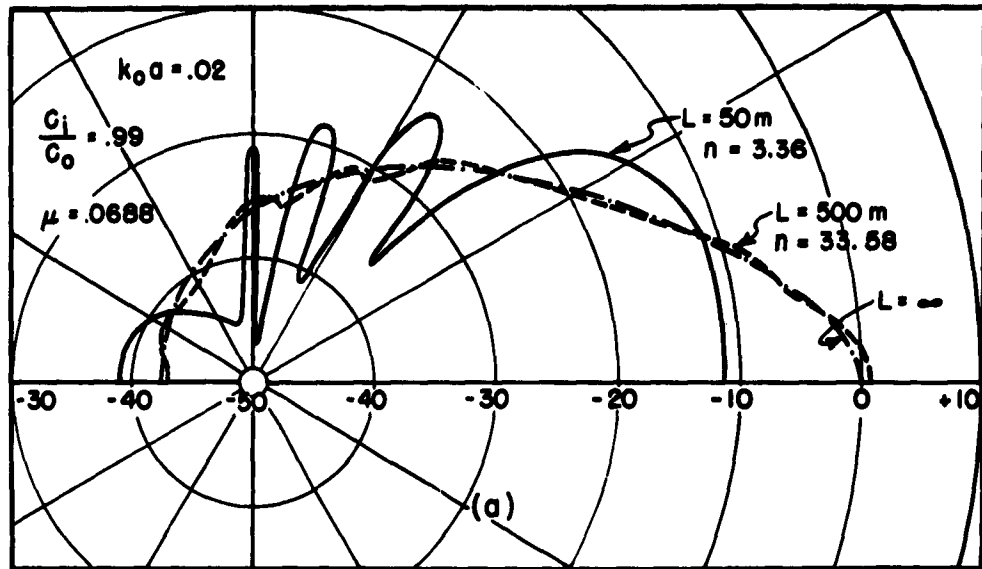


Fig. II.5 (a). Directivity patterns of traveling-wave sources of three different lengths ( $L = 50\text{ m}$ ,  $n = 3.36$ ;  $L = 500\text{ m}$ ,  $n = 33.6$ ; and  $L = \infty$ ), normalized to the on-beam intensity of the semi-infinite source ( $L = \infty$ ), for small attenuation;  $c_1/c_0 = 0.99$ ,  $k_0 a = 0.02$ , and  $\mu = 0.0688$ .

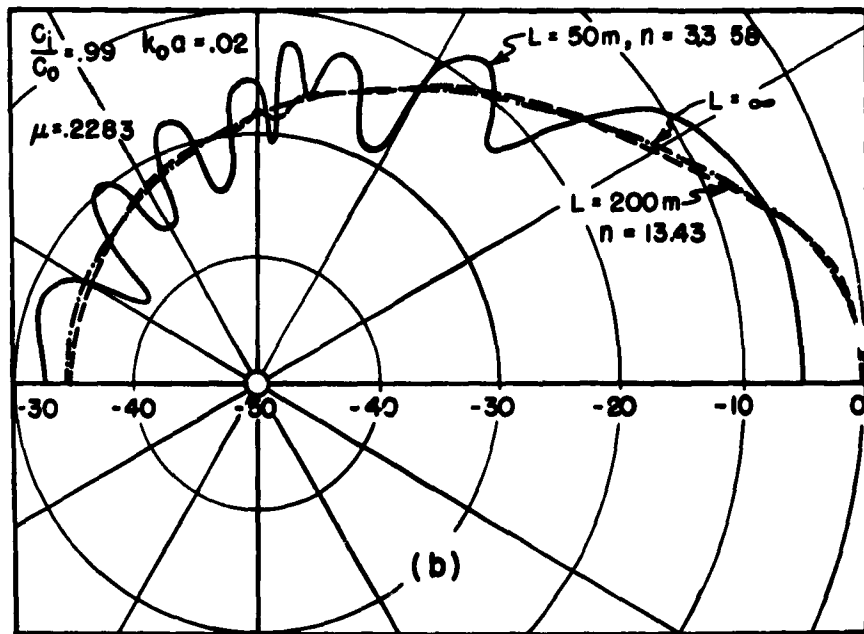


Fig. II.5 (b). Directivity patterns of travelling-wave sources of three different lengths ( $L = 50\text{ m}$ ,  $n = 3.36$ ;  $L = 200\text{ m}$ ,  $n = 13.4$ , and  $L = \infty$ ), normalized to the on-beam intensity of the semi-infinite source ( $L = \infty$ ), for large attenuation;  $c_1/c_0 = 0.99$ ,  $k_0 a = 0.02$ , and  $\mu = 0.2283$ . When this figure is compared with Figure II.5 (a), it is seen that a larger attenuation reduces the optimal source length.

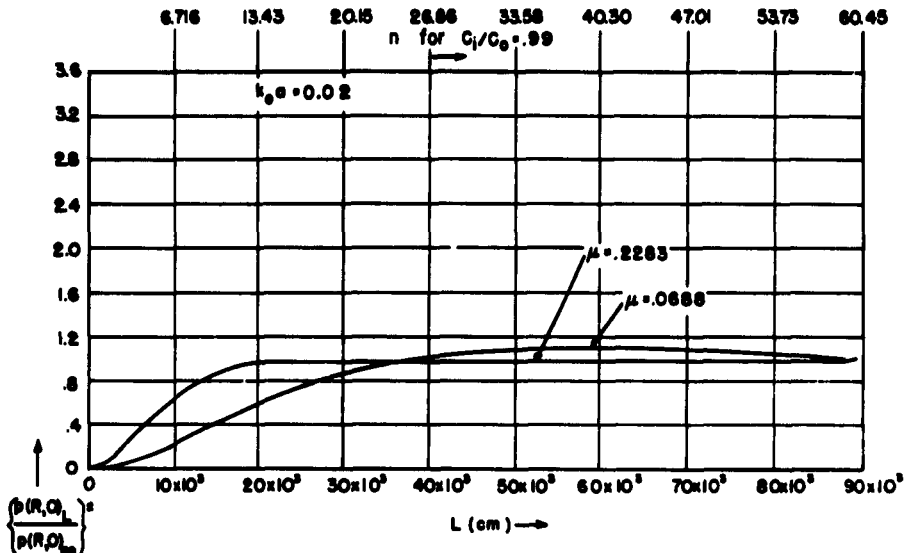


Fig. II.6. On-beam sound intensity of traveling wave sources of finite length  $L$  normalized to the on-beam sound intensity of a semi-infinite source for small and large attenuations;  $c_1/c_0 = 0.99$ ,  $k_o a = 0.02$ ,  $\mu = 0.0688$ , and  $\mu = 0.2283$ . This figure illustrates that, if the attenuation is small, a greater source length is required to take full advantage of the end-fire directive properties of this type of source.

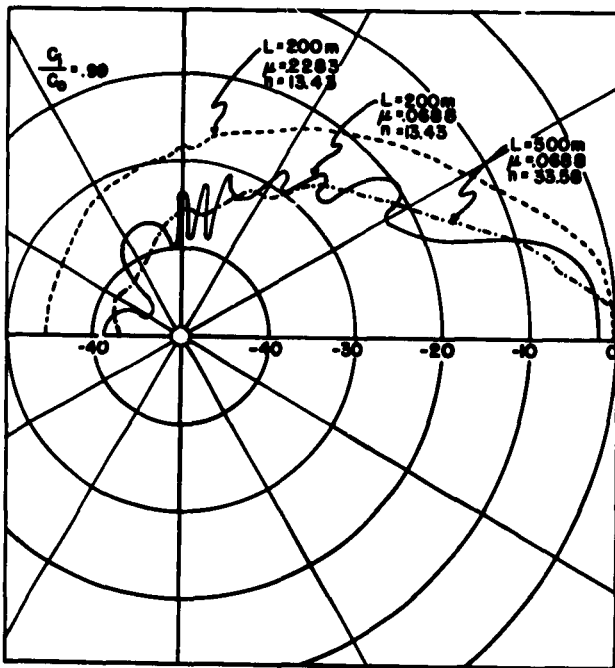


Fig. II.7. Directivity patterns of traveling-wave sources of two different lengths ( $L = 200 \text{ m}$ ,  $n = 13.43$ , and  $L = 500 \text{ m}$ ,  $n = 33.58$ ) and two different attenuations ( $\mu = 0.0688$  and  $0.2283$ );  $c_1/c_0 = 0.99$ ,  $k_o a = 0.02$ . These patterns illustrate that a reduction in  $\mu$  accompanied by an increase in length results in higher end-fire directivity.

where

$$\left| p(R, \theta)_{\pm} \right| = \frac{p_0 c_o U}{\pi k_i R \sin \theta |H_1^{(2)}(k_o a \sin \theta)|} \left[ \frac{1 + e^{\mp 2n\mu} - 2e^{\mp n\mu} \cos 2n\pi(1 \mp \frac{c_i}{c_o} \cos \theta)}{\frac{\mu^2}{4\pi^2} + (1 \mp \frac{c_i}{c_o} \cos \theta)^2} \right]^{\frac{1}{2}}$$

$$\gamma(\theta)_{\pm} = \tan^{-1} \frac{\mp \sin 2n\pi(1 \mp \frac{c_i}{c_o} \cos \theta)}{e^{\pm n\mu} - \cos 2n\pi(1 \mp \frac{c_i}{c_o} \cos \theta)} \quad (\text{II.17})$$

$$\beta(\theta)_{\pm} = \tan^{-1} \frac{\frac{\mu}{2\pi}}{\frac{c_i}{1 \mp \frac{c_i}{c_o} \cos \theta}}, \epsilon(\theta) = \tan^{-1} \left\{ -\cot \left[ \frac{\gamma(\theta)_+ - \beta(\theta)_+ + \gamma(\theta)_- - \beta(\theta)_-}{2} \right] \right\}$$

and where the angle  $\delta$  is defined following Eq. (II. 9). The angular distribution can now be computed from the following ratio:

$$\left| \frac{p(R, \theta)}{p(R, 0)} \right|^2 = \frac{\left| p(R, \theta)_+ \right|^2 + \left| p(R, \theta)_- \right|^2 - 2 \left| p(R, \theta)_+ \right| \cdot \left| p(R, \theta)_- \right| \cos[\gamma(\theta)_+ - \gamma(\theta)_- - \beta(\theta)_+ + \beta(\theta)_-]}{\left| p(R, \theta)_+ \right|^2 + \left| p(R, \theta)_- \right|^2 - 2 \left| p(R, \theta)_+ \right| \cdot \left| p(R, \theta)_- \right| \cos[\gamma(\theta)_+ - \gamma(\theta)_- - \beta(\theta)_+ + \beta(\theta)_-]} \quad (\text{II.18})$$

The angles  $\gamma(\theta)_+$  and  $\beta(\theta)_+$  are obtained directly from Eqs. (II. 17) by setting  $\cos \theta$  equal to unity. The expression for  $|p(R, \theta)_+|$ , however, must be derived in a somewhat more complicated fashion by studying the limit of  $|p(R, \theta)_+|$  as  $\theta$  tends to zero:

$$\left| p(R, \theta)_+ \right| = \frac{p_0 c_o U}{2R} \frac{1 + e^{\mp 2n\mu} - 2e^{\mp n\mu} \cos 2n\pi(1 \mp \frac{c_i}{c_o})^{\frac{1}{2}}}{[(\frac{\mu}{2\pi})^2 + (1 \mp \frac{c_i}{c_o})^2]^{\frac{1}{2}}} \quad (\text{II.19})$$

The directivity pattern produced by the standing-wave source shows that this source is equivalent to two superimposed travelling-wave sources pointed in opposite directions and whose excitations differ in phase and magnitude. The effects of the parameters  $k_o a$ ,  $c_i/c_o$ ,  $n$ , and  $\mu$  on the directivity pattern are therefore of the same nature as in the case of the travelling-wave source. The only new effect is the backfiring produced

by the  $p_+$  (i.e., reflected) radiation. Equation (II.16) indicates that, for large values of  $(n\mu)$ ,  $p_-$  is much larger than  $p_+$ . Hence, for a source with much attenuation or of great length, the nature of the terminating surface has little effect on the radiation pattern. This is illustrated in Figs. II.8 and II.9. The frame of reference and the coordinates are the same in the two figures; i.e., the patterns obtained from the analysis were rotated  $180^\circ$  and normalized with respect to the end-fire sound pressure so as to conform to the conventions used in dealing with the travelling-wave source. The directivity is seen to be fairly high, but could be improved considerably in the case of the source with small attenuation (Fig. II.9) by using a greater source length.

Various kinds of devices can be used to reflect the back-fired energy forward. In general, however, this should not be necessary, as a source which is long enough to give good end-fire directivity will have little back-firing. In other words, in a well-designed source, with an adequately large value of  $(n\mu)$ , it is immaterial whether the termination is reflective or absorptive.

#### An End-Fire Source in the Form of a Battery of Partly Occluded Cylinders

It will be seen in (Chap. IV) that the major difficulty encountered in designing the two types of sources analyzed above is to achieve the condition  $c_i \approx c_o$ , required for good directivity. In the case of a source in the form of a fluid-filled hose, the difficulty derives from the fact that no liquid suitable for usage in the fluid column has a sound velocity considerably in excess of that of water (i.e., of  $c_o$ ); hence, the equality  $c_i \approx c_o$  requires a tube with stiff walls, i.e., a condition which severely limits the rates of sound radiation which can be achieved. This difficulty can be circumvented by a stratagem to be discussed in (Chap. IV), which is to operate the hose above resonance, i.e., to use a mass-controlled hose wall. The device here described avoids this difficulty, as it calls for a value of  $c_i/c_o = 1/2$ . This condition can easily be achieved by using the same fluid in the hose as in the surrounding medium, operating the hose below resonance, and using a fairly flexible hose wall (cf. Chap. IV). The drawback of this type of source is that at least four, preferably eight, hoses are required. This source can, of course, also be in the form of a solid rod as of an elastic shell.

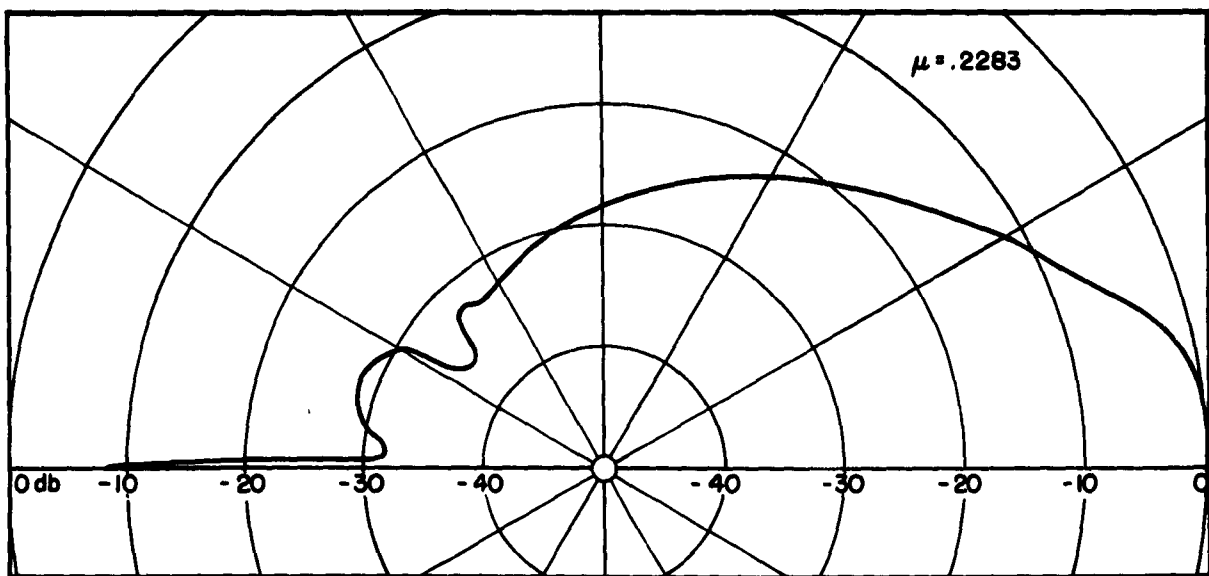


Fig. II.8. Directivity pattern of the standing-wave source for large attenuation;  $c_1/c_0 = 0.99$ ,  $k_0 a = 0.02$ ,  $n = 14.1$ ,  $\mu = 0.2283$ . Backfiring is unimportant because most of the energy is dissipated before the waves reach the reflective termination.

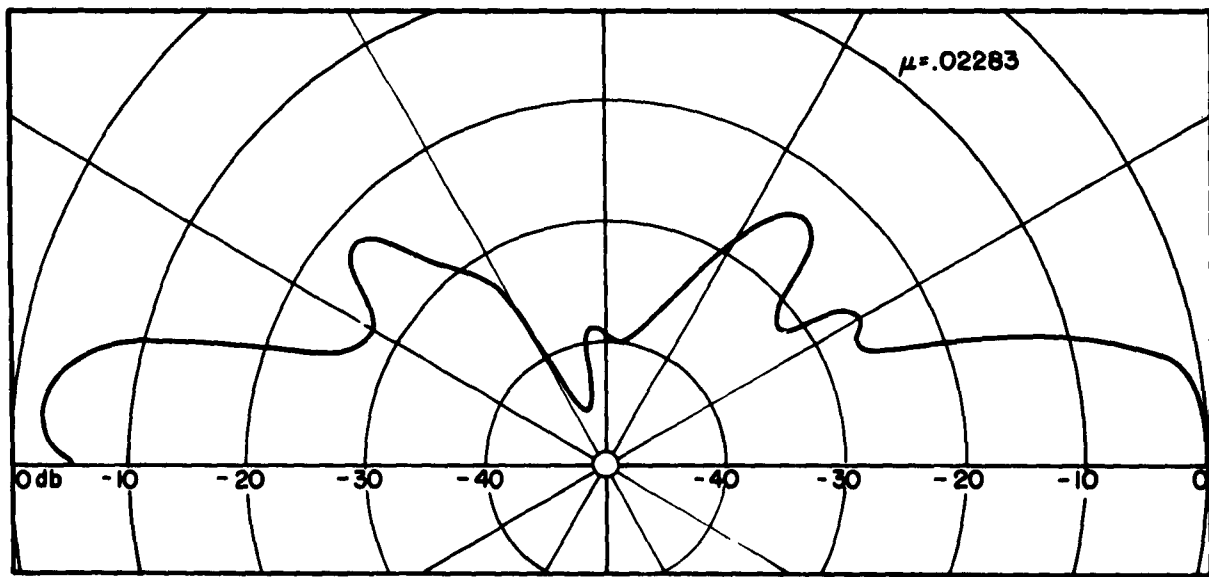


Fig. II.9. Directivity patterns of the standing-wave source for small attenuation;  $c_1/c_0 = 0.99$ ,  $k_0 a = 0.02$ ,  $n = 14.1$ ,  $\mu = 0.02283$ . Backfiring is considerable. Termination of the cylinder is of importance when, as in the present case,  $(n\mu)$  is relatively small.

The source consists of a battery of four partly occluded, staggered tubes. The radiating windows are located at intervals of two wavelengths  $\lambda_i$  and measure one half-wavelength. They play the role of the point sources in an end-fire array. By properly staggering the tubes, and by using appropriate phase angles between the pressure waves injected into each tube, high end-fire directivity can be achieved. There are several combinations which yield satisfactory results. It is possible to improve the directivity pattern of any such combination still further by using two batteries of four tubes. By properly adjusting their phase relationship in space and time one can completely eliminate either backfiring or broadside radiation. A source which combines end-fire directivity at small  $k_o$  with large rates of sound energy radiation, thus appears to be practicable. The mathematical theory required to calculate the directivity pattern of this type of source will now be developed.

Consider a fluid column conducting travelling waves; the column is bounded by a cylindrical surface which is flexible (i.e., radiating) over intervals of  $1/2\lambda_i$ , separated by intervals having a length of  $3/2\lambda_i$ , where the cylindrical surface is rigid, and therefore non-radiating. (cf. Fig. II.10). Using the customary notation, the radial velocity of the tube surface is

$$\dot{u}_o(z) = \dot{U} e^{\frac{\mu}{2\pi} k_i z} e^{j(\omega t - k_i z)} \quad \text{when } 2m\lambda_i < z < 2m\lambda_i + \lambda_i/2$$

$$\dot{u}_o(z) = 0 \text{ elsewhere} \quad \text{with } 0 \leq m \leq \frac{n}{2} - 1 \quad (\text{II.20})$$

The integer  $m$  indicates the location of the radiating window relative to other windows. The subscript 0 indicates that the origin of coordinates coincides with the driving end of this source, i.e. that the stagger of the other sources of the battery is measured from this reference source. The phase velocity  $c_i$  is larger in a tube interval bounded by rigid walls than in an interval corresponding to a radiating window, and the attenuation  $\mu$  is smaller. These local variations are ignored here, and average values of  $k_i$  and  $\mu$  are used.

The Fourier transform of this boundary condition is

$$\dot{u}_o(\zeta) = \dot{U} e^{j\omega t} \sum_{m=0}^{\frac{n}{2}-1} J_o^{(m)}(\zeta) \quad (\text{II. 21})$$

where  $J_o^{(m)}(\zeta)$  is the integral

$$\begin{aligned} J_o^{(m)}(\zeta) &= \int_{2m\lambda_i}^{2m\lambda_i + \frac{\lambda_i}{2}} e^{-\frac{\mu k_i z}{2\pi}} e^{-j(k_i - \zeta)z} dz \\ &= \frac{e^{-2m\mu} e^{2m j(\lambda_i \zeta - 2\pi)}}{\frac{\mu}{2\pi} k_i + j(k_i - \zeta)} \left[ 1 - e^{-\frac{\mu}{2} j(\frac{\lambda_i \zeta}{2} - \pi)} \right] \end{aligned} \quad (\text{II. 22})$$

Setting  $\zeta = k_o \cos \theta$ , this integral becomes

$$J_o^{(m)}(k_o \cos \theta) = \frac{-j e^{-2m\mu} e^{-4m j\phi(\theta)} e^{j[\beta(\theta) - \gamma(\theta)]}}{k_i [\frac{\mu}{4} + \phi(\theta)^2]^{\frac{1}{2}}} \pi [1 + e^{-\mu - \frac{\mu}{2} \cos \phi(\theta)}]^{\frac{1}{2}},$$

where

$$\phi(\theta) \propto \pi \left( 1 - \frac{c_i}{c_o} \cos \theta \right)$$

$$\gamma(\theta) = \tan^{-1} \frac{\sin \phi(\theta)}{e^{\mu/2} - \cos \phi(\theta)} \quad (\text{II. 22a})$$

and

$$\beta(\theta) = \tan^{-1} \frac{\mu}{2\phi(\theta)}$$

The pressure field generated by this source is given by Eq. (II.7) after substitution of the value of  $\dot{u}(k_o \cos \theta)$  obtained by combining Eqs. (II.21) and (II.22a):

$$p_o(R, \theta) = \frac{j \rho_o c_o \dot{U} \exp \left\{ j[\omega t - k_o R + \delta_1(k_o a \sin \theta)] \right\}}{\pi R \sin \theta |H_1^{(2)}(k_o a \sin \theta)|} \sum_{m=0}^{\frac{n}{2}-1} J_o^{(m)}(k_o \cos \theta) \quad (\text{II. 23})$$

At  $\theta = 0$ , the pressure is

$$p_0(R,0) = \frac{\dot{U} p_0 c_i a \exp\{j[\omega t - k_o R + \beta(0) + \zeta(0)]\}}{R [\mu^2 + 4\phi^2(0)]^{1/2}} \pi [1 + e^{-\mu} - 2e^{-\frac{\mu}{2}} \cos \phi(0)]^{1/2} \sum_{m=0}^{\frac{n}{2}-1} e^{-2m\mu} e^{-j4m\phi(0)} \quad (\text{II.24})$$

Normalizing the pressure  $p(0)$  with respect to the pressure at  $\theta=0$ , one obtains the angular distribution of sound intensity:

$$\left| \frac{p_0(R,0)}{p_0(0,0)} \right|^2 = \left[ \frac{2}{k_o a \sin \theta |H_1^{(2)}(k_a a \sin \theta)|} \right]^2 \cdot \frac{\mu^2 + 4\phi^2(0)}{\mu^2 + 4\phi^2(0)} \cdot \frac{1 + e^{-\mu} - 2e^{-\frac{\mu}{2}} \cos \phi(0)}{1 + e^{-\mu} - 2e^{-\frac{\mu}{2}} \cos \phi(0)} \cdot \frac{\left| \sum_{m=0}^{\frac{n}{2}-1} e^{-2m\mu} e^{-4m\phi(0)} \right|^2}{\left| \sum_{m=0}^{\frac{n}{2}-1} e^{-2m\mu} e^{-4m\phi(0)} \right|^2} \quad (\text{II.25})$$

Consider now the field generated by another source which differs from the preceding one only in that the radiating windows are all displaced by a certain fraction  $\psi$  of a wavelength. The boundary condition is now

$$\begin{aligned} \dot{u}_\psi(z) &= U e^{-\frac{\mu}{2\pi} k_i z} e^{j(\omega t - k_i z)} && \text{when } (2m + \psi)\lambda_i < z < (2m + \frac{1}{2} + \psi)\lambda_i \\ \dot{u}_\psi &= 0 \text{ elsewhere} && \text{with } 0 \leq m \leq \frac{n}{2} - 1 \end{aligned} \quad (\text{II.26})$$

It is easily verified that

$$\mathcal{J}_\psi^{(m)} = \mathcal{J}_0^{(m)} e^{-\mu\psi} e^{-j2\psi\phi(0)} \quad (\text{II.27})$$

Hence

$$p_\psi(R,0) = p_0(R,0) e^{-\mu\psi} e^{-j2\psi\phi(0)} \quad (\text{II.28})$$

These expressions will now be used to calculate the patterns produced by the combination of several sources of this type. Since  $c_i/c_0 = 1/2$ ,

each source taken individually is non-directive. End-fire directivity is obtained by staggering the sources in space and in time in such a way as to generate favorable interference effects which tend to cancel out energy radiated in the off-beam direction and to reinforce end-fire radiation. First, two combinations (A and B) of four sources each will be studied. Their spatial distribution is the same, but the phase angles between the sources are different for the two combinations (Fig. II.10). The first combination is defined as follows:

(1) Combination A

The radiating windows are staggered as follows:

Hose I:	$\dot{u}(z) \neq 0$	when	$2m\lambda_i < z < 2m\lambda_i + \lambda_i/2$	$\therefore \psi = 0$
II:	$\dot{u}(z)$	"	$2m\lambda_i - \lambda_i/4 < z < 2m\lambda_i + \lambda_i/4$	$\therefore \psi = -1/4$
III:	$\dot{u}(z)$	"	$2m\lambda_i + \lambda_i/2 < z < 2m\lambda_i + \lambda_i$	$\therefore \psi = 1/2$
IV:	$\dot{u}(z)$	"	$2m\lambda_i + \lambda_i/4 < z < 2m\lambda_i + 3\lambda_i/4$	$\therefore \psi = 1/4$

The phase angles are adjusted so that the waves in hoses II and IV lag  $90^\circ$  behind the waves in hoses I and III.

From Eq. (II.28) it is found that the pressures generated by the individual hoses are related to the reference pressure  $p_o$ , given in Eq. (II.23), as follows:

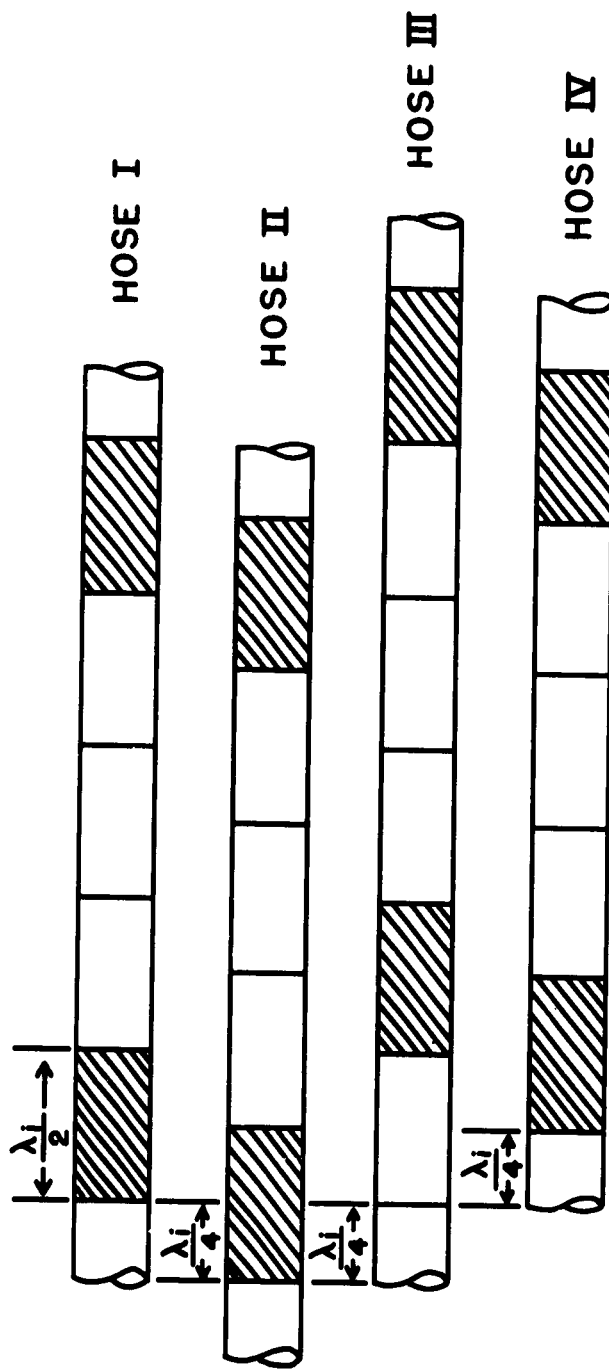
$$\begin{aligned} p_I &= p_o, \\ p_{II} &= -j p_o e^{\frac{+\mu}{4} j \phi(0)} e^{\frac{-\mu}{2}}, \\ p_{III} &= p_o e^{\frac{-\mu}{2}} e^{-j \phi(0)} \end{aligned} \tag{II.29}$$

and

$$p_{IV} = -j p_o e^{\frac{-\mu}{4}} e^{-j \phi(0)/2}$$

Combining these four quantities, one obtains the following expression for the sound field generated by the battery:

$$\begin{aligned} p_A(R, \theta) &= p_o(R, \theta) [2 + 2 \cos \phi(0) + 4 \cos^2 \frac{p(0)}{2} + \\ &+ 4 \sin \phi(0) \cos \frac{\phi(0)}{2}]^{\frac{1}{2}} e^{j \nu A(\theta)} \end{aligned}$$



**Combination A:** Hoses II and IV lag  $90^\circ$  behind hoses I and III.

**Combination B:** Hose II lags  $90^\circ$ .  
Hose IV leads  $90^\circ$ .

Shading indicates radiating windows.

**Fig. II.10.** End-fire directive source in the form of four partly occluded, staggered radiating cylinders ( $c_j/c_0 = 1/2$ ).

where

$$\nu_A(\theta) = \tan^{-1} \frac{-\sin \phi(\theta) - 2 \cos \phi(\theta)/2}{1 + \cos \phi(\theta)} \quad (\text{II.30})$$

In performing this addition, the factors  $e^{-\mu/2}$  and  $e^{\pm\mu/4}$  are assumed to be unity, i.e., it is assumed that no attenuation occurs over a length of hose corresponding to the stagger between radiating windows. This approximation is justified in practice, because this stagger corresponds to a small length of non-radiating hose, over which the attenuation is much less than the average value of  $\mu$ . Expression (II.30) can be normalized with respect to the pressure at  $\theta = 0$  to obtain the angular sound intensity distribution. For  $c_i/c_o = 1/2$ , this distribution becomes

$$\left| \frac{p_A(R,\theta)}{p_A(0)} \right|^2 = \left| \frac{p_o(R,\theta)}{p_o(0)} \right|^2 \frac{1 + \cos \phi(\theta) + 2 \cos^2 \phi(\theta)/2 + 2 \sin \phi(\theta) \cos \phi}{3.414} \quad (\text{II.31})$$

The directivity pattern is plotted in Fig. II.11. This source is seen to be fairly end-fire-directive, except for the tendency to backfiring. This condition can be remedied by combining two four-hose sources, as described below.

## (2) Combination B

The radiating windows are staggered as in combination A. The phase angles between the waves in the individual cylinders are as follows: Hoses I and III are in phase, hose II lags  $90^\circ$ , and hose IV leads  $90^\circ$ . The pressures generated are:

$$\begin{aligned} p_I &= p_o \\ p_{II} &= j p_o e^{-\frac{\mu}{4}} e^{-j\phi(\theta)} \\ p_{III} &= p_o e^{-\frac{\mu}{2}} e^{-j\phi(\theta)} \end{aligned} \quad (\text{II.32})$$

and

$$p_{IV} = j p_o e^{-\frac{\mu}{4}} e^{-j\phi(\theta)/2}$$

Combining these quantities, the resultant sound field pressure is found:

$$p_B(R,\theta) = p_o(R,\theta) [ 2 + 4 \sin^2 \frac{\phi(\theta)}{2} + 2 \cos \phi(\theta) + 4 \sin \phi(\theta) ] + \quad (\text{II.33})$$

$$+ 4 \cos \phi(0) \sin \frac{\phi(0)}{2} \left[ e^{j\phi(0)} \right]$$

where

$$\nu_B(0) = \tan^{-1} \frac{-\sin \phi(0)}{1 + \cos \phi(0) + 2 \sin \frac{\phi(0)}{2}}$$

Normalizing this expression, with respect to the value at  $\theta = 0$ , and setting  $c_i/c_0 = 1/2$ , one obtains:

$$\left| \frac{p_B(R, \theta)}{p_B(R, 0)} \right|^2 = \left| \frac{p_O(R, \theta)}{p_O(R, 0)} \right|^2 \frac{[1 + 2 \sin^2 \frac{\phi(0)}{2} + \cos \phi(0) + 2 \sin \frac{\phi(0)}{2} + 2 \cos \phi(0) \sin \frac{\phi(0)}{2}]}{3.414} \quad (\text{II.34})$$

The corresponding directivity pattern is plotted in Fig. II.12. The pattern is less desirable than that produced by combination A, but two four-hose sources of this type may be combined to produce satisfactory patterns, as shown below.

It is possible to improve these directivity patterns by combining two four-hose batteries in such a way as to eliminate either off-beam or backfire radiation. In the following the pressure of the sound field generated by one battery of four hoses is designated by the symbol  $p_4$  (which may be equal to  $p_A$  or  $p_B$ , according to whether combination A or B is used).

### (1) Combination a

Combination a consists of two batteries, of four hoses each, which are  $180^\circ$  out of phase (cf. Fig. II.13). In space, the two batteries are displaced one wavelength with respect to each other (i.e.,  $\psi = 1$ ). The sound field is given by the equation

$$p_a = p_4 - p_4 e^{-2j\phi(0)} \\ = p_4 [2 - 2 \cos 2\phi(0)]^{\frac{1}{2}} e^{j\sigma_a(0)} \quad (\text{II. 35})$$

where

$$\sigma_a(0) = \tan^{-1} \frac{\sin 2\phi(0)}{1 - \cos 2\phi(0)}$$

Normalizing the sound pressure becomes, for  $c_i/c_0 = 1/2$ ,

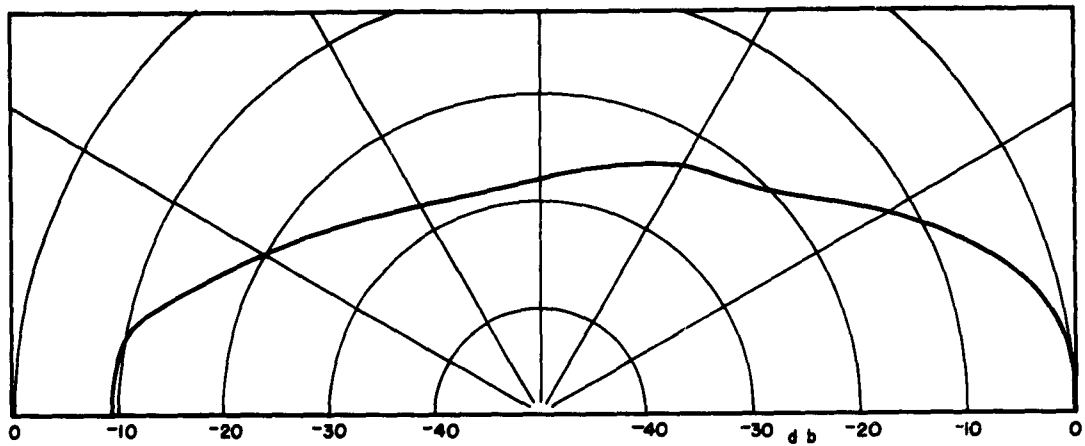


Fig. II.11. Directivity pattern for a battery of four cylinders, combination A,  $k_0 a = 0.1$ ,  $n = 34$ ,  $c_1/c_0 = 0.5$ ,  $\mu = 0.10$ .

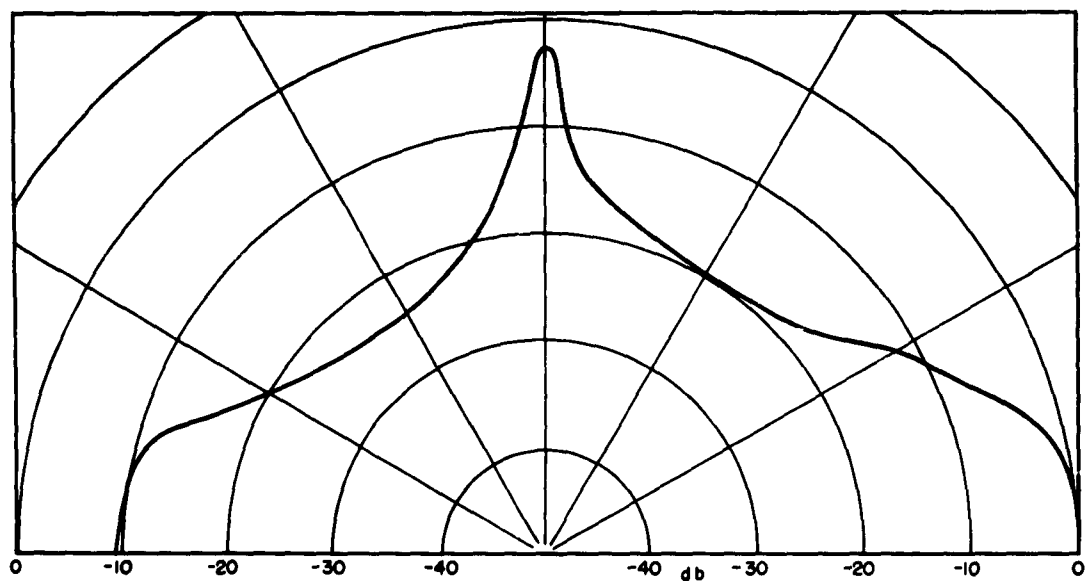
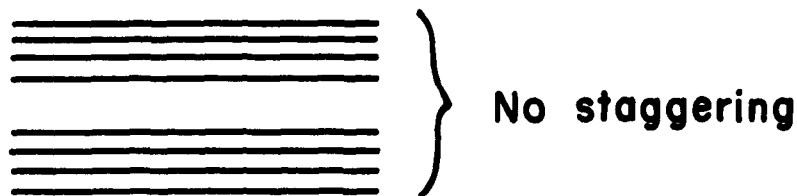
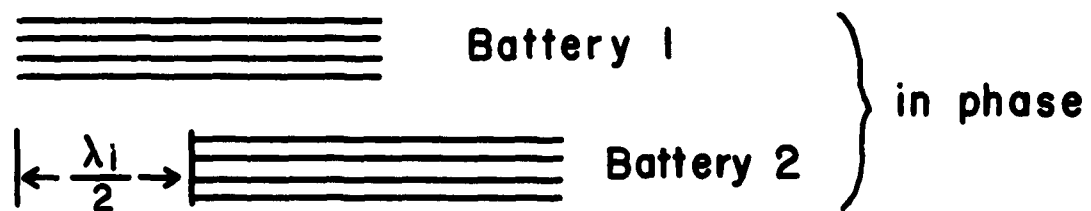


Fig. II.12. Directivity pattern for a battery of four cylinders, combination B,  $k_0 a = 0.1$ ,  $n = 34$ ,  $c_1/c_0 = 0.5$ ,  $\mu = 0.10$ .

**COMBINATION  $\alpha$**   
Two batteries  
 $180^\circ$  out of phase



**COMBINATION  $\beta$**



**COMBINATION  $\gamma$**

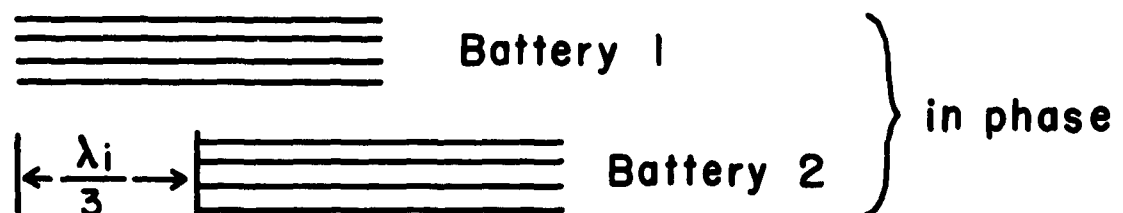


Fig. II.13. Three possible combinations of two four-hose batteries.

$$\left| \frac{p_a(R,\theta)}{p_a(R,0)} \right|^2 = \left| \frac{p_4(R,\theta)}{p_4(R,0)} \right|^2 \frac{1 - \cos 2\phi(\theta)}{2} \quad (\text{II.36})$$

The corresponding directivity patterns are plotted in Figs. II. 14 and II. 15, for  $p_4 = p_A$  and  $p_4 = p_B$ , respectively. It is seen that broadside radiation is eliminated.

### (2) Combination β

The two batteries are in phase and displaced one half-wavelength (i.e.,  $\psi = 1/2$ ). Hence,

$$\begin{aligned} p_\beta &= p_4 + p_4 e^{-j\phi(\theta)} \\ &= p_4 [2 + 2 \cos \phi(\theta)]^{\frac{1}{2}} e^{j\sigma_\beta(\theta)} \end{aligned} \quad (\text{II.37})$$

where

$$\sigma_\beta(\theta) = \tan^{-1} \frac{-\sin \phi(\theta)}{1 + \cos \phi(\theta)}$$

Normalizing, this becomes

$$\left| \frac{p_\beta(R,\theta)}{p_\beta(R,0)} \right|^2 = \left| \frac{p_4(R,\theta)}{p_4(R,0)} \right|^2 [1 + \cos \phi(\theta)] \quad (\text{II.38})$$

This is plotted in Figs. II.16 and II.17 for  $p_4 = p_A$  and  $p_4 = p_B$ , respectively. It is seen that this combination has the same effect as combination α in eliminating broadside radiation, but is more directive.

### (3) Combination γ

The two batteries are in phase, and displaced one third of a wavelength ( $\psi = 1/3$ ). Hence:

$$\begin{aligned} p_\gamma &= p_4 e^{-j\frac{2}{3}\phi(\theta)} + p_4 \\ &= p_4 [2 + 2 \cos \frac{2}{3}\phi(\theta)]^{\frac{1}{2}} e^{j\sigma_\gamma(\theta)} \end{aligned} \quad (\text{II.39})$$

where

$$\sigma_\gamma(\theta) = \tan^{-1} \frac{-2 \sin \frac{2}{3}\phi(\theta)}{1 + \cos \frac{2}{3}\phi(\theta)}$$

Normalizing, this becomes

$$\left| \frac{p_y(R, \theta)}{p_y(R, 0)} \right|^2 = \left| \frac{p_4(R, \theta)}{p_4(R, 0)} \right|^2 \cdot \frac{2 + 2 \cos \frac{2}{3} \phi(\theta)}{3} \quad (\text{II.40})$$

This is plotted in Figs. II.18 and II.19 for  $p_4 = p_A$  and  $p_B$  respectively. It is seen that this combination yields a very favorable pattern: Broadside radiation is reduced, and backfiring is eliminated.

A factor which has been considered is the effect of source length on the directivity pattern. Approximately halving the source length, while keeping  $(n\mu)$  constant, causes only a moderate loss in directivity. This is illustrated in Fig. II.20 for combination A.

There are, no doubt, many other combinations which will produce other and probably more desirable directivity patterns. Among those investigated, the four hose combinations generate patterns which are definitely inferior to those produced by the single sources studied earlier in this chapter. However, two of the eight hose combinations are of interest: combination A-β, which eliminates broadside radiation, (Fig. II.16) and combination A-ε which eliminates backfiring (Fig. II.18). Unfortunately, these advantages are largely neutralized by the inconvenience of the cumbersome system of sources required. Until the designs in Chap. IV, which are based on the requirement  $c_i = c_o$ , are proven to be impractical, this type of source will not be considered.

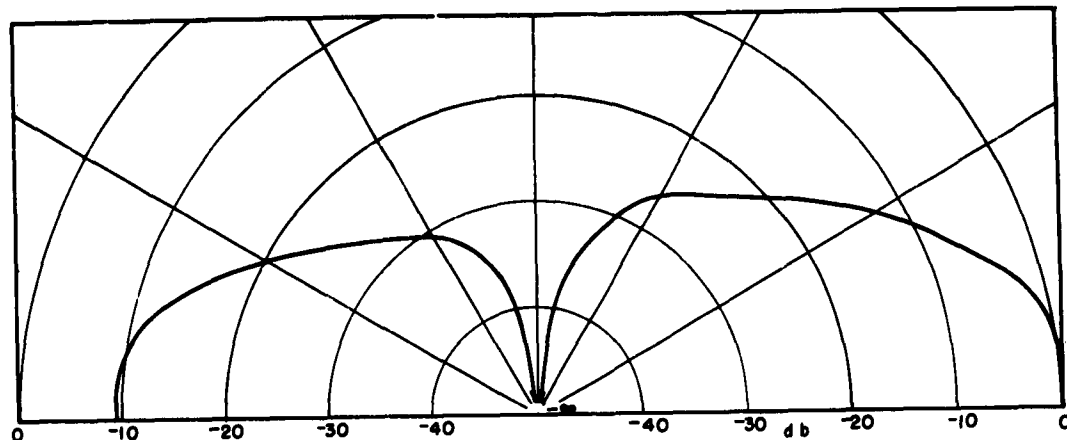


Fig. II.14. Directivity pattern for two four-hose batteries, combination A -  $\alpha$ ,  $k_0 a = 0.1$ ,  $n = 34$ ,  $c_1/c_0 = 0.5$ ,  $\mu = 0.10$ .

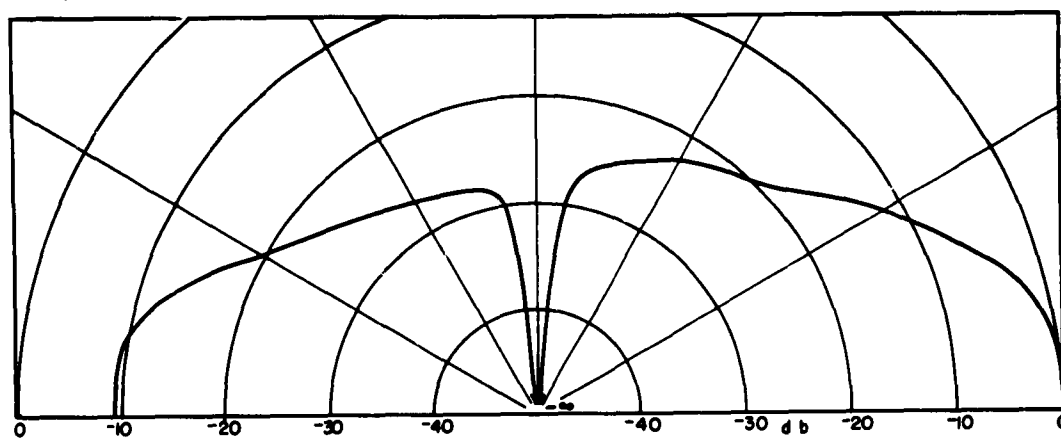


Fig. II.15. Directivity pattern for two four-hose batteries, combination B -  $\alpha$ ,  $k_0 a = 0.1$ ,  $n = 34$ ,  $c_1/c_0 = 0.5$ ,  $\mu = 0.10$ .

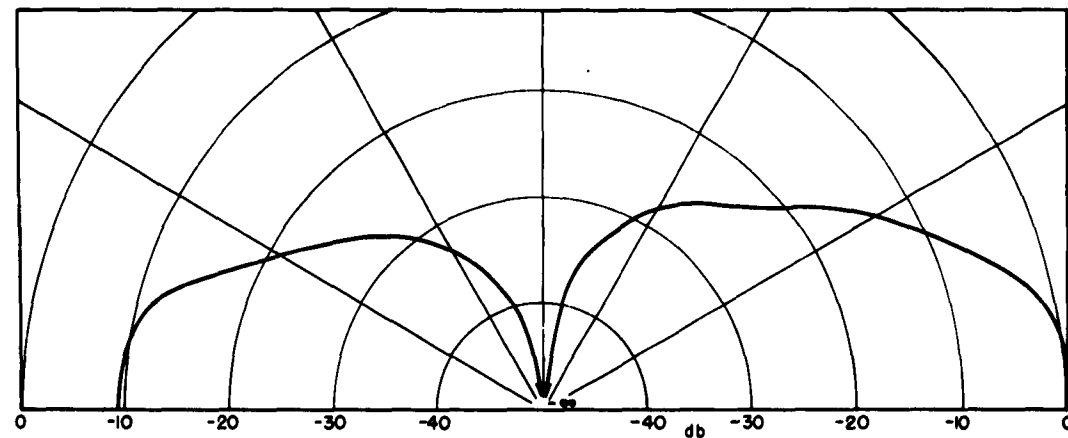
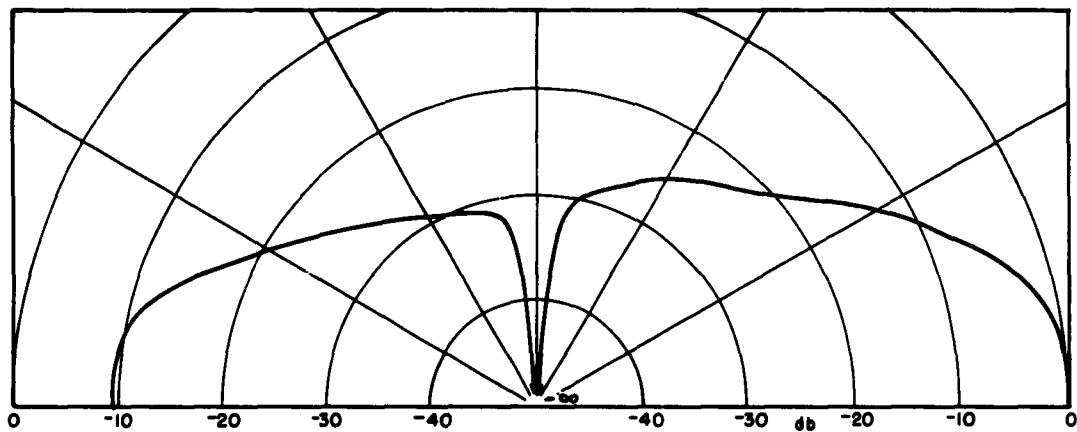
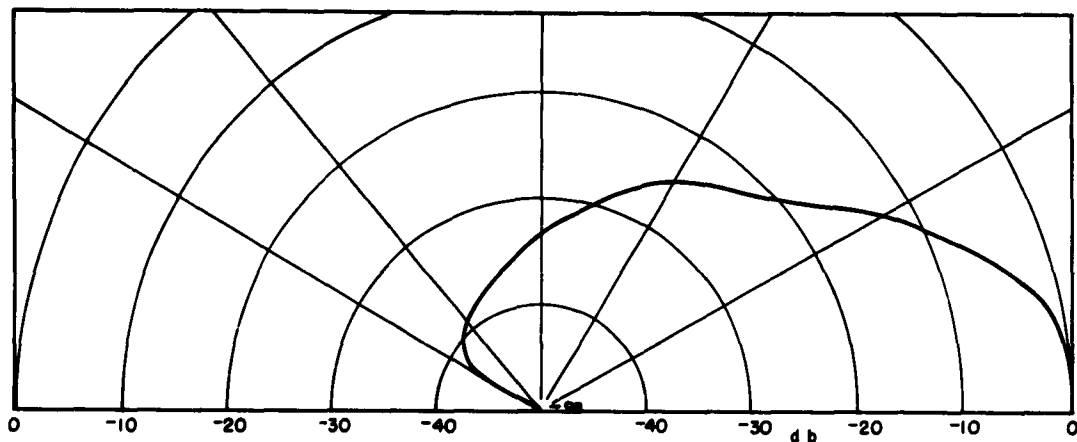


Fig. II.16. Directivity pattern for two four-hose batteries, combination A -  $\beta$ ,  $k_0 a = 0.1$ ,  $n = 34$ ,  $c_1/c_0 = 0.5$ ,  $\mu = 0.10$ .



**Fig. II.17. Directivity pattern for two four-hose batteries, combination B -  $\beta$ ,  $k_0 a = 0.1$ ,  $n = 34$ ,  $c_1/c_0 = 0.5$ ,  $\mu = 0.10$ .**



**Fig. II.18. Directivity pattern for two four-hose batteries, combination A -  $\gamma$ ,  $k_0 a = 0.1$ ,  $n = 34$ ,  $c_1/c_0 = 0.5$ ,  $\mu = 0.10$ .**

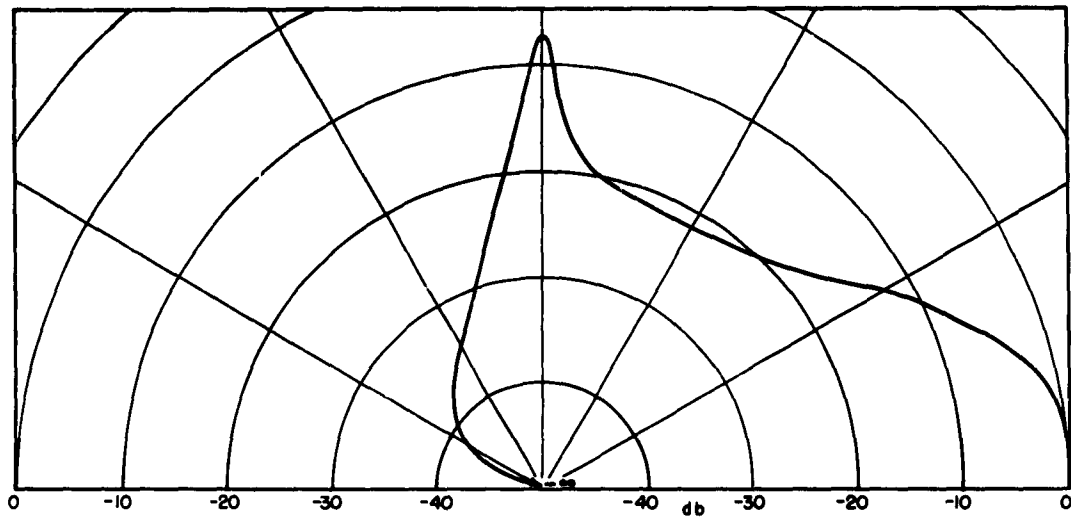


Fig. II.19. Directivity pattern for two four-hose batteries, combination B - $\gamma$ ,  $k_o a = 0.1$ ,  $n = 34$ ,  $c_1/c_o = 0.5$ ,  $\mu = 0.10$ .

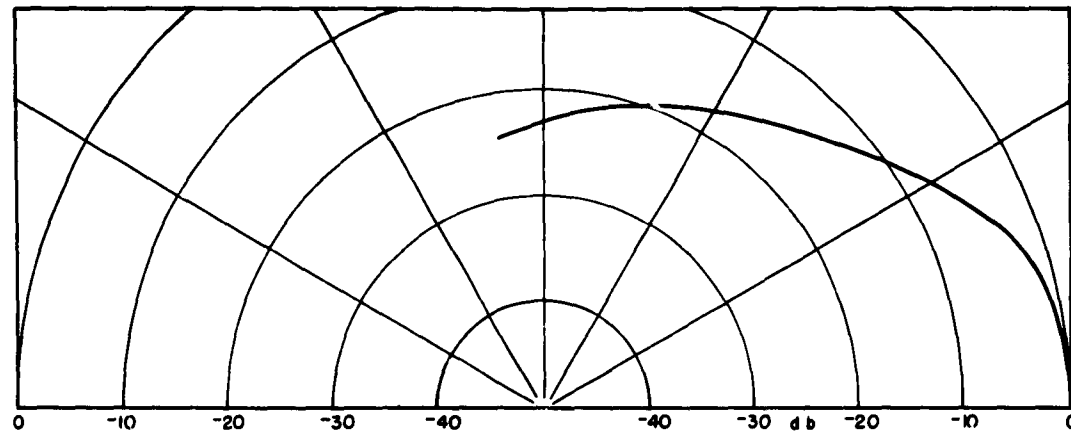


Fig. II.20. Directivity pattern for a four-hose battery, combination A,  $k_o a = 0.1$ ,  $n = 18$ ,  $c_1/c_o = 0.5$ ,  $\mu = 0.189$ . Even though the hose length is nearly halved, end-fire directivity is not considerably less than for the pattern in Fig. II.11.

## Chapter III.

Experimental Verification of the TheoryNature of the Experiments

The most interesting application of the end-fire source is its use as an underwater sound source. However, the theory developed in the preceding chapter is valid both for liquid and for gaseous media. It was therefore decided to carry out the experimental verification of this theory in air, since facilities for such tests were immediately available.

The tests were performed in the anechoic chamber of this Laboratory by means of the installation to be described in the next section. In these tests, the conditions which could be controlled were the frequency, and the quantities  $c_i$  and  $\rho_i$  (by filling the hose with a predetermined mixture of air and helium). The actual value of  $c_i$  was obtained experimentally, as was the value of the attenuation  $\mu$ ; these two quantities were then used to compute the theoretical directivity patterns which were to be checked against the experimental patterns. The experimental measurements were therefore of two types: (1) measurements of  $c_i$  and  $\mu$ , and (2) recording of the directivity patterns.

Description of the Experimental End-Fire Source

The radiating surface of the source consisted of a hose which was built up by winding a strip of "saran" (vinylidene chloride) on a brass rod, in helical form. The saran strip had previously been painted with cement over a width of approximately 1/8 in. adjacent to the edge of the strip; since the coils of the helix overlap slightly, an airtight cylindrical surface is thus formed. The brass rod was then removed. The diameter of this hose is 0.616 in. and its length 51 in. The hose wall thickness is 0.0007 in. The hose is terminated by a brass plug. In view of the reflective character of this termination, this end-fire source is of the standing-wave type. A slight tension is applied to the hose by means of a tension spring acting on a thin rod screwed into the brass plug. (cf. Fig. III.1). This rod is freely supported by two pulleys.

The driving end of the hose is cemented to a brass tube which, in turn, is connected to a Western Electric type-555 loudspeaker. The sound waves generated by this source travel up the relatively rigid brass tube, without appreciable attenuation. For the values of  $k_0$  encountered in these tests, only the zero-order, quasi-plane mode is capable of propagation. (cf. next chapter). This system is mounted on a turntable supported by a carriage; hence both translational and rotational motion are possible.

The pressure in the saran hose is controlled as follows: Air from the high-pressure air main is fed through a regulating valve into a rubber hose which is terminated by a Y-type connector, one branch of which leads to the brass tube-saran hose system. The other branch performs the function of a vent opening to a water column in a graduated glass. By adjusting the regulating valve so as to cause slowly-forming bubbles to emerge from this vent, the gas pressure of the system, measured in inches  $H_2O$ , is approximately equal to the height of the water column above the vent. The gas pressure can thus be conveniently controlled by varying the amount of water in the graduated glass. During tests, the gaseous contents of the system are constantly renewed by allowing the gas to escape through a small exhaust vent in the terminating plug, thus causing the gas to flow down the saran hose at a slow rate. This arrangement is actually intended for tests where not pure air but an air-helium mixture is used, so as to avoid a gradual change in the proportions of the two gases owing to helium's greater ability to diffuse through the saran membrane.

Owing to the elastic character of the saran hose, the zero-order mode phase velocity for waves travelling along the gas column is somewhat smaller than the sound velocity in the surrounding space when pure air is used in the tube-hose system (cf. Chap. IV). In order to raise the phase velocity to the value of, or somewhat above, the sound velocity in air, it is necessary to introduce a small proportion of helium into the air in the system. The desired ratio of the two gases is achieved by feeding each of them into a balloon, and by controlling their rate of flow (by means of a rotormeter) and the time interval of flow (by means of a stopwatch). The gaseous mixture is then fed into the system by applying an appropriate pressure to the balloon; the pressure in the system is again controlled by

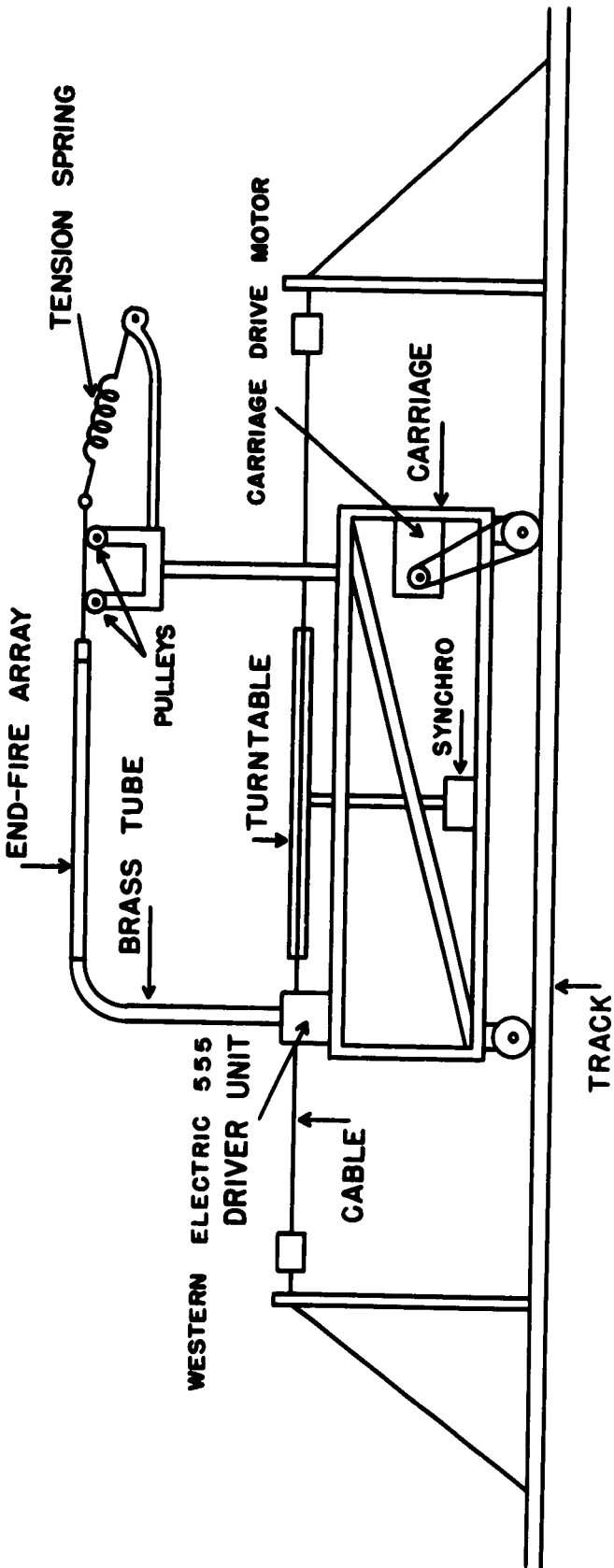


Fig. III.1. Experimental installation for the study of an end-fire source in the anechoic chamber of this laboratory. The arrangement pictured here, which permits the carriage to travel along the track, is used for the measurement of the phase velocity  $c_1$  and the attenuation  $\mu$  per wave length. An alternative arrangement, permitting rotation of the turntable, is used in the observation of directivity patterns.

means of the water pressure above the vent opening into the graduate.

### Instrumentation

In the first test, the phase velocity  $c_1$  and the attenuation  $\mu$  are measured by recording the axial pressure distribution of the standing wave system in the saran hose. The sound pressure is measured by a small microphone located at right angles and close to the saran hose (cf. Fig. III.2); during the test the hose is made to travel at a steady rate past the microphone. A record of sound pressure versus axial displacement is thus obtained, from which it is possible to calculate  $c_1$  and  $\mu$ .

The translational motion of the saran hose is brought about by causing the carriage which carries the hose to travel along a track coinciding with one axis of symmetry of the anechoic chamber (cf. Fig. III.3). The carriage is driven by a motor connected to one of the wheels by means of a belt (cf. Fig. III.1). This sketch also shows that the translational motion of the carriage is related to the rotational motion of the turntable by means of a wire causing the turntable to turn as the carriage moves. The rotation of the table is fed into a synchro which correlates it with the signal from the microphone. The carriage drive motor is controlled by a servo amplifier (cf. Fig. III.2).

The microphone, which is wrapped, like most other testing equipment, in glass fiber to minimize sound reflection, receives the pressure signal through a small probe extending to approximately 1/2 in. of the hose wall. The microphone signal is amplified and processed by a UTC-4C filter. It then actuates a power level recorder which is linked to a synchro which in turn is connected to the turntable synchro and to the servo-amplifier (cf. Fig. III.2). The recording system described traces a record of sound intensity versus carriage (or turntable) position.

Directivity patterns of the end-fire source are obtained by rotating the source and measuring the sound pressure by means of a stationary microphone located at the far end of the track (cf. Fig. III.4: in this photograph the track is covered with a layer of glass fiber). The distance from the source to the microphone is at least 120 wavelengths, thus justifying the "far-field" assumption. Since the source, and hence the

sound field, are symmetrical with respect to the cylindrical axis, it is sufficient to explore the sound field in one, viz., the horizontal plane. Rotation of the saran hose is achieved by mounting the loudspeaker and brass tube at the hub of the turntable. The rotational position of the table is correlated with the microphone signal as in the preceding test.

#### Observed Directivity Patterns

Figures III.5 and III.6 show directivity patterns for a saran hose filled with pure air; as mentioned earlier, the ratio  $c_1/c_0$  is less than unity in this case. The values of  $\mu$  and  $c_1$  given in these figures are experimental and were measured in the way described in the preceding section. The value of frequency (and hence of  $k_0 a$  and  $n$ ) was obtained by comparing the loudspeaker input with a standard frequency signal. The smooth curves in Figs. III.5 and III.6 are directivity patterns computed by means of Eq. (II.18) and using the observed values of  $c_1$  and  $\mu$ . The agreement of the experimental and theoretical curves will be discussed in the next section. The directivity of these patterns could have been improved by using a value of  $c_1/c_0$  of exactly unity and a somewhat longer source.

Figures III.7 and III.8 show directivity patterns obtained when  $c_1/c_0 > 1$ , i.e., when a small amount of helium is mixed with the air in the saran hose. The two prongs in the pattern may be interpreted as the trace of the approximately conical wave produced by the source under these conditions (cf. Chap. I).

When the sound waves travelling up the brass tube are allowed to radiate directly into space, without the intermediary of the saran hose, the mouth of the brass tube constitutes a sound source approximately equivalent to a vibrating, circular, baffleless piston. The directivity patterns produced in this fashion at the two test frequencies are shown in Fig. III.9. They are almost completely nondirective, as was to be expected from the small values of  $k_0 a$ . Comparison of this figure with the four preceding ones illustrates how a nondirective source can be made directive by the simple device of using it to drive an end-fire source, instead of allowing it to radiate directly into space.

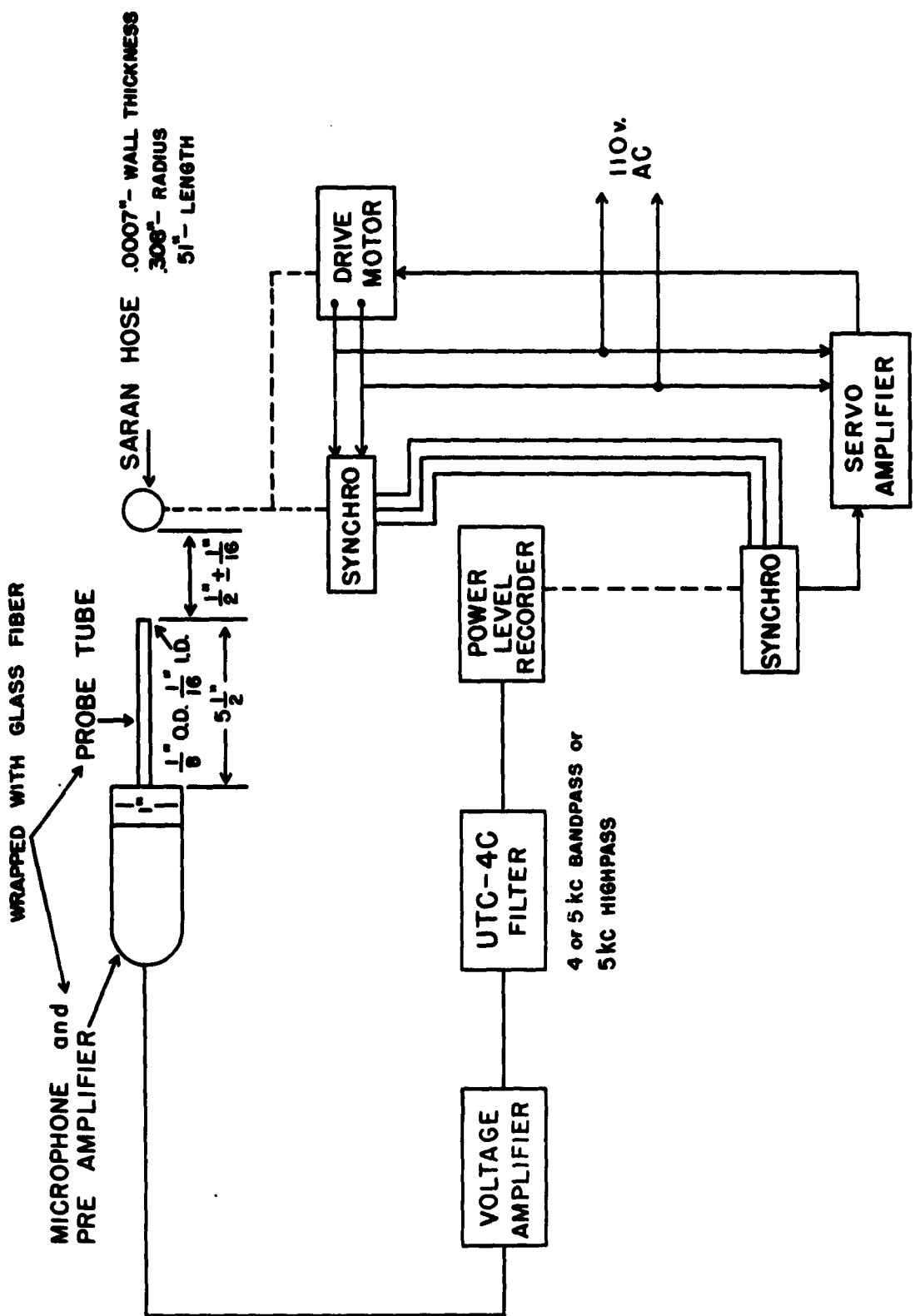


Fig. III.2. Experimental setup for the measurement of the phase velocity  $c_1$  and the attenuation per wave length  $\mu$  in the Saran hose (electronic circuit).

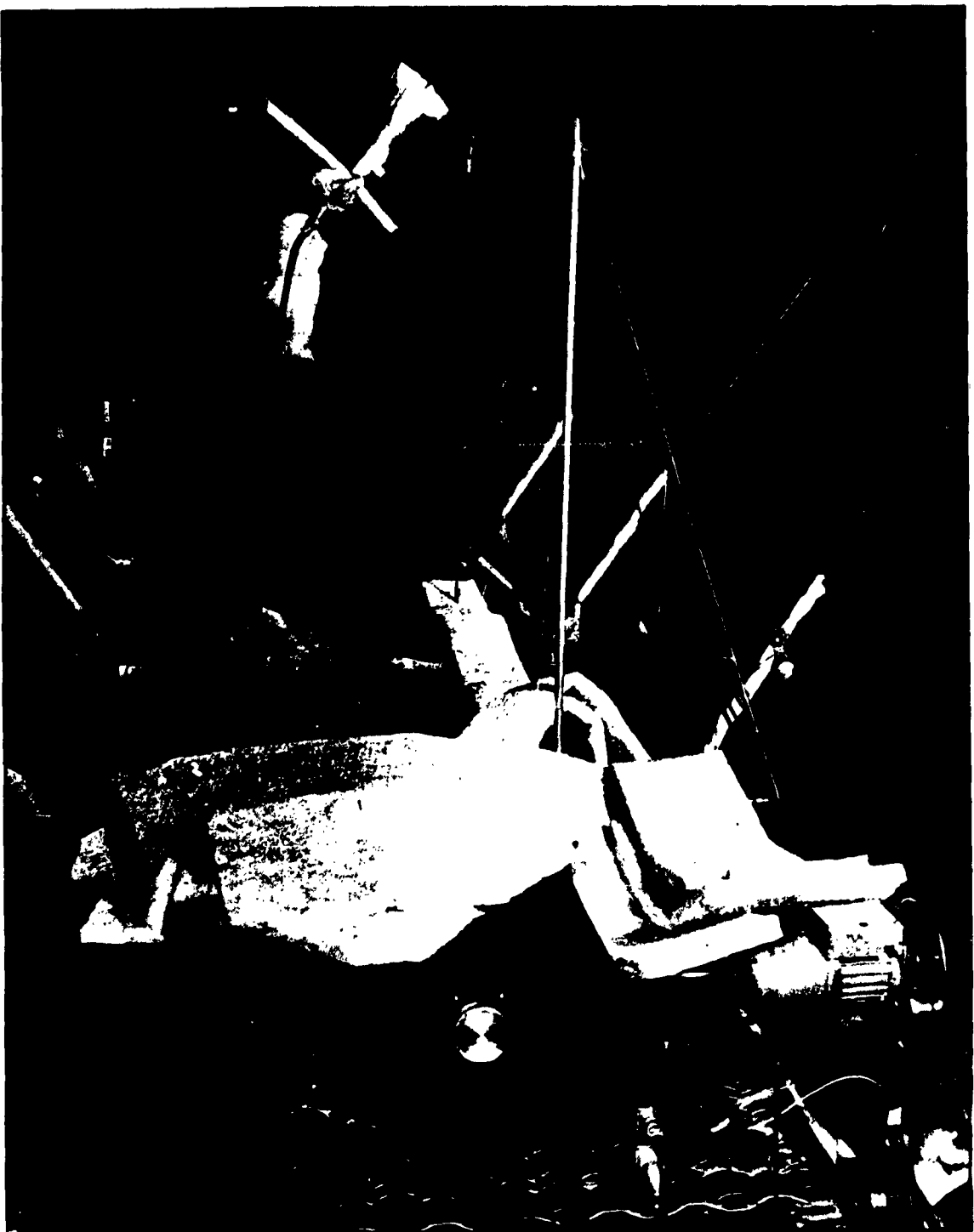


Fig. III.3. Experimental installation for the measurement of  $c_1$  and  $\mu$  in the Saran hose. The carriage and microphone are covered with sound absorptive material. During the test, the microphone, which is mounted on a tripod, remains stationary, while the Saran hose, which is attached to the carriage, travels past the microphone probe (the probe is the narrow tube pointed at the hose).

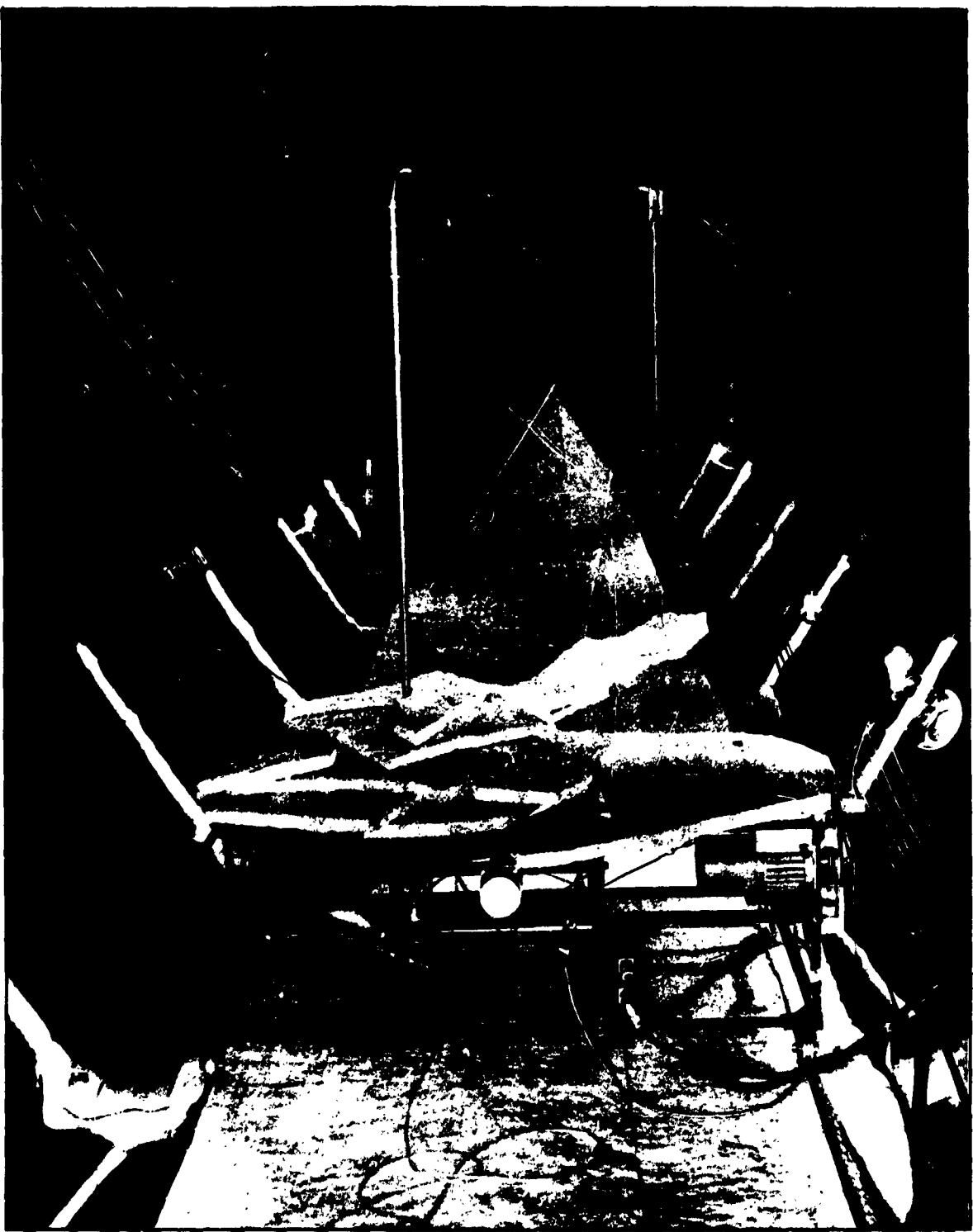


Fig. III.4. Experimental installation for the observation of directivity patterns. The stationary microphone is seen at the far end of the track (which is covered with absorptive material). The brass tube leading to the Saran hose is mounted at the hub of the turntable; during the test, the table rotates.

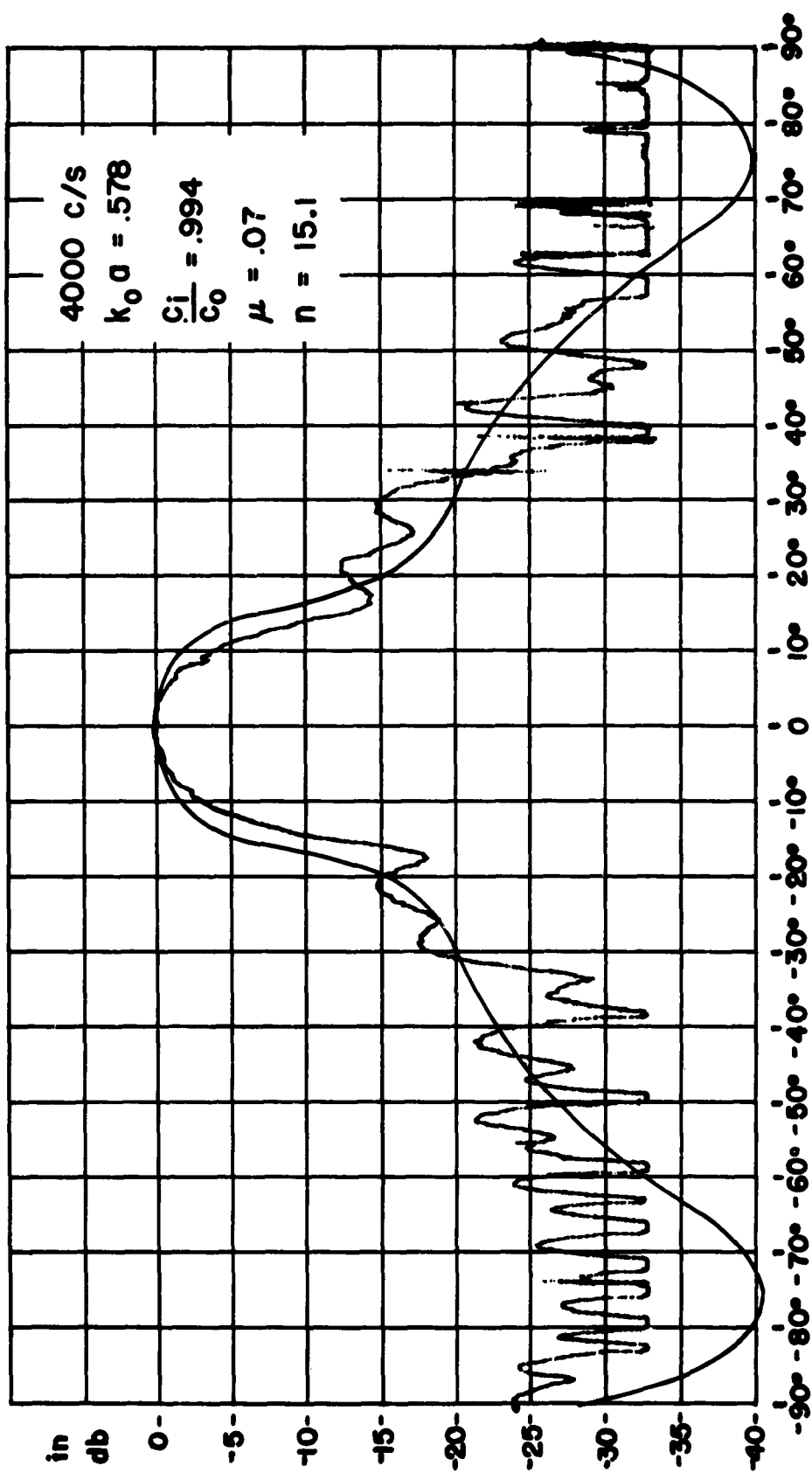


FIG. III.5. Directivity patterns for the condition  $c_1 < c_0$ . The smooth curve is theoretical, the irregular curve experimental. The low intensity curve is "smooth" in the observed pattern is probably caused by reflection from equipment in the chamber. The frequency is 4000 c/s,  $k_0 a = 0.578$ ,  $C_1/C_0 = 0.994$ ,  $\mu = 0.07$ , and  $n = 15.1$ .

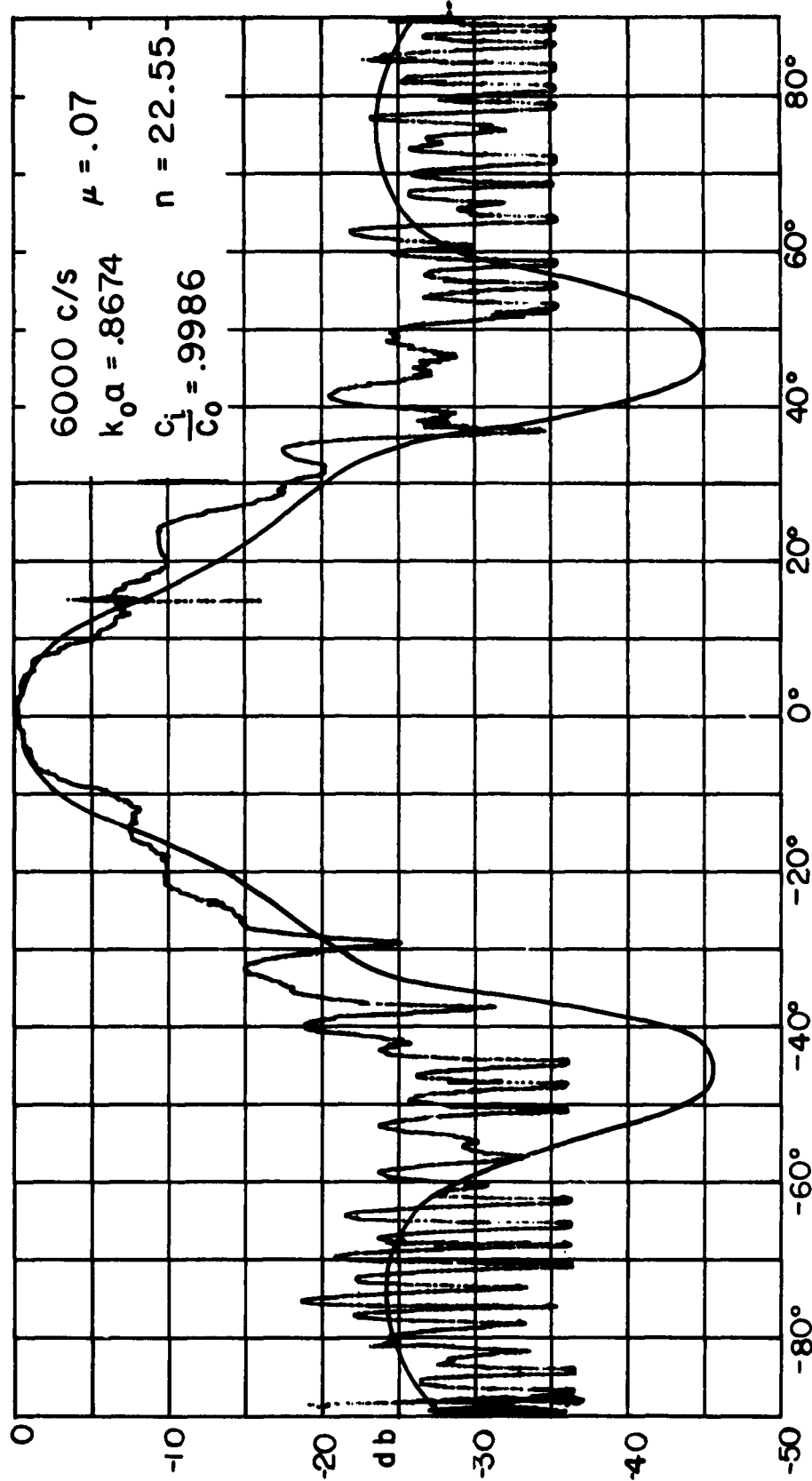


Fig. III.6. Observed and computed directivity patterns for the condition  $c_1 < c_0$ .  
 The frequency is 6000 c/s,  $k_0 a = 0.867$ ,  $c_1/c_0 = 0.99$ ,  $\mu = 0.07$ , and  $n = 22.55$ .

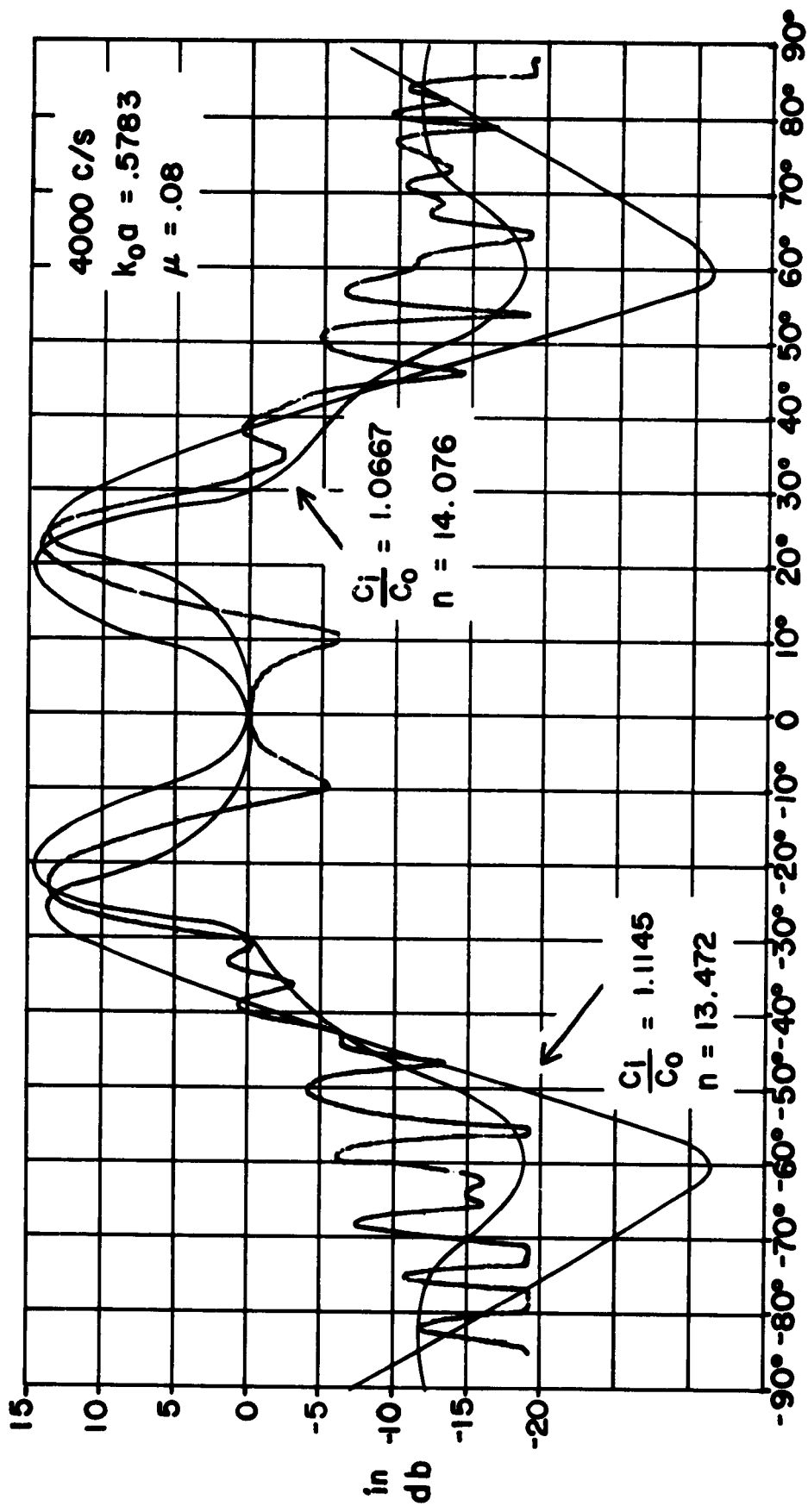
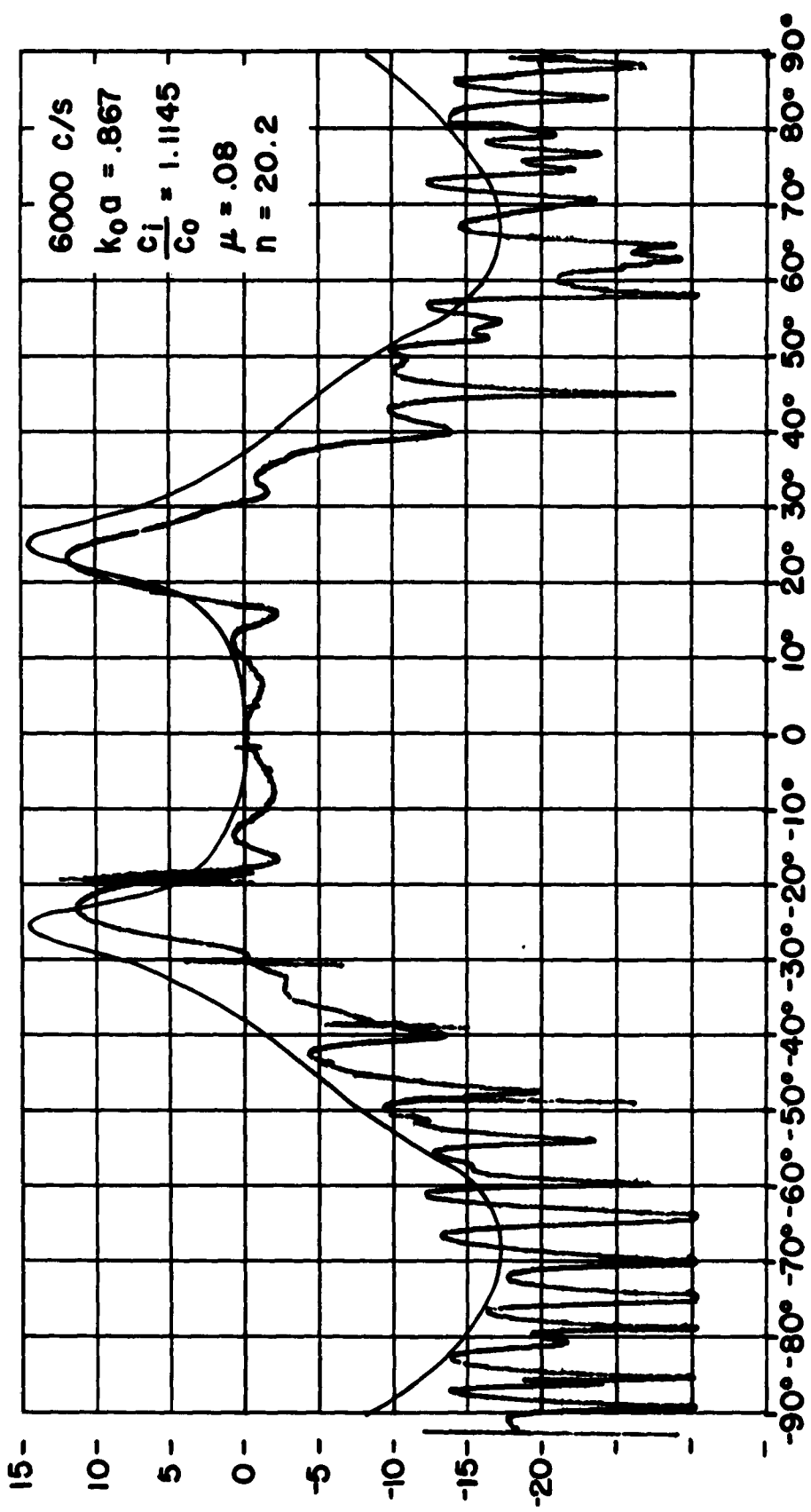


FIG. III.7. Observed and expected directivity patterns for the conditions  $n > 0$ .  
 The two ranges which characterize this condition and which are the trace of the overall state in the normalized plane are clearly visible. The two theoretical patterns are based on the two smallest different values of  $n$ , (and therefore of  $\mu$ ) which were observed for the test conditions. The frequency is  $4000 \text{ c/s}$ ,  $k_0 d = 0.578$ ,  $\alpha_i/\alpha_o = 1.115$ ,  $\mu_i = 0.08$ ,  $n = 13.471$  to  $14.081$ .

Hg, Hg.8. observed and calculated absorption rate in the condensation  $\theta_1 > 90^\circ$ .  
The frequency is 6000 c/s,  $\lambda_0 = 0.867 \text{ } \mu\text{m}$ ,  $\alpha = 20.2$ .



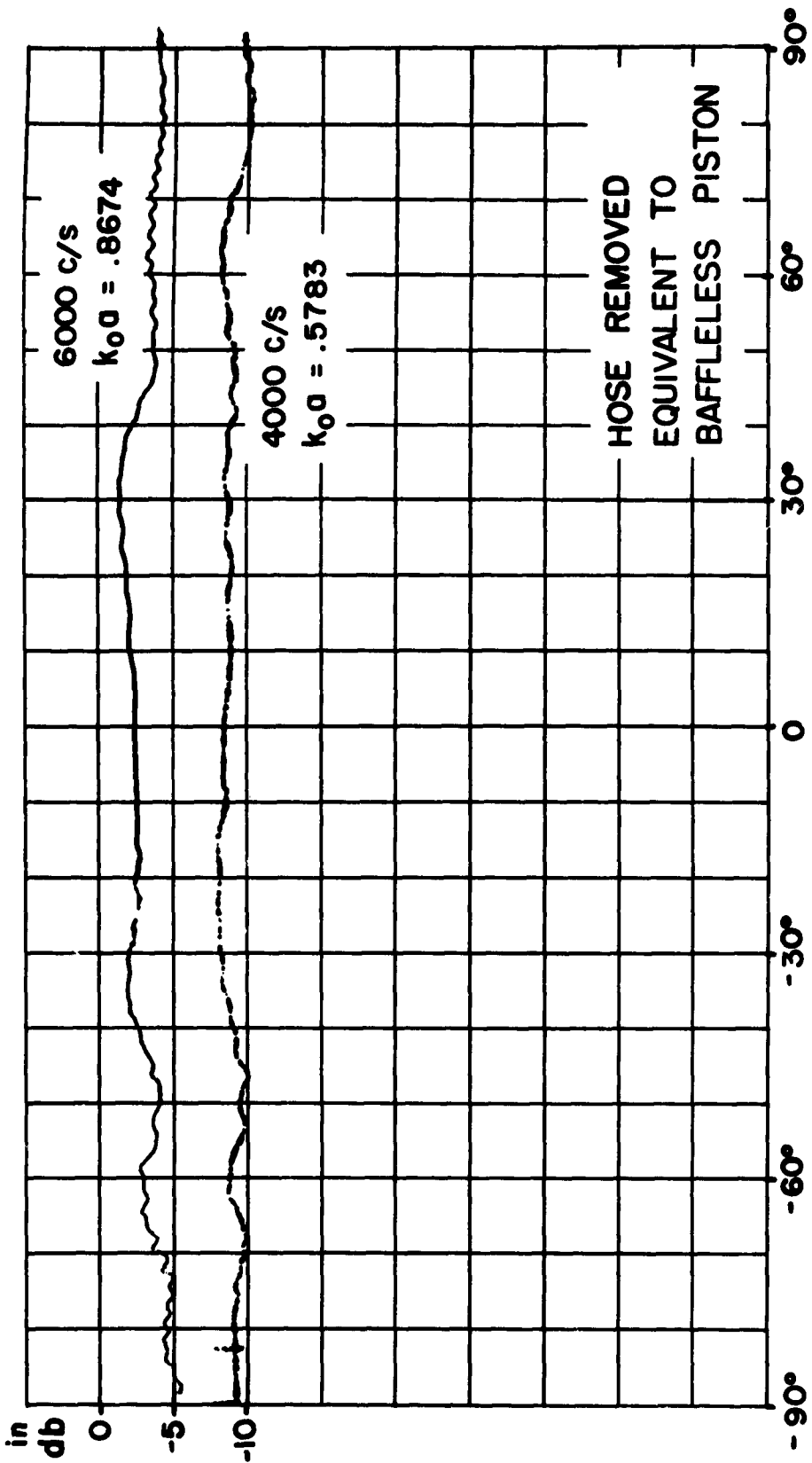


Fig. III.9. Directivity patterns observed when the brass tube mouth relates directly into space instead of into the Seran hose. The tube mouth is equivalent to a source in the form of a baffleless piston. The patterns are completely non-directive, as expected from the small values of the test frequencies and source diameter. The frequencies are 4000 and 6000 c/m, and  $k_o a = 0.578$  and  $0.867$ . This figure illustrates how a non-directive source can be made directive by coupling it to the surrounding medium by means of the end-fire source.

Discussion of Experimental Results

Comparision of the theoretical and experimental patterns in Figs. III.5 - III.8 shows good agreement in the region where the sound pressure is high; i.e., in the on-beam region. The lack of agreement in the off-beam region, where the sound pressure is low, is probably due to scattering from the test rig (i.e., to the insufficiently anechoic behavior of the test area) and to other sources of noise. This is suggested by the "hash"-like appearance of the experimental pattern in this off-beam region. Owing to the very low sound level prevailing there, this discrepancy between observed and theoretical values is of little importance.

A great difficulty in comparing theoretical and observed directivity patterns is that the present experimental set-up yields only inaccurate values of  $\mu$ . This is due to the fact that the system supporting the hose, as well as the hose itself, tends to sway back and forth when the carriage is set in motion. As a result, the distance between the hose wall and the microphone probe varies, thus causing pressure variations not related with the axial pressure distribution in the saran hose. These variations could be minimized if it were possible to locate the probe at a greater distance from the hose. However, this would introduce even greater difficulties in that the sound field several inches away from the hose wall is not related in a simple way to the axial pressure distribution in the hose, since all elements of the hose contribute to it. When, accidentally, vibrations were avoided over a significant portion of the total length of travel of the carriage, the pressure recorded did approach the form of a hyperbolic cosine, as stipulated by Eq. (II.11) (cf. Fig. III.10). Unfortunately, the record in Fig. III.11 is far more typical. In a badly distorted record such as this one, it is still possible to obtain accurate readings of wavelengths, i.e., of  $c_i$ . This is illustrated in Fig. III.12, where a number of readings of  $c_i$  are plotted as a function of the pressure in the saran hose for different values of helium to air mass ratio  $r$ . (It is seen, by the way, that the pressure has only an insignificant effect on  $c_i$ .)

A record such as the one in Fig. III.11 can be used to obtain a value of  $\mu$  by analyzing the envelope of the curve in those sections where the pressure record seems not to have been disturbed by vibration, i.e., in sections

showing an approximately exponential decay. Figure III.13 indicates the seriousness of the inconsistencies found in a typical set of data. These points show only a small fraction of the experimental data; in general, no consistent variation of  $\mu$  with pressure, mass ratio of helium to air, or even frequency within the 4000-6000 c/s range, could be detected. Owing to this inconsistency in the observed values of  $\mu$ , the following procedure has been adopted: When the two or three values of  $\mu$  measured under test conditions corresponding to those of the particular directivity pattern under investigation show reasonable agreement, their average value is used in computing the theoretical directivity patterns. If, however, the data are widely scattered, those points whose contribution to the average value of  $\mu$  would result in poor agreement between the experimental and theoretical directivity patterns are omitted. This procedure is obviously purely heuristic, but it may be justified by the following considerations: (1) when consistent values of  $\mu$  are obtained, their average value does lead to a theoretical directivity pattern which is in good agreement with the experimental pattern; (2) an inaccurate value of  $\mu$  will, in general alter the directivity pattern less than a wrong value of  $c_i/c_o$ ; (3) elimination of the difficulty underlying the measurement of  $\mu$  (i.e., vibration of the hose) requires laborious and time-consuming changes in the whole test rig, such as elimination of play between the carriage wheels and track, a gradual starting up of the carriage, etc. The accuracy of these tests could be improved by measuring the pressure along the cylindrical axis by means of a small movable probe supported by a sleeve at the center of the brass plug which terminates the hose.

It is found that the pressure in the hose, and the axial tension applied to the hose, have no consistent effect, provided they are sufficiently large to insure that the hose wall is smooth and devoid of creases. When this is not the case, the directivity pattern observed is nondirective; when  $c_i/c_o > 1$ , i.e., when the pattern (as in Fig. III.8) displays two prongs, the prongs are blunt instead of slender. This condition indicates excessive attenuation, probably caused by frictional effects in the creased saran wall.

Finally, it should be added that many directivity patterns were observed which are not given here, and which were not checked against a computed

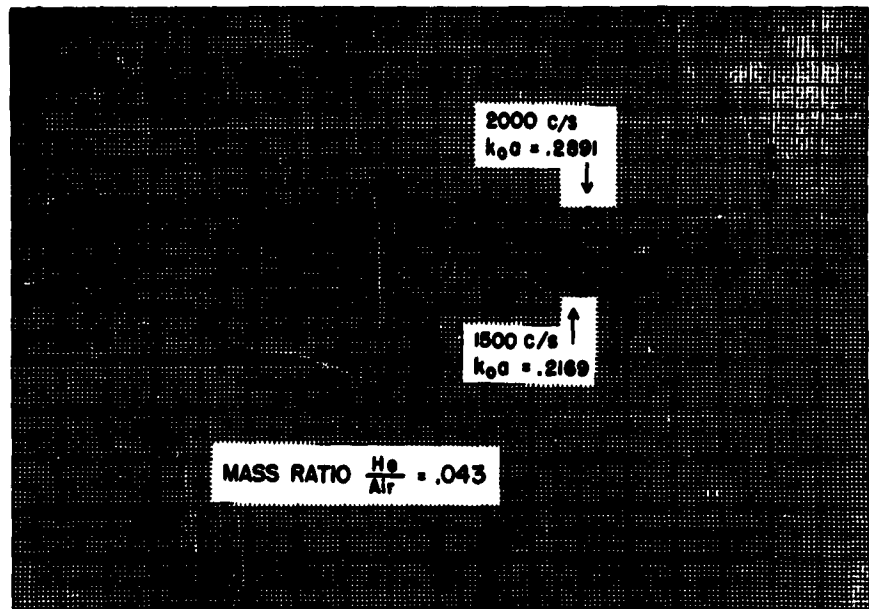


Fig. III.10. Observed axial pressure distribution along the Saran hose , in the form of a hyperbolic cosine. This type of record is used to measure  $\lambda_1$  (i.e.  $c_1$ ) and  $\mu$ . The frequencies are 1500 c/s ( $k_0a = 0.217$ ) and 2000 c/s ( $k_0a = 0.289$ ). The phase velocity was raised above that in air by using a mixture of helium and air (mass ratio He/air = 0.043) .

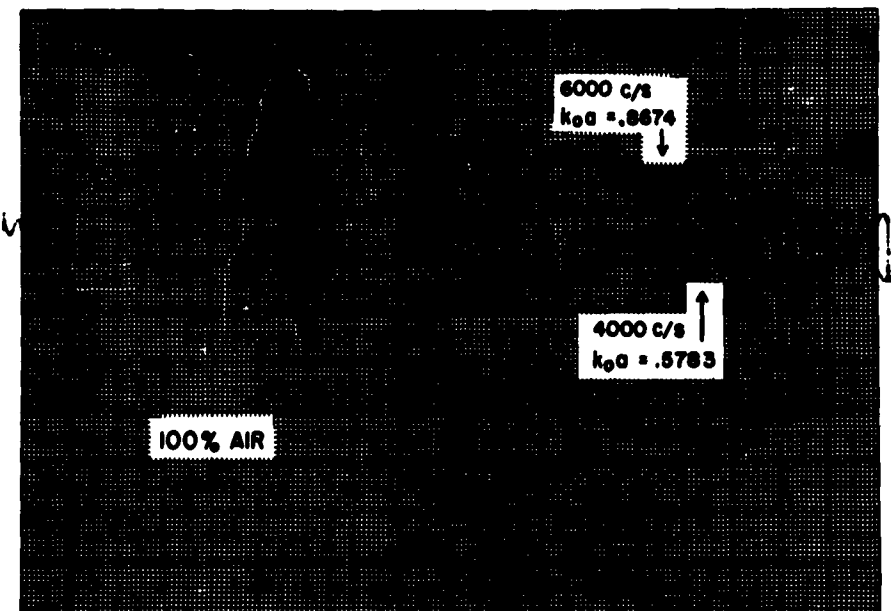


Fig. III.11. Observed axial pressure distribution along the Saran hose illustrating the disturbing effect of the variation in distance between the hose wall and the microphone probe caused by swaying of the brass tube-hose system. The frequencies were 4000 c/s ( $k_0a = 0.578$ ) and 6000 c/s ( $k_0a = 0.867$ ). Pure air was used in the hose.

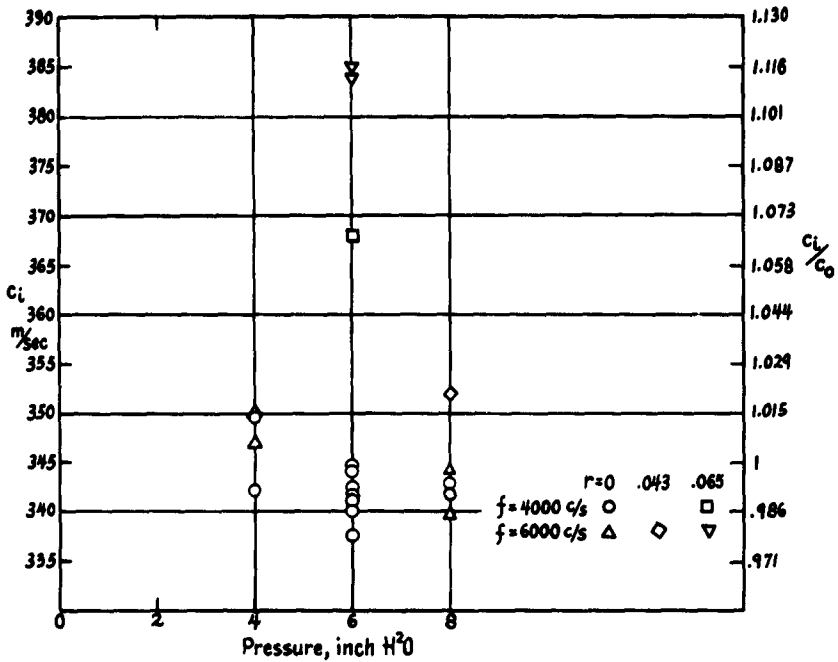


Fig. III.12. Phase velocity of the zero-order mode in a standing-wave source in the form of a Saran hose surrounded by air and filled with air or a mixture of helium and air ( $r$  = mass ratio He/air); the abscissa indicates the pressure in the hose. The wall thickness is 0.0007 in., the radius 0.308 in. It is seen that the scatter of points for a given value of  $r$  is relatively small.

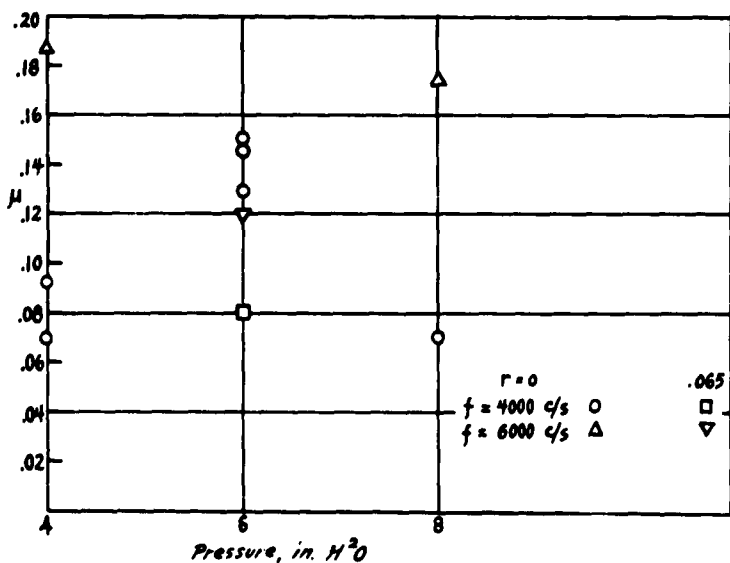


Fig. III.13. Attenuation per wave length  $\mu$  in a standing-wave source in the form of a Saran hose surrounded by air and filled with air or a mixture of helium and air; the abscissa indicates the pressure in the hose. The wall thickness is 0.0007 in., radius 0.308 in. The scatter is seen to be considerable.

pattern because of the great amount of labor involved in carrying out the necessary calculations. These experimental patterns show good consistency and were reproducible without difficulty.

## Chapter IV

Design of an End-Fire Source for Use Under WaterNature of the Design Problem

A practical design of a low-frequency end-fire source for use under water will now be discussed. Essentially, the problem is to determine the most convenient means of building a device endowed with physical parameters having the values required for good directivity. It was found in Chapter II that the conditions to be fulfilled are:

- (1)  $c_i/c_o \approx 1$ , i.e.,  $c_i \approx 1.5 \times 10^5$  cm/sec (except for the source in the form of a battery of partly occluded cylindrical radiators, where  $c_i \approx 0.75 \times 10^5$  cm/sec).
- (2)  $n$  larger than a certain minimum value which varies inversely as  $\mu$  (of the order of 15 to 35).
- (3) a relatively small value of  $\mu$  (viz., of the order of 0.05 to 0.12)

Condition (3) is relatively easy to satisfy. It is simply a matter of not allowing the energy in the source to escape too rapidly into the surrounding medium. The factors determining  $\mu$  will be discussed later in this chapter. The practical lower limit of  $\mu$  is determined by the attenuation associated with internal friction in the source. Obviously the attenuation owing to radiation should be considerably larger than that caused by friction, if the source is to be efficient. If the source is in the form of a solid elastic cylinder this requirement may be quite difficult to satisfy.

Condition (2) can be complied with by using a sufficiently long source. At low frequencies and when a very small value of  $\mu$  is selected as to achieve high directivity, the source may be impracticably long. Otherwise, this requirement does not present any difficulty.

In contrast, condition (1) is quite difficult to satisfy. The difficulty is two-fold: (a) few liquids have a sound velocity as high as that of water; it is therefore difficult to achieve a fluid-filled elastic hose which will permit waves to propagate in the zero-order mode with a sufficiently large phase

velocity (higher modes of propagation are inconvenient for several reasons; see below for a discussion of the mechanism of propagation). (b) in order to take advantage of the fact that the directivity pattern does not depend appreciably on frequency (or, more exactly, on  $k_0 a$ ) the phase velocity  $c_i$  should also be frequency-independent in the region of operation; this would permit operating the device over a certain range of frequencies without a change in the directivity pattern. Since the mechanism of wave propagation in fluid-filled hoses, elastic rods, etc. is in general dispersive, a system must be used whose dispersion curve is level in the desired range of operating frequency.

Different systems will now be considered to determine to what extent they lend themselves to our purpose.

#### Solid Cylindrical Rods

In view of the first difficulty mentioned, i.e., the large value of  $c_o$ , the first thought that comes to mind is to approximate a phase velocity  $c_i$  of the order of  $1.5 \times 10^5$  cm/sec by using elastic waves in a solid, elastic, cylindrical rod or shell constructed of metal or of some synthetic substance.

In the case of solid cylinders, only longitudinal waves are appropriate as flexural waves result in a dipole effect; torsional waves are not suited, because the essentially tangential motions they generate do not cause sound radiation. The propagation of longitudinal waves in cylinders has been the subject of much research. Among the most recent investigations is the one by Davies [8], which is analytical and experimental, and the one by Holden [9], which is analytical. The general problem is summarized in Chapter III of reference [3]. The effect of the surrounding medium on the wave propagation has been analyzed by the author (to be published).

The dispersion curves of the first three longitudinal modes as given by Davies [8] are reproduced in Fig. IV.1. The first mode appears to be better suited for our purpose because it is nondispersive over a wide frequency range and because its stress distribution is simpler than that of the higher modes (it has at most one nodal circle, while the second mode has one or two nodal circles, and so on). This mode is therefore easier to excite and frictional losses may be expected to be smaller. One of the two frequency

ranges where the first mode has a fairly frequency-independent phase velocity is approximately defined by the inequality  $(a/\lambda_i) > 0.8$ . An additional incentive for working in this region is that the longitudinal wave is of the nature of a Rayleigh surface wave. The stresses accompanying such a wave are actually restricted to the outer skin of the rod, i.e., to the region which is instrumental in radiating to the surrounding medium. This situation is very desirable because the energy dissipation by friction in the metal is kept at a minimum. The phase velocity in this frequency region is also that of the Rayleigh wave (i.e., of the order of 0.6 c<sub>B</sub>). Since this phase velocity must be equal to  $1.5 \times 10^5$  cm/s, we can solve for the "bar velocity" c<sub>B</sub> and note that this quantity must be of the order of  $2.5 \times 10^5$  cm/s. This leaves tin as the only suitable metal. There are, of course, a great number of plastics which have the desired bar velocity. From the condition that  $(a/\lambda_i) > 0.8$ , we can solve for the rod diameter D (= 2a) as a function of the minimum desired operating frequency (i.e., the frequency for which  $a/\lambda_i = 0.8$ ). Taking  $\lambda_i = 1.5 \times 10^5/f$ , the required diameter in cm is found to be

$$D = 2.4 \cdot 10^5 / f \quad (\text{IV.1})$$

It is seen that even for a 1-ft rod the minimum frequency would be 8000 c/s. Hence this approach is not practical if one wishes to operate at low frequency.

A further difficulty is that, for efficient operation, the rod must be driven by a transducer approximately conforming to the Rayleigh wave stress distribution, so as to avoid exciting the higher modes to an appreciable extent. This could be achieved by using a transducer in the form of an annulus exciting only the peripheral region of the cylinder.

Inspection of the dispersion curves in Fig. IV.1 suggests that a source suitable for very low frequencies could be achieved by using the other plateau displayed by the first mode curve in the region  $0 < a/\lambda_i < 0.1$ . The relation between the rod diameter in cm. and the maximum operating frequency f<sub>max</sub> (i.e., the frequency for which  $a/\lambda_i = 0.1$ ) is found to be

$$D = \frac{3.0 \cdot 10^4}{f_{\text{max}}} \quad (\text{IV.2})$$

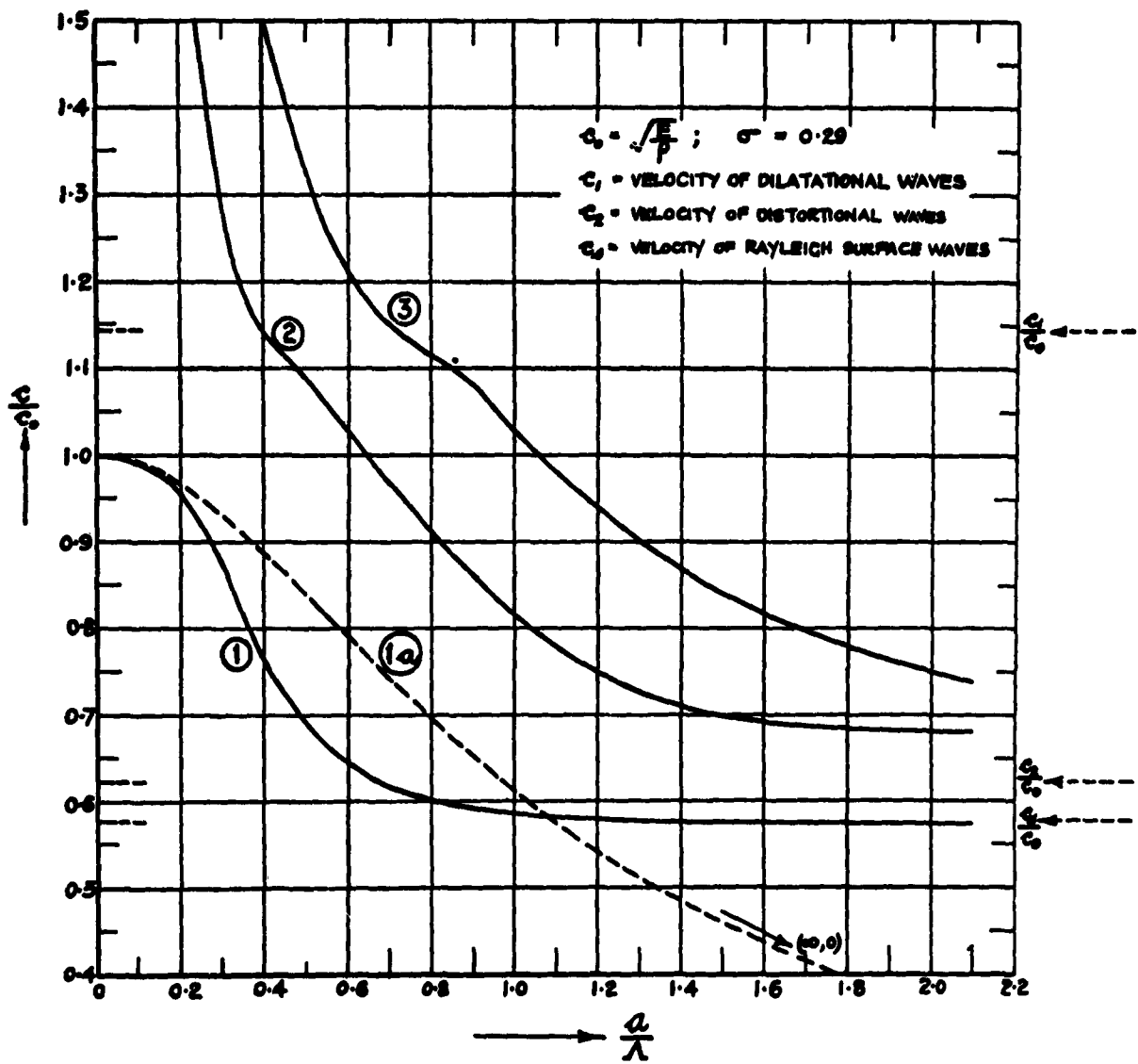


Fig. IV.1. Dispersion curves of the first three modes of propagation for longitudinal waves in an infinite, elastic cylinder, reproduced from a paper by Davies (8). The phase velocity is  $c$ , which in the notation used in this memorandum is designated by  $c_1$  or  $c_2$ .  $\lambda$  is the corresponding wave length, i.e.  $\lambda_1$  in the present notation. The curve labeled (la) is based on Lord Rayleigh's approximate theory.

It is seen that even if it is required that the end-fire source operate up to 1000 c/s the diameter would not have to exceed 1 ft; in other words, the restriction imposed by the condition  $a/\lambda_i < 0.1$  is in practice no restriction at all in that it does not interfere with any practical design.

Having thus disposed of the restrictions on diameter and frequency range, the designer must compare the materials having a "bar velocity" of the order of  $1.5 \times 10^5$  cm/s and determine if any of them are suitable. There are a large number of plastic materials whose "bar velocity" has the desired value. Unfortunately, most of these materials display a large amount of internal friction. At the low operating frequencies that are considered, the frictional effects are, in general, not too important; however, it must be remembered that attenuations in excess of approximately  $1-2 \text{ db}/\lambda_i$  are objectionable and that plastics are notoriously lossy. Not the least difficulty is that the information on low-frequency attenuation in plastics, and in solids in general, is exceedingly scanty.

A variant of this approach to this problem is to use a gelatin-like substance enclosed in a thin hose. Some of these substances display low attenuations and have the proper value of  $c_B$ . In a sense, this sort of a system is equivalent to a fluid-filled hose, but avoids the basic pitfall of such a system in that the cohesion of the material is inherent in the material itself, so that the stiffness of the hose wall is not required to prevent the phase velocity from dropping to very small values.

A transducer for driving such a rod should be designed to excite the whole rod section in phase and with uniform amplitude. The radial displacement at the surface is entirely caused by a Poisson-type effect which varies linearly with frequency:

$$\left| \frac{u}{v} \right| \approx 2\pi v \frac{a}{\lambda_i} \quad \text{for small } a/\lambda_i \quad (\text{IV. 3})$$

This is a regrettable situation since the radial displacement component  $u$  which is associated with sound radiation is relatively small in the lowest frequency range. This drawback is somewhat attenuated in the case of gelatin-like substances which have a Poisson ratio of nearly 1/2.

An advantage of operating near the low-frequency end of the dispersion

curve is that the higher modes are non-propagating; the dynamic configuration of the transducer need therefore not conform too closely to that of the mode to be excited.

### Cylindrical Shells

It would seem that the use of axially symmetrical flexural waves propagating along the wall of a thin shell will circumvent some of the difficulties presented by the use of longitudinal waves in a solid cylindrical rod: (1) the volume of material stressed is small, so that the attenuation owing to frictional loss is small compared to attenuation caused by radiation; in other words, stress distribution is most desirable because the material under stress lies entirely near the surface which is instrumental in radiating sound; (2) the phase velocity of flexural vibrations is determined, at least in a certain frequency range, by the ratio ( $h/a$ ); hence, by selecting a sufficiently thin-walled shell, even materials having an inherently high sound velocity, such as steel, may be used.

There exist on wave propagation in shells a paper by Giebe and Blechschmidt [10] presenting experimental results (together with an inadequate analytical study), and a recent theoretical analysis [11]. Fig. IV. 2, which is taken from the latter paper, shows the dispersion curves for the first two modes of propagation. The level region of the curve connected with the first mode is defined by the inequality  $k_w a > 1.1$ . This region seems particularly attractive for two reasons: (1) It corresponds essentially to a flexural mode producing mostly radial deformations [11], and therefore lends itself to sound radiation; (2) the phase velocity in this region is determined by the wall thickness as seen from the following approximate expression

$$c_z = \frac{c_b}{3^{1/4}} \sqrt{\frac{h/a}{(1-\nu^2)}} \quad k_w a = \sqrt{\frac{c_b h \omega}{[3(1-\nu^2)]^{1/4}}} \quad (\text{IV. 4})$$

The designer is thus free to use a material having desirable characteristics of strength, corrosion resistance, etc., and to obtain the desired phase velocity  $c_i = 1.5 \times 10^5 \text{ cm/s}$  by selecting the proper value of ( $h/a$ ). For example, if steel is selected, one finds that the wall thicknessdiameter ratio ( $=h/a$ ) must be 0.0385. This value is perfectly compatible with structural

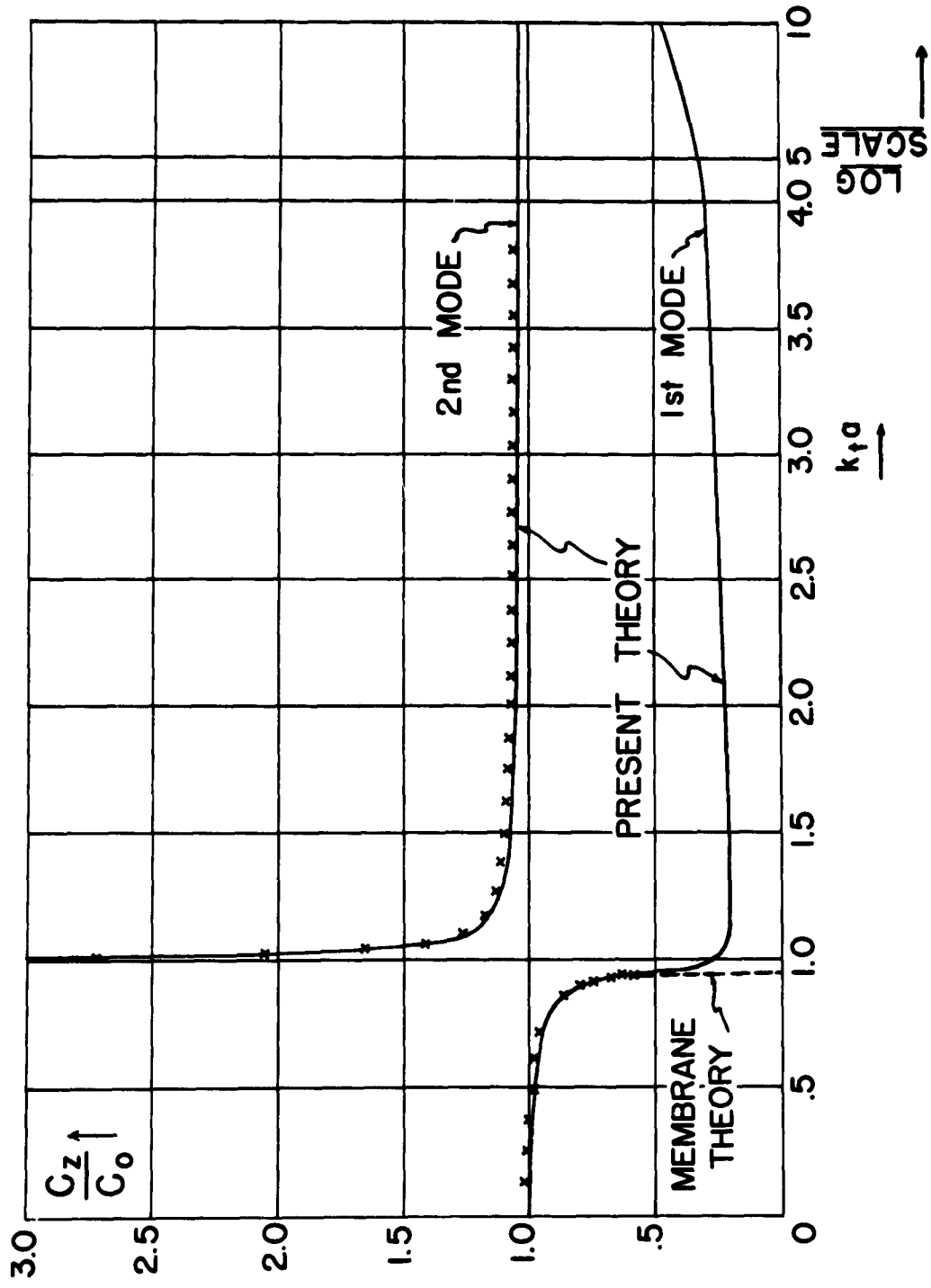


Fig. IV.2. Dispersion curves for the first two axially symmetrical modes of propagation in elastic shells, reproduced from reference (11). The symbol  $k_1$  stands for  $k_y$  in the present notation. Similarly,  $c_0$  stands for the bar velocity  $a_b$ . The first mode is predominantly longitudinal at low frequencies and flexural at high frequencies. The second mode is predominantly longitudinal.

requirements.

As in the case of elastic rods, the diameter is related to the desired frequency range by the restriction imposed on the values of  $k_w a$  (or  $a/\lambda_1$ ). Inspection of Fig. IV. 2 shows that we must have  $k_w a > 1.1$ , or (for  $\nu = 0.27$ )

$$D \geq 0.364 \frac{c_o}{f_{\max}} \quad (\text{IV. 4(a)})$$

For a one-foot steel shell, the minimum frequency is approximately 6000 c/s. This quantity is somewhat smaller than the previously found minimum frequency for the Rayleigh wave-type of mode in solid rods (the frequency limit can be reduced further by using a plastic instead of steel). If the designer is interested in this medium frequency range, the shell is much preferable to the rod: The quantity of material to be used is a small fraction of that required for the rod. This reduces cost of manufacturing and installation; it also reduces attenuation owing to internal losses. In addition, a flexural mode of this type is easy to excite; a radially expanding transducer can be used for this purpose. In summary, a thin metal shell constitutes a practical solution for producing frequencies of the order of 6000 c/s. The merit of this solution is, however, invalidated to some extent by the fact that the corresponding  $k_o a$  is large enough so that even a comparable piston-type source would be directive. However, the shell-type source still retains two great advantages over the piston-type source: (1) the directivity pattern is frequency independent over a large range; (2) the situation with respect to cavitation is very favorable, even more so than for the fluid-filled hose design since there is obviously no cavitation problem connected with the transducer driving the cylinder.

The second mode, in Fig. IV. 2 is less desirable for the medium frequency range than the first one because it excites mostly axial (i.e., nonradiating) displacement components.

In the preceding section, it was found that very low frequencies could conveniently be excited by using the initial plateau of the zero-order mode dispersion curve of the solid rod. The restrictions on the bar velocity of the material are exactly as in the case of the solid rod, i.e., metals cannot be used. The shell design also shares with the solid rod approach the inconvenience that radial displacements are very small, the ratio of radial to

axial displacement in the lowest frequency range being given again by Eq. (IV. 3). The shell does, however, possess over the solid rod the already mentioned advantages which go with a great reduction in weight. As a result, plastics, which are not suitable for the solid rod because of their large attenuations, would be acceptable for use in a thin shell. The transducer driving such a shell would be in the form of an axially or radially vibrating annulus. This is again a more desirable situation than the one encountered in the solid rod design where a piston-type transducer wastes much of its energy in exciting the inner core of the rod which is not instrumental in radiating sound energy.

In connection with the rod it was mentioned in the preceding section that a hose filled with gelatin seems a promising solution. This design might be adapted to the case of the shell by filling with gelatin the annular space between two concentric hoses.

#### The Stiffness-Controlled Hose or Tube

When attempting to realize a cylindrical surface suitable for the propagation of axially symmetrical surface waves, the most obvious approach is to use a fluid-filled tube, or a hose (the distinction drawn here between these two structures is that a tube, like a plate, possesses flexural rigidity, while a hose resembles a membrane in that it resists stretching but not bending). It can be shown that a tube filled with a fluid remains stiffness-controlled at all frequencies [11, 14]. A hose, however, becomes mass-controlled above the natural frequency of the axially symmetrical, extensional mode of vibrations.\* The low frequencies in which we are interested lie below this frequency, unless a special attempt is made to reduce the latter. Thus, a fluid-filled tube or hose may be expected to be stiffness-controlled under the conditions that interest us.

The propagation of a pressure pulse in an elastic tube is discussed by Morse (reference 7, Sect. VII. 26). A more recent analysis expresses the solution in terms of the constants of the tube [12]. Kuhl [13] gives experimental data which will be found useful in the next section. The effect of a surrounding medium on the mechanism of propagation has also been studied recently [14]. The dispersion curves of pressure waves propagating

\* The words "tube" and "hose" are used interchangeably in this section, while only the word "hose" is used in the next section.

sound velocity  $c_s$ . The use of water inside the tube is therefore excluded in favor of liquids having higher sound velocities. The zero-order mode phase velocity in the low-frequency region is related to the wall stiffness approximately as follows:

$$c_i = c_s \left[ 1 + \frac{1}{\frac{Sa(1-\nu^2)}{(k_s a)^2} - \frac{\rho_i c_s^2}{4}} \right]^{-1/2} \quad (\text{IV.5})$$

The inertial term involving  $k_s a$  is of little importance at low frequency. If it is considered that few liquids have sound velocities  $c_s$  considerably in excess of that of water, it is seen from Eq. (IV.5) that the wall stiffness  $S$  must be relatively large to prevent  $c_i$  from dropping below the desired value of  $1.5 \times 10^5$  cm/s. It is sensed intuitively, and will be shown rigorously below, that a large wall-stiffness does not permit efficient radiation of sound energy from the fluid column to the surrounding medium. The designer must therefore select the practically usable liquid with the largest sound velocity so as to keep the wall stiffness down to a reasonable value. Equation (IV.5) has been plotted in Fig. IV.4 for glycerine, a liquid which has the largest sound velocity of any common liquid ( $c_s = 1.92 \times 10^5$  cm/s). Unfortunately, glycerine is objectionable in practice because of its viscosity. It will, however, be used as a basis for the evaluation of the operating range and design requirements. It will be shown below that even for the large sound velocity of glycerine the wall stiffness, as obtained from Fig. IV.4, is objectionably large, i.e., that the lowest operating frequency of this form of the end-fire source is not sufficiently small for our purpose, even under optimal conditions. If the effect of the surrounding medium is given consideration, the situation is even more unfavorable, as the additional mass loading lowers the effective stiffness.

A liquid, which has a larger sound velocity than glycerine (and, as a matter of fact, the highest known sound velocity of any liquid), has been studied recently: Sorbitol, a hexahydric alcohol, has a sound velocity of the order of  $2.1 \times 10^5$  cm/s when used in 83% solution [16]; when pure, the sound velocity is apparently of the order of  $3 \times 10^5$  cm/s. These velocities were measured at a frequency of 1 megacycle; owing to a relaxation effect,

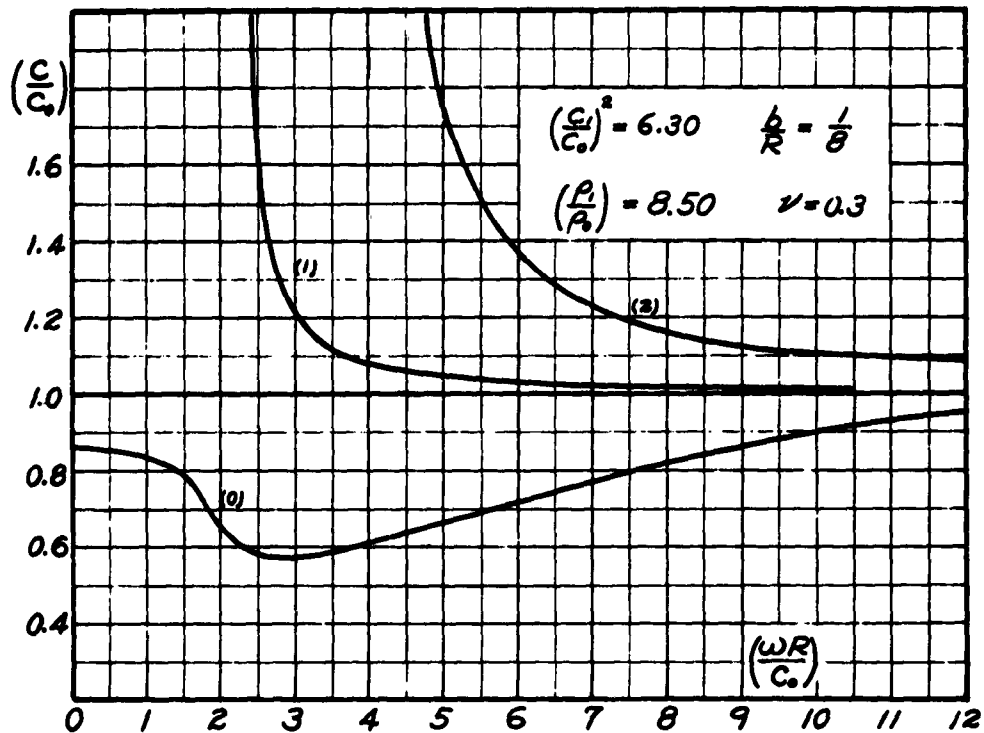


Fig. IV.3. Dispersion curves for the first three modes of propagation of sound waves in a column of water contained in a brass tube, as given by Thompson (12).  $c_0$ ,  $R$ ,  $c$ , and  $b$  respectively translate into the present notation as  $c_s$ ,  $a$ ,  $c_1$  (or  $c_g$ ), and  $2h$ . The tube is stiffness-controlled at all frequencies.

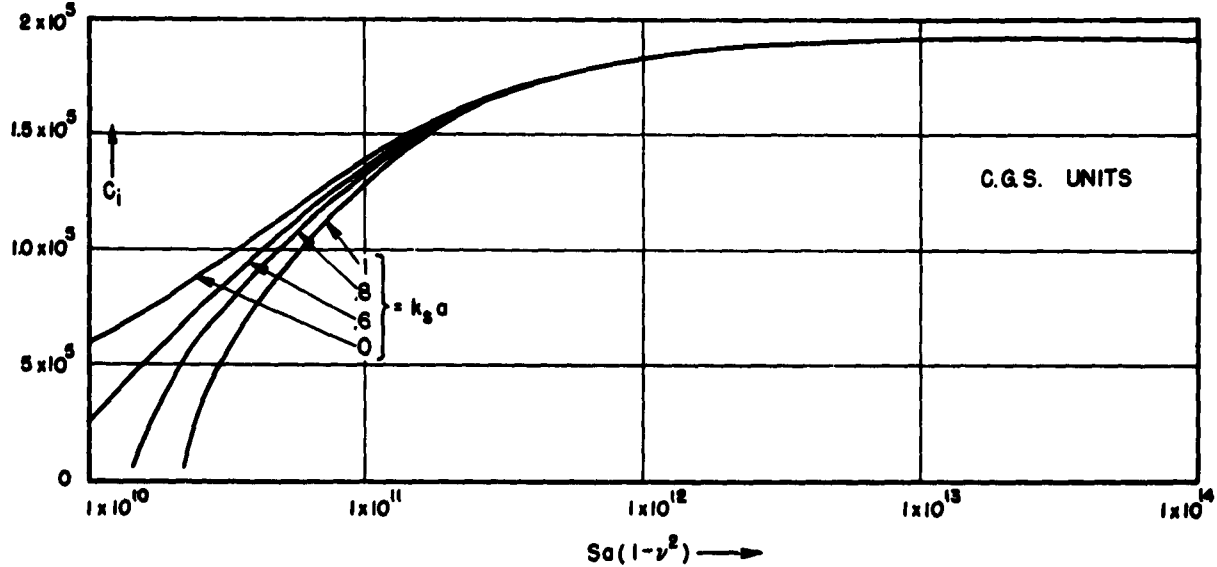


Fig. IV.4. Functional relation between the phase velocity  $c_1$  and the tube wall stiffness  $S$  for glycerine and the zero-order mode of propagation.

they would be somewhat smaller in the low-frequency region. The use of such a liquid would appreciably lower the wall stiffness required to achieve the condition  $c_i = 1.5 \times 10^5$  cm/s; unfortunately, sorbitol is also very viscous.

The relation between the rate of sound radiation and the wall stiffness will now be derived. It will then be possible to estimate the rate of sound radiation which can be achieved for a given liquid. This rate is determined essentially by the attenuation  $\mu$ . In order to relate  $\mu$  to the parameters of the system, let us consider the axial energy flow through a given cross section of the fluid-filled hose, identified by its point of intersection  $z$  with the cylindrical axis. The total energy flowing through the cross section is the sum of the fluid energy  $W(z)$  and of the potential energy of the deformed hose wall  $V(z)$ . In the approximate analysis the kinetic energy of the hose wall may be neglected at low frequencies. The strain energy of a short length of symmetrically deformed hose or shell is approximately:

$$dV(z) = \frac{2\pi Eu^2(z)dz}{(1-\nu^2)a} \quad (\text{IV.6})$$

This expression disregards flexural effects, shearing effects, etc. For a more exact expression, one may consult one of the many analyses of cylindrical shells. The stiffness  $S$  of the hose wall, defined as  $p/u$ , can be derived from this expression in the usual way: From Castigliano's theorem the force ( $=pdA$ ) connected with the strain energy in Eq. (IV.6) is equal to  $\frac{\partial V}{\partial u}$ ; hence

$$px(2\pi adz) = \frac{4\pi Ehudz}{(1-\nu^2)a} \quad (\text{IV.7})$$

Solving for  $p/u (=S)$ , one obtains

$$S = \frac{2Eh}{(1-\nu^2)a} \quad (\text{IV.8})$$

Substituting this parameter in Eq. (IV.6), and using the boundary condition Eq. (II.1), the average rate of strain energy flow through the tube cross section at  $z$  is found to be

$$\dot{V}(z) = \frac{\pi}{2} Sac_i U_i^2 (\exp)^{2\mu z/\lambda_i} \quad (\text{IV.9})$$

The rate of fluid energy flow is (see, for example, reference 7, p. 274)

$$\dot{W}(z) = \frac{\pi a^2}{2\rho_i c_i} |p(z)|^2 \quad (\text{IV.10})$$

This expression is only approximate, since the pressure is also a function of the radius, except in the limiting case where the hose wall is infinitely rigid. The radial velocity  $u$  of the hose wall is, of course, equal to  $p/z_w$  where  $z_w$  is the specific acoustic impedance presented by the hose wall (and the surrounding medium) to radial motion. At very low frequencies, and as a rough approximation, it can be assumed that  $(j\omega z_w \approx S)$  (A more exact expression for  $z_w$  is given in reference 14). The pressure  $p(z)$  in Eq. (IV.10) can now be written as  $-jS\bar{u}(z)/\omega$ . Again making use of the boundary condition Eq. (II.1), the rate of fluid energy flow is finally expressed as follows:

$$\dot{W}(z) = \frac{\pi a^2}{2\rho_i c_i} S^2 U^2 \exp(-2\mu \frac{z}{\lambda_i}) \quad (\text{IV.11})$$

The total rate of flow through the cylindrical cross section located at  $z$  is obtained by adding Eqs. (IV.9) and (IV.11). The total power  $\dot{E}_s$  emitted by the source is the difference of the rates of energy flow through the cross section at  $z = 0$  and the one at  $z = L$ :

$$\dot{E}_s = \frac{\pi a}{2} S U^2 c_i \left(1 + \frac{Sa}{2\rho_i c_i}\right) (1 - e^{-2n\mu}) \quad (\text{IV.12})$$

This function is plotted in Figs. IV.5 (a) and (b) for different values of wall stiffness and for two different values of  $k_o a$ .

The power  $\dot{E}_s$  lost by the source must be equal to the power radiated,  $E_r$ . Since the analysis in Chapter II yields information on the distant field only,  $E_r$  must be obtained by integrating the sound intensity over a large sphere enclosing the sound source. The wave fronts may be considered approximately plane over a small surface element of such a sphere. The sound intensity at the surface element located near the point  $(R, \theta)$  is therefore of the form  $|p(R, \theta)|^2 / 2\rho_o c_o$ . The power radiated is obtained by integrating the intensity over the spherical surface:

$$\dot{E}_r = \frac{1}{2 \rho_0 c_0} \int_{\sigma}^{\pi} |p(R, \theta)|^2 d\sigma$$

$$= \frac{\pi R^2}{\rho_0 c_0} \int_0^{\pi} |p(R, \theta)|^2 \sin \theta d\theta$$
(IV.13)

The quantity  $|p|^2$  is proportional to  $U^2/R^2$ . The above expression is therefore independent of  $R^2$  and proportional to  $U^2$ . The integral (IV.13) has been evaluated numerically for various values of  $\mu$ ; the corresponding values of radiated power  $\dot{E}_r$  are plotted in Figs. IV.5.

Before proceeding further in determining the relation between  $S$  and  $\mu$ , an attempt will be described to calculate  $\dot{E}_r$  by an approximate method; if found satisfactory, such a method would make the cumbersome numerical integrations implied in Eq. (IV.13) unnecessary. The approach tried consists in calculating the power  $\dot{E}_r$  by assuming that the acoustic resistance ratio is approximately the same for the case under consideration and for an infinite cylinder whose dynamic configuration is in the form of unattenuated standing or travelling waves whose wavelength is equal to  $\lambda_i$ , and which extends to infinity over the entire cylinder. The near field, and, in particular, the field at ( $r=a$ ) can, of course, be evaluated for this system. The travelling- and standing-wave cases are found to be equivalent if the proper transformations are made. Using this approach, the average power radiated by an element  $dz$  of the source is

$$d\dot{E}_r = 2\pi a dz \cdot \frac{\rho_0 c_0}{4} \theta_{01}(k_1 a) |\dot{u}(z)|^2$$
(IV.14)

In this expression,  $\theta_{01}$  is an acoustic resistance ratio defined as [1]

$$\theta_{01}(k_1 a) = \frac{2k_0}{\pi k_1^2 a |H_1^{(2)}(k_1 a)|^2}$$
(IV.15)

where

$$k_1 = k_0 \left[ 1 - \left( \frac{c_0}{c_i} \right)^2 \right]^{1/2}$$

Substituting Eq. (II.1) in Eq. (IV.14), and integrating the latter over the length of the source, an expression for the total radiated power is obtained:

$$\dot{E}_r = \frac{\pi^2}{2\mu} a \rho_0 c_0 c_i U^2 \omega \theta_{01}(k_0 a) (1 - e^{-2n\mu}) \quad (\text{IV.16})$$

Equation (IV.16) is also plotted in Fig. IV.5(a). Its magnitude is seen to be approximately twice that of the more exact value obtained from Eq. (IV.13). This discrepancy is due to end-effects in the finite-length source, and to the peculiar behavior of the function  $\theta_{01}$  in the region  $c_i \approx c_0$ . In the case of the infinite cylinder, as  $k_1$  tends to zero along the real axis (i.e., as  $c_i$  tends to  $c_0$  from above), the function  $\theta_{01}$  rises steeply to a maximum value. When  $k_1$  becomes imaginary (i.e., when  $c_i < c_0$ ), the function  $\theta_{01}$  vanishes; in other words, a cut-off phenomenon takes place (for the infinite cylinder uniformly excited only, of course). Hence, while the use of  $\theta_{01}$  is satisfactory when  $c_i > c_0$ , it leads to mediocre accuracy when  $c_i \approx c_0$ , and is entirely unusable when  $c_i < c_0$ .

This approach toward the evaluation of  $\dot{E}_r$  will therefore be discarded in favor of another procedure, which makes use of the acoustic resistance ratio  $\theta_0(k_0 a)$  of an infinitely long, uniformly vibrating cylinder (i.e., a cylinder having a configuration independent of  $z$ ). To simulate the effect of the sinusoidal  $z$ -dependence of boundary condition Eq. (II.1), the amplitude of vibration must be taken equal not to  $|u(z)|$  but to the root-mean-square of that quantity, i.e., to

$$\frac{Ue^{-\mu \frac{z}{k_1}}}{\sqrt{2}}$$

The expression for radiated power then takes the form

$$\dot{E}_r = \frac{\pi^2}{2\mu} a \rho_0 c_0 c_i U^2 \theta_0(k_0 \theta) (1 - e^{-2n\mu}), \quad (\text{IV.17})$$

where [17]

$$\theta_0(k_0 a) = \frac{2}{\pi k_0 a |H_1^{(2)}(k_0 a)|^2} \quad (\text{IV.18})$$

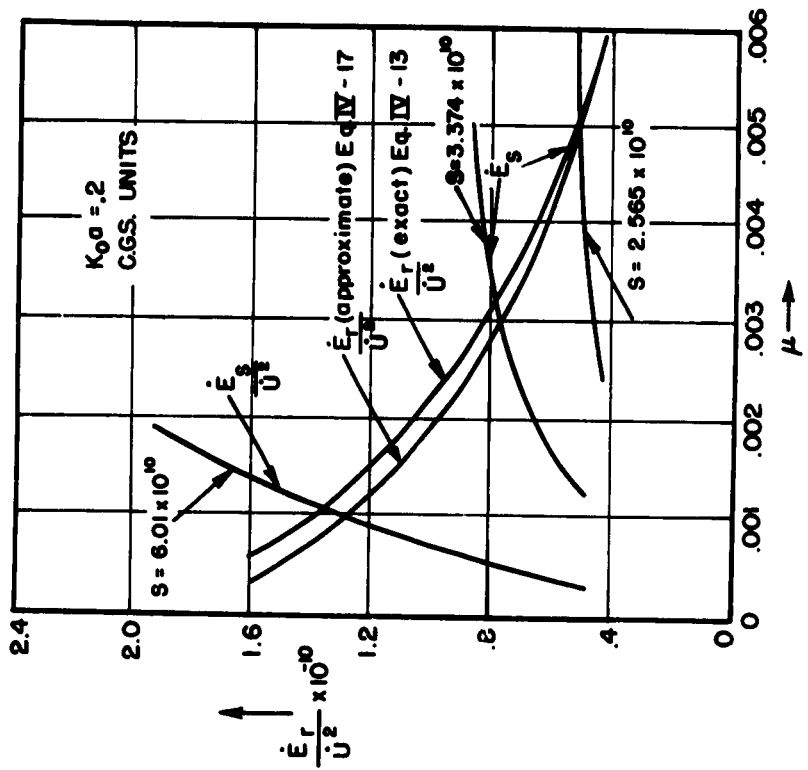


Fig. IV.5 (b). Power radiated by the source ( $\dot{E}_s$ ) for different wall stiffnesses, and sound power in far field ( $\dot{E}_r$ ), for  $k_{Cs} = 0.2$ .

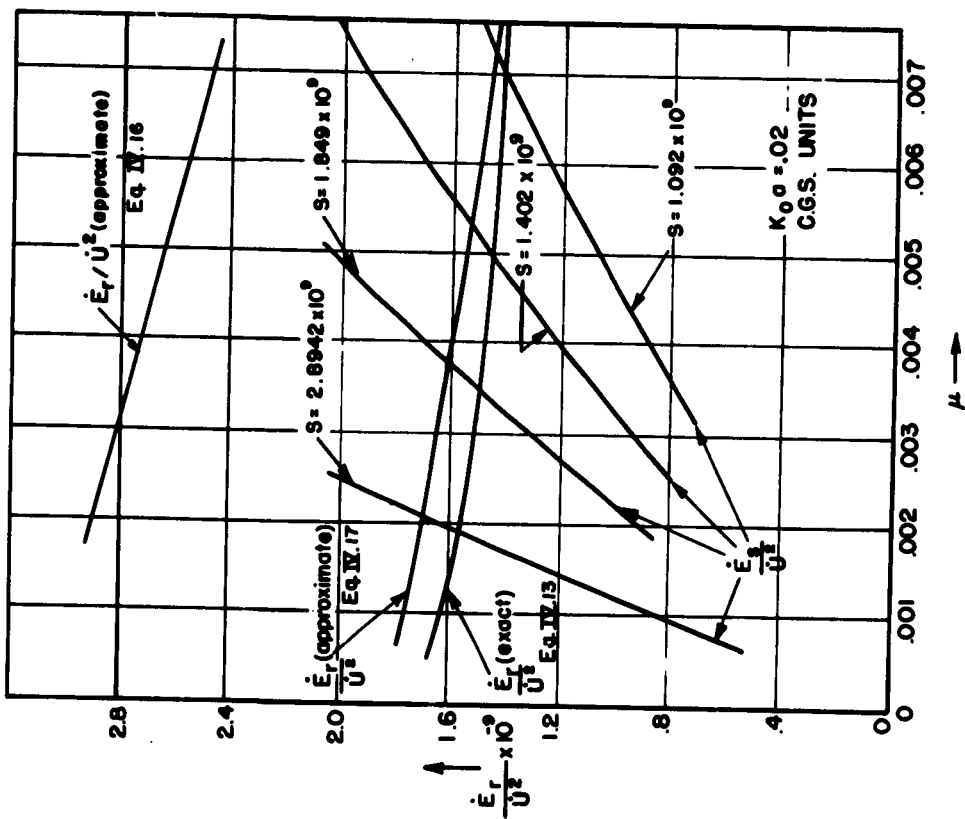


Fig. IV.5 (a). Power radiated by the source ( $\dot{E}_s$ ) for different wall stiffnesses, and sound power in far field ( $\dot{E}_r$ ), for  $k_0^0 = 0.02$ . Intersections of curves give possible combinations of  $\mu$  and  $S$ , and thus determine the functional relation  $\mu = f(S)$ .

The value of  $\dot{E}_r$  thus computed is also plotted in Fig. IV.5. For the parameters selected this approximate value of  $\dot{E}_r$  is seen to be only slightly larger than the more exact value obtained from Eq. (IV.13). For other conditions, particularly for a shorter hose, a greater discrepancy may be expected. However, this approximate method appears adequate for the present purpose, particularly since the end-fire source must measure at least 15 to 30 wavelengths in length.

It is noted that both the approximate and exact values of  $\dot{E}_r$  decrease with increasing  $\mu$ . At first glance, one might expect the opposite. This impression would be correct if the power furnished to the source were constant. This, however, is not the case; it is the velocity amplitude  $U$  at the driving end of the source which is kept constant. Equations (IV.13) and (IV.17) state nothing as to the power supplied to the source, and do not contain any information as to the impedance presented by the cylindrical source to the driving unit.

The functional relation  $\mu = f(S)$  can now be determined from the following line of reasoning: Since, in the absence of friction, the power  $\dot{E}_s$  emitted by the source must be equal to the power  $\dot{E}_r$  radiated, physically possible situations correspond to intersections of the curves representing  $\dot{E}_s$ , Eq. (IV.12) and of the curves representing  $\dot{E}_r$ , Eq. (IV.13) or (IV.17). The values of  $\mu$  and  $S$  corresponding to these intersections are plotted in Figs. IV.6.

An explicit expression for the functional relationship between  $\mu$  and  $S$  can be derived if the approximate expression for  $\dot{E}_s$  is used. Equalizing Eqs. (IV.12) and (IV.17), and solving for  $\mu$ , one obtains

$$\mu = \frac{\pi \rho_0 c_0 \omega_0 \theta_0 (k_0 a)}{S \left( 1 + \frac{Sa}{\rho_i c_i} \right)} . \quad (IV.19)$$

Since the quantity  $c_i$  is itself a function of the wall stiffness  $S$ , this expression becomes explicit only after introducing the relation between  $c_i$  and  $S$  which is expressed in Eq. (IV.5). Neglecting the inertial term in this expression and taking  $c_i = 1.5 \times 10^5$  cm/s, the required  $S$  can be expressed as a function of the characteristic velocity of sound  $c_s$ :

$$S = \frac{2\rho_i c_s^2}{a(1-\nu^2) \left( \frac{c_s^2}{2.25 \cdot 10^{10}} - 1 \right)}, \text{ C.G.S.} \quad (\text{IV.19a})$$

When this expression is introduced in Eq. (IV.19), and taking  $\rho_o c_o = 1.535 \times 10^5$  C.G.S., an explicit relation between  $\mu$  and  $c_s$  is obtained

$$\mu = 1.07 \times 10^{-5} \frac{\omega \theta_o (k_o a) a (1-\nu^2) (c_s^2 - 2.25 \times 10^{10})}{\rho_i c_s^2 [1 + \frac{2 c_s^2}{(1-\nu^2)(c_s^2 - 2.25 \cdot 10^{10})}]}, \text{ C.G.S.} \quad (\text{IV.20})$$

For small values of  $k_o a$  ( $< 0.2$ ) this can be simplified further by using the asymptotic expression for  $\theta_o (k_o a)$  for small argument; i.e.,  $\theta_o = \pi k_o a / 2$ .

The expression for the attenuation now becomes:

$$\mu = - \frac{1.12 \times 10^{-10} \omega^2 a^2 (1-\nu^2) (c_s^2 - 2.25 \times 10^{10})}{\rho_i c_s^2 [1 + \frac{2 c_s^2}{(1-\nu^2)(c_s^2 - 2.25 \times 10^{10})}]} \text{ for small } k_o a, \text{ C.G.S.} \quad (\text{IV.21})$$

The useful frequency range of this design can now be determined. The value of  $\mu$  increases with frequency. Hence, since increasing the value of  $c_s$  is seen, by Eq. (IV.20), to correspond to an increase in  $\mu$ , liquids having the largest values of  $c_s$  are those whose frequency range can be extended to the lowest values (while still maintaining a sufficiently large value of  $\mu$ ). What these lower limits of operating frequencies are can be determined from Eq. (IV.19) by noting from Figs. II.7 that  $n\mu$  must be of the order of two, if full advantage is to be taken of a large source length (viz., 30 wavelengths). In order to compensate for the small values of  $\mu$  resulting from the large values of wall stiffness  $S$  which must be used (particularly near the lower limit of the operating frequency range; cf., Eq. (IV.20)), it is desirable to use the longest possible source. If the greatest practical length is 500m, the total attenuation in decibels ( $= 8.686 n\mu$ ) can be calculated as a function of frequency:

$$T.A. = 0.461 n\mu, \text{ in db} \quad (\text{IV.22})$$

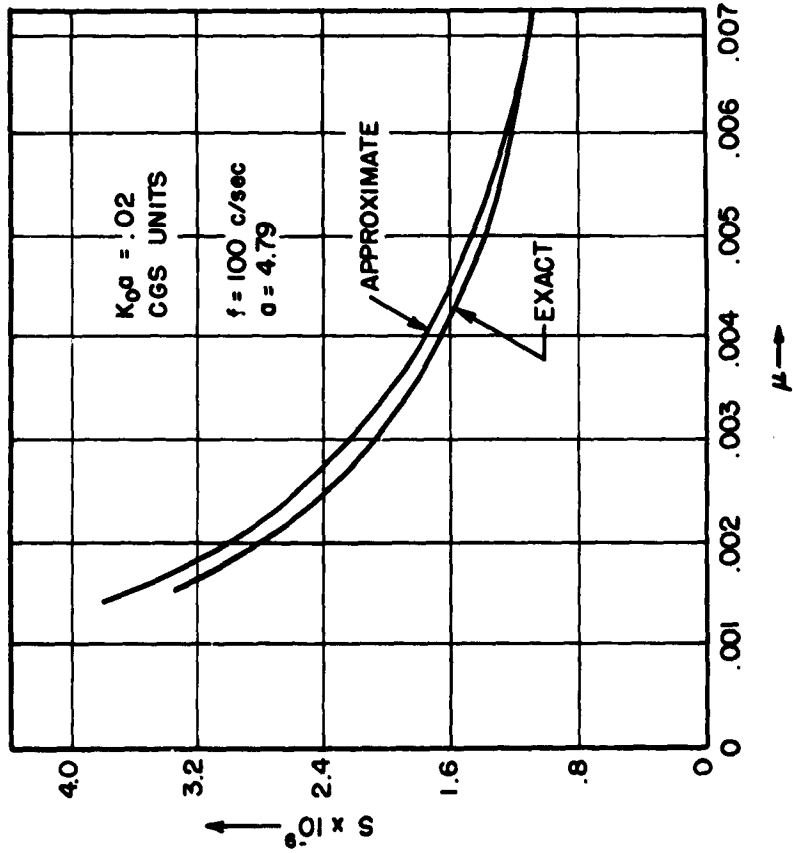
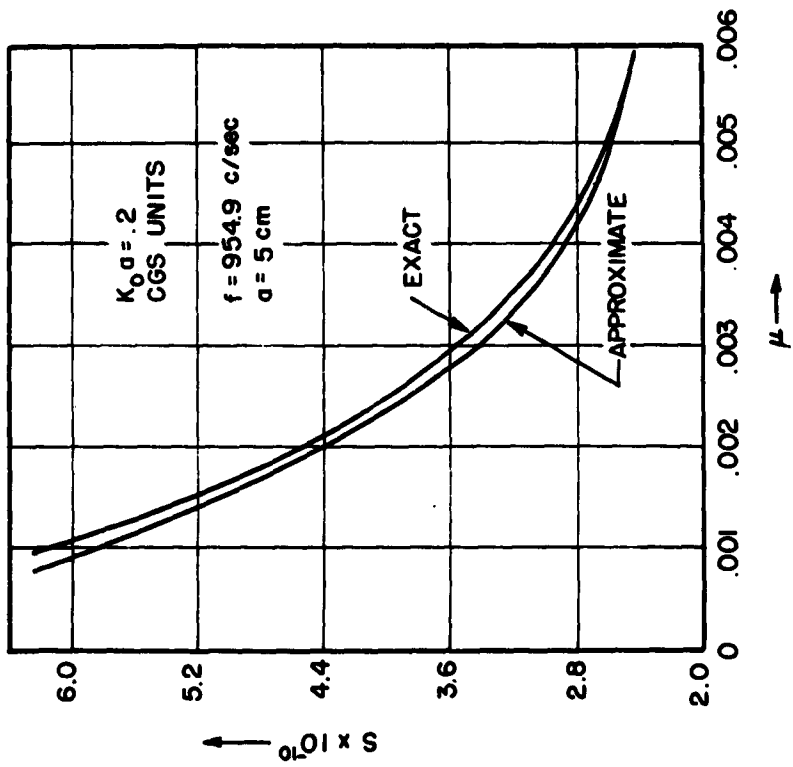


**Fig. IV.6 (a).** Functional relation  
 between tube wall stiffness  $S$  and attenua-  
 tion  $\mu$  for  $k_0 a = 0.02$ , computed from Fig.  
 IV.5 (a).

**Fig. IV.6 (b).** Functional relation  
 between  $S$  and  $\mu$ , for  $k_0 a = 0.2$ , computed  
 from Fig. IV.5 (b).

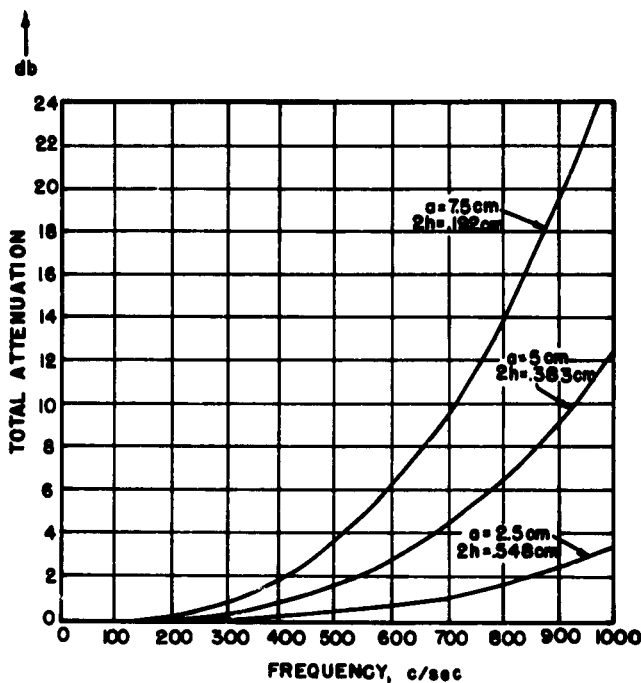


Fig. IV.7. The total attenuation ( $= 8.686 n\mu$ ) of the sound waves reaching the far end of the cylindrical source, as a function of frequency, for glycerine ( $\rho_1 = 1.26$ ,  $c_s = 1.92 \times 10^5$ , C.G.S.). Since the product ( $n\mu$ ) (i.e. the total attenuation) must exceed a certain minimum value if end-fire directivity is to be achieved, these curves give the minimum operating frequency of a hose having a given radius.

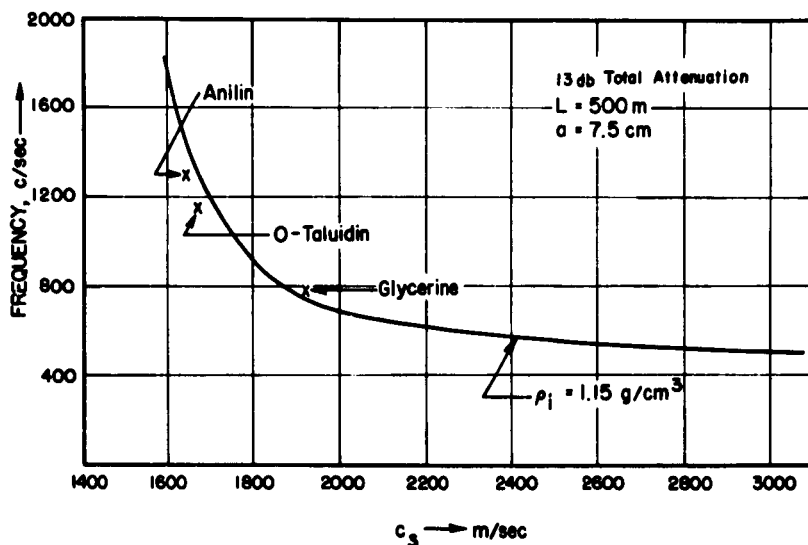


Fig. IV.8. Frequencies giving a total attenuation of 13 db as a function of the sound velocity  $c_s$  of the liquid used in the fluid column. A hypothetical liquid having a density of  $1.15 \text{ g/cm}^3$  is assumed. Points corresponding to existing liquids are also indicated. A Sorbitol solution would give a limiting frequency value of the order of 600 c/s.

Substituting for  $\mu$ , from expression (IV.20) the total attenuation can be written explicitly as a function of frequency, and of the parameters of the hose and of the liquid it contains:

$$T.A. = 0.494 \cdot 10^{-5} \frac{\omega_0^2 (k_s) s (1-v^2) (c_s^2 - 2.25 \times 10^{10})}{\rho_i c_s^2 [1 + \frac{2c_s^2}{(1-v^2)(c_s^2 - 2.25 \times 10^{10})}]} , \text{ in db, and using C.G.S. units}$$
(IV.22a)

This is plotted in Fig. IV.7 for a hose filled with glycerine ( $\rho_i = 1.26$ ,  $c_s = 1.92 \times 10^5$  C.G.S.); the Poisson's ratio of the hose wall material is taken to be 0.3). The directivity index corresponding to these values of  $n\mu$  can, of course, also be plotted as a function of frequency. If, in a particular design, it is decided that the directivity index corresponding to a certain value of  $n\mu$ , say  $n\mu = 1.50$  (which corresponds to a total attenuation of 13 db), is acceptable, Equation (IV.22a) can be solved for the limiting frequency in terms of  $c_s$ . The lowest operating frequency for different liquids can thus be plotted as a function of  $c_s$  (cf. Fig. IV.8). The point corresponding to a sorbitol solution would give a limiting frequency of the order of 600 c/s.

For a given liquid the value of wall stiffness required to achieve the condition  $c_i = 1.5 \times 10^5$  cm/s (which is given in Eq. (IV.19a), can be used to compute the pressure  $P$  and radial displacement  $U$  of the hose wall at the driving end of the source. This is illustrated in Fig. IV.9 for a total output of 1 kw at 1000 c/s for a hose filled with glycerine.

In summary, it appears doubtful whether a practical design based on a stiffness-controlled hose can be used efficiently below 1000 c/s. However, one favorable aspect of the situation is that the small values of  $\mu$  imposed by the limitations of this design permit the achievement of very high end-fire directivity (cf. Chap. II).

This design was studied very thoroughly in the Internal Reports of 16 February, 8 April, and 28 April, 1953. The latter report contains an analysis of the effect of frictional losses in the hose wall and in the liquid.

### The Mass-controlled Hose

Another approach, avoiding one of the worst drawbacks of the stiffness-controlled hose (which is that sea-water cannot be used to fill the hose), is to drive the source above the natural frequency of the axially symmetrical (ring-type) mode of vibration of the hose. For our purpose, this natural frequency should of course be as small as possible; the hose should therefore offer as little resistance to bending as possible, so that it will not tend to remain stiffness-controlled, in the fashion of a tube (cf., preceding section and reference 11). In the ideal case, when the hose experiences only membrane stresses, the specific wall reactance is of the form:

$$x_w = - \frac{2\rho_w c_w}{k_w a} \frac{1}{\frac{a}{h} - \frac{1-2\nu}{1-\nu}} \left[ -k_w^2 a^2 + 1 + \frac{\nu^2}{\left(\frac{c_i}{c_w}\right)^2 - 1} \right] \quad (\text{IV.23})$$

Neglecting the Poisson term, which is small, it is seen that  $x_w$  is positive, i.e., that the hose is mass-controlled, when  $k_w a > 1$ , i.e., at frequencies above the natural frequency of the axially symmetrical mode of vibration. Disregarding the effect of the surrounding medium (which is beneficial for this purpose in that it increases the value of  $x_w$ ), the lower limit of the frequency range of such a source is therefore found to be  $k_w a = 1$ . In order to extend this limit as far as possible, it is desirable to use large-diameter hoses made of a material having a small value of  $c_w$ , i.e., plastic, rubber, or the like.

The dispersion curve connected with the zero mode when  $x_w > 0$  is shown in Fig. IV.10. The larger the value of  $x_w$  (i.e., the more mass-controlled the hose wall), the smaller the cut-off frequency and the lower the limit of the region over which the phase velocity  $c_z$  (or  $c_i$ ) is essentially equal to the sound velocity  $c_s$  [15]. Since this region is the nondispersive frequency range where the end-fire source would be operated, it is possible to use sea water in the hose so that  $c_z = c_s = c_o$ . The major drawback of the stiffness-controlled hose is thus eliminated.

The cross-sectional distribution of the zero mode conforms fairly

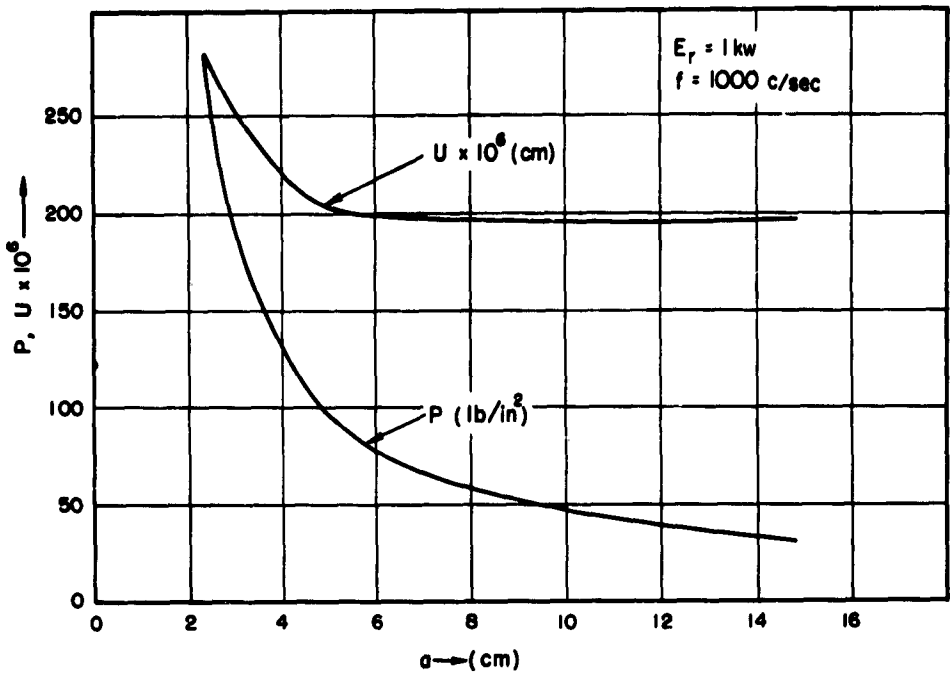


Fig. IV.9. Displacement amplitude  $U$  and pressure amplitude  $P$  at the driving end of a glycerine-filled hose radiating 1 kw of sound power at 1000 c/s, plotted as a function of hose radius. The magnitude of the wall stiffness  $S$  is such as that  $c_1 = 1.5 \times 10^5$ , C.G.S. (cf. Eq. IV.19 (a)).

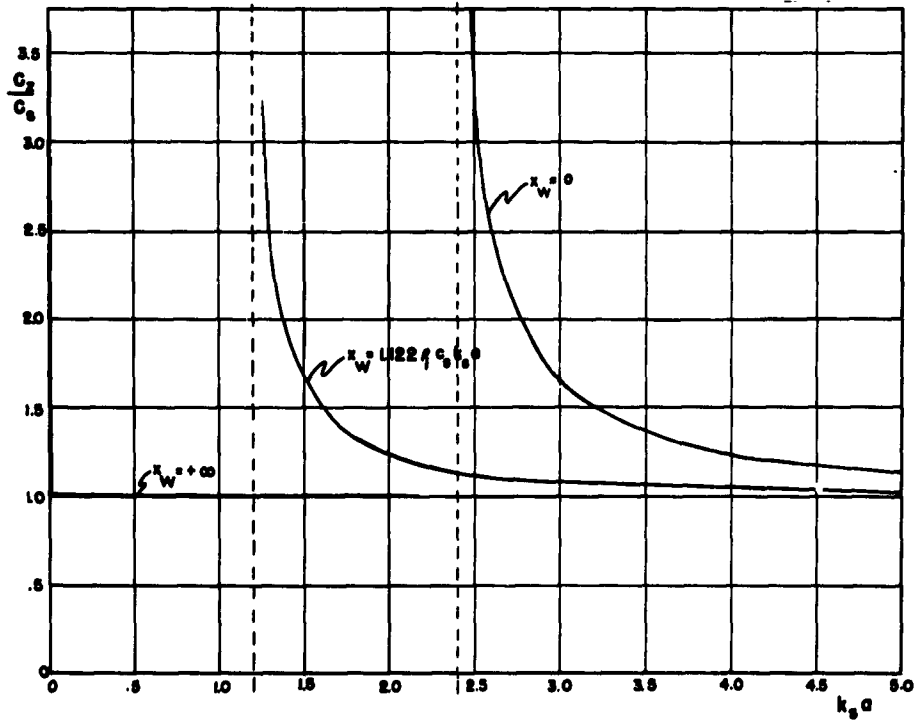


Fig. IV.10. Dispersion curves for sound waves propagating in the zero-order mode inside a fluid-filled, mass-controlled hose. All curves approach the limit  $c_2 = c_s$  for sufficiently large  $k_o a$  (i.e. frequency). The larger  $x_w$ , i.e. the more mass-controlled the hose, the lower the frequency at which  $c_2$  first approaches its asymptotic value  $c_s$ .

well to the dynamic configuration of a piston-type transducer whose surface elements move with equal amplitude and phase. (If the wall approaches a pressure release condition, this is not true.) Since the higher modes all display nodal circles, such a transducer would not excite them appreciably, even above their cut-off frequencies.

In practice, of course,  $x_w$  is a function of frequency. The dispersion curves will therefore never be as illustrated in Fig. IV.10. In order to determine the possible operating range for an actual hose material, these curves were calculated for a soft rubber hose filled with sea-water (cf. Fig. IV.11). The lower frequency limit is approximately 7800 c/s for a 1-ft diameter hose. This frequency, of course, is too large to be acceptable. As seen from Fig. IV.10, it can be brought down to any desired value by increasing the wall reactance  $x_w$ ; indeed, as the mass reactance approaches infinity, the lower frequency limit tends to zero. By using a heavier material for the hose wall,  $x_w$  can be increased; the effective weight of the wall can also be increased by attaching segments of metal rings to its surface. In practice, however, this may not be necessary: The actual limiting frequency will be considerably lower and the wall reactance  $x_w$  much larger, owing to the mass loading provided by the surrounding sea water. In theory, the mass loading for the axially symmetrical mode of vibration approaches infinity for an infinite cylinder [1], as  $c_i$  tends to  $c_o$ . This, of course, does not hold for a finite cylinder. However, in a cylinder 15 to 30 wavelengths long, the mass loading is still very large, i.e.,  $x_w$  is much increased and, hence, the lower operating frequency limit extended considerably beyond the value calculated by neglecting the action of the surrounding medium. Unfortunately, the theory developed in Chapter II does not give information on the near field. It is therefore impossible to predict how far the lower frequency limit could be extended. A qualitative idea of how short a cylinder can be and still experience considerable mass loading from surrounding medium can be obtained by the following reasoning: This phenomenon of infinite mass loading coincides with a vanishing of the resistive impedance when  $c_i < c_o$ . Both phenomena also occur in the case of infinite rectangular surfaces. Goesele, who has studied this problem [18], shows that even when the surface is only 3

wavelengths long the energy radiated drops by approximately 10 db when  $\lambda_i/\lambda_o$  is decreased from unity to about 0.95. It is to be expected that the reactive impedance similarly approaches its limiting value for the infinite case when the radiating surface is still relatively small. Presumably, the same holds true for cylindrical surfaces, as the two cases are mathematically quite similar.

In developing a mass-controlled hose design, a practical procedure would be to set the lower frequency limit equal to the natural frequency of the hose in air, and to rely on the fluid reactance to provide the necessary mass loading to push the dispersion curve down a good part of the way from the ( $x_w = 0$ ) curve towards the ( $x_w = \infty$ ) curve in Fig. IV.10. The lower frequency limit determined by this criterion is shown in Fig. IV.12 for three different materials; however, the natural frequency is not the only criterion by which to judge a potential hose material. If the material is not sufficiently strong, the hose wall will have to be excessively thick to support the desired pressure differential of 10 atmospheres which it is desired to maintain in order to retard the onset of cavitation. A thick hose wall is of course undesirable because of the increased frictional losses, manufacturing cost, etc. The greater thickness also results in increased flexural stresses, thus raising the natural frequency and invalidating the curves in Fig. IV.12 which are based on the assumption of a purely membrane-type state of stress (cf. Eq. (IV.23)). In view of these considerations, the three materials in Fig. IV.12 have been compared as to their strength; a convenient way of doing this is to plot the inner pressures causing a "hoop stress" equal to the respective yield and tensile strengths as a function of the wall-thickness-to-radius ratio (=  $2h/a$ ) (cf. Fig. IV.13). Materials such as soft rubber, which display a desirably low natural frequency in Fig. IV.12, are revealed in Fig. IV.13 to be entirely unsuitable, as they do

- - - - -

\* The properties of plastics and rubber vary, of course, considerably with testing conditions, manufacturing process, etc. For soft rubber, the physical properties from which  $c_w$  is calculated, and the yield strength, were determined experimentally on the apparatus which is illustrated in Fig. IV.15 and described below. The material labeled "polyethylene" was not identified more specifically in the reference giving its physical properties. The properties of "Mylar" were obtained from the manufacturers.

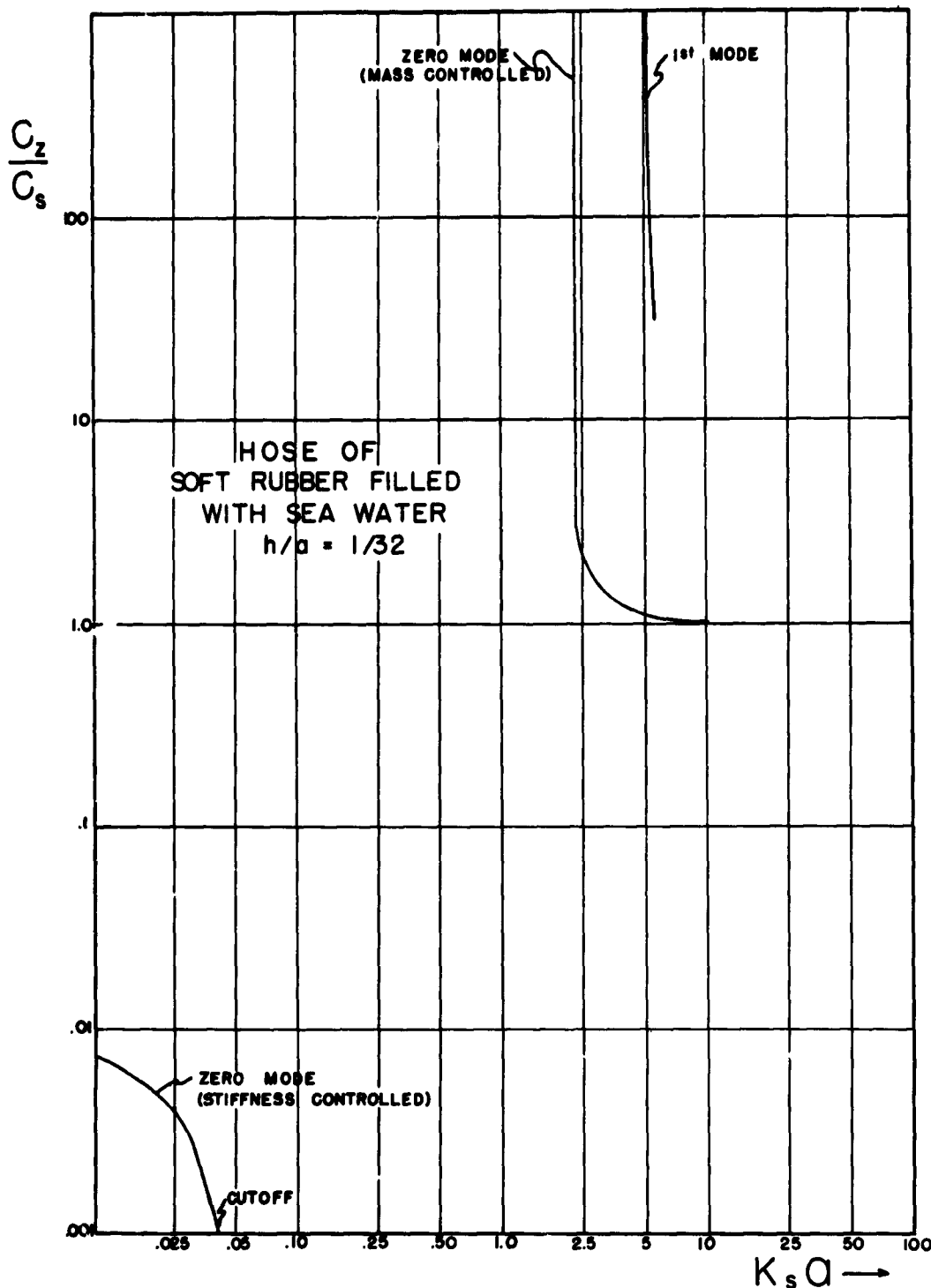


Fig. IV.11. Dispersion curves for a soft rubber hose filled with seawater. The value of  $k_s a$  (i.e. of frequency) at which the zero-mode approaches the desired condition  $c_z \approx c_s$  is unacceptably large. The actual frequency will be much smaller owing to the mass-loading of the surrounding water, which was neglected in computing these curves, and which effectively increases  $x_w$ .

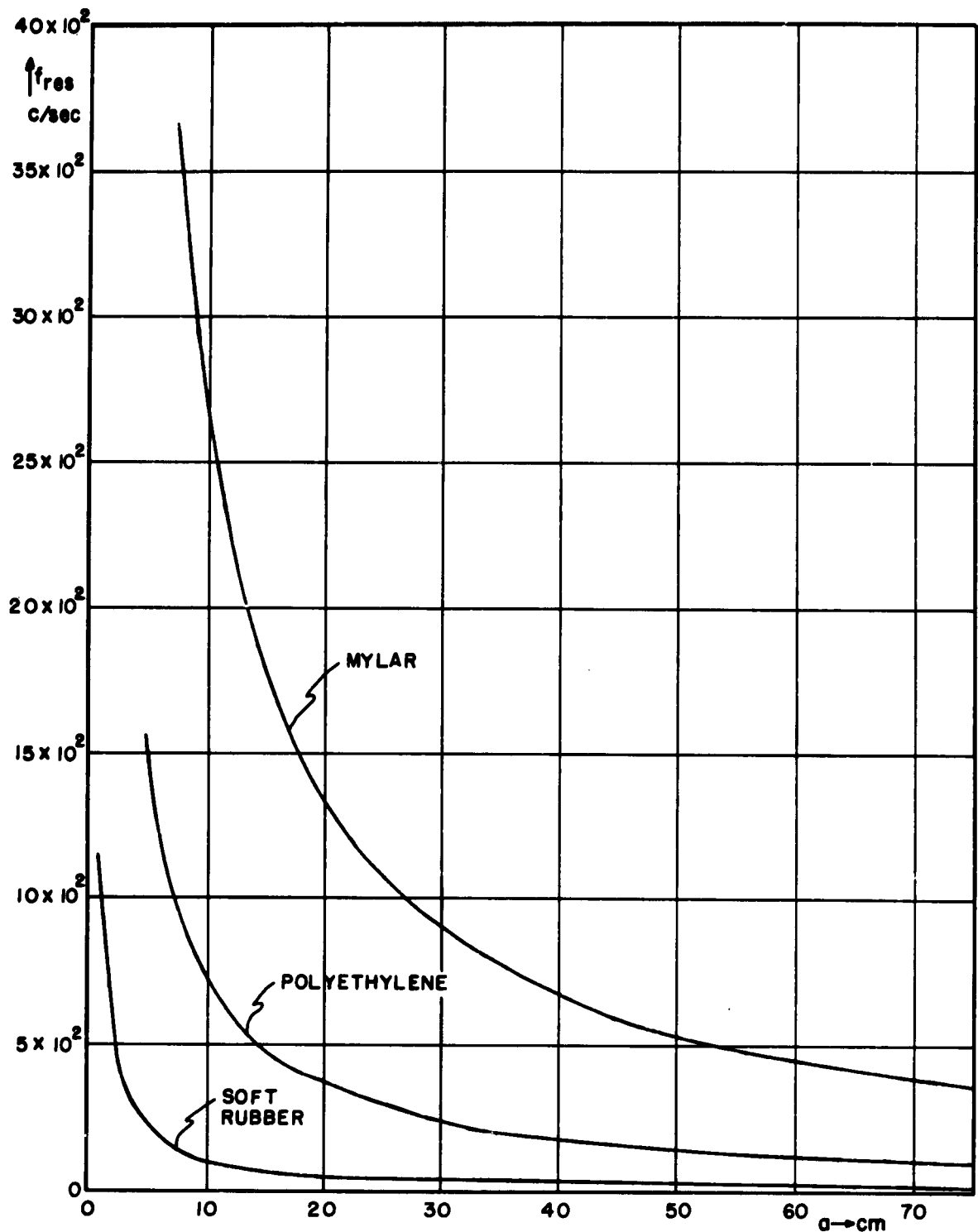


Fig. IV.12. Natural frequencies of hoses of soft rubber and of two types of plastic vibrating in their axially symmetrical mode, as a function of hose radius. When the hoses are submerged, they will be heavily mass-controlled at these frequencies owing to the mass-loading of the ambient water. The longitudinal wave velocity  $c$ , which determines the natural frequencies is as follows for the three hose materials:  $0.068 \times 10^5$  for soft rubber,  $0.458 \times 10^5$  for Polyethylene, and  $1.674 \times 10^5$  for Mylar, in cm/s.

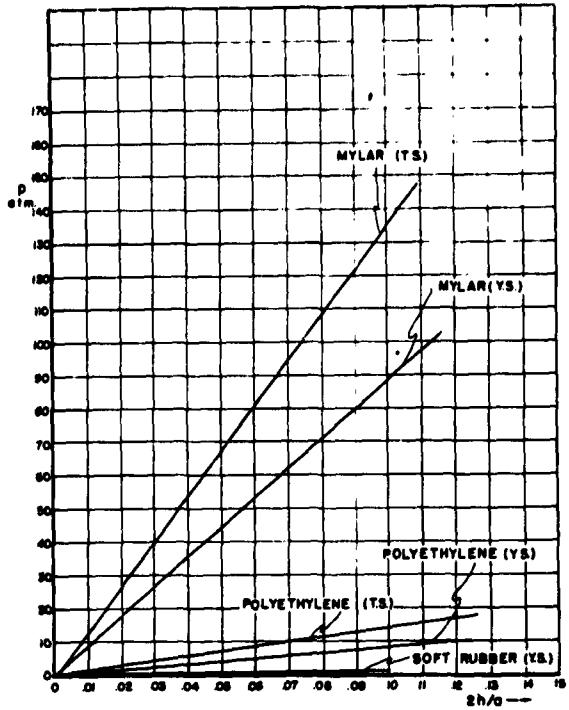


Fig. IV.13. Relative strengths of three hose materials. The pressure differential across the hose wall giving a hoop-strength equal to the yield and tensile strengths is plotted as a function of the wall thickness to radius ratio for soft rubber ( $Y.S. = 1,54.6 \text{ lb/in}^2$ ), polyethylene ( $Y.S. = 1,200 \text{ lb/in}^2$ ,  $T.S. = 2,100 \text{ lb/in}^2$ ), and Mylar ( $Y.S. = 13,000 \text{ lb/in}^2$ ,  $T.S. = 20,000 \text{ lb/in}^2$ ).

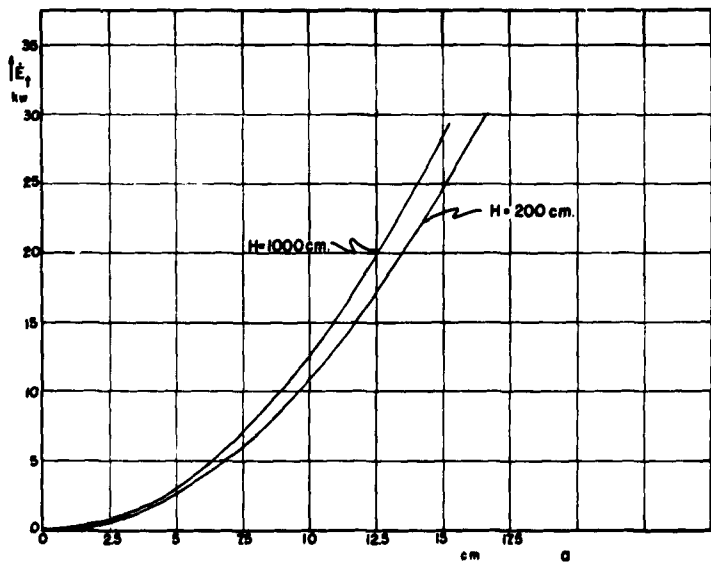


Fig. IV.14. Power which can be injected into the hose by a piston-shaped transducer without causing cavitation on the transducer surface, as a function of hose radius. The pressure differential across the hose wall is 10 atmospheres. The exterior hydrostatic pressure corresponds to depths of immersion of 200 and 1000 cm.

not support the pressure differential necessary to avoid cavitation at the transducer surface. The designer must therefore make a compromise and select a material combining a reasonably small  $c_w$  with sufficiently large strength. This suggests a material such as "Mylar" (polyethylene terephthalate) strong enough to permit the use of a very thin hose wall (of the order of  $2h = 0.01$ ) even for a pressure differential of 10 atmospheres. Such a hose, with its low frictional losses, its small banding resistance, and its resistance to mechanical wear, etc., would have very desirable all-around characteristics. Only experiments will show how far down the lower frequency limit can be pushed by means of the mass loading of the surrounding sea water.

If the initial tests show that the mass-loading of the surrounding fluid is not sufficient to bring the frequency limit down to the desired value, the above-mentioned remedy of attaching inertial elements in the form of circular metal segments to the hose wall might be used. In this connection, it is interesting to note that even a metal tube which, as mentioned above, is normally stiffness-controlled at all frequencies can be endowed with a massive wall reactance by machining grooves at regular intervals into the outer wall surface [13]. The thick-walled segments then act as rigid masses and the thin-walled ones as spring elements; the flexural resistance in these elastic elements is not sufficient to maintain the tube wall stiffness-controlled.

The power with which such a source in the form of a fluid-filled hose can be driven without running into cavitation is determined by the fact that the pressure amplitude at the transducer must not exceed the sum of the surrounding hydrostatic pressure and of the 10 atmospheres pressure differential which the hose wall is designed to sustain. Assuming that the transducer surface is relatively plane during motion, the maximum power which can be injected into a hose filled with sea water is

$$\dot{E}_t = \frac{(\rho_i g H + \Delta p)^2}{2 \rho_i c_i} \pi a^2$$

$$= 1.012 \times 10^{-15} (1010 H + 1.013 \times 10^7)^2 a^2 \quad (\text{IV. 24})$$

where  $H$  is the depth at which the source is located,  $\Delta p$  the pressure differential, and  $g$  the gravitational acceleration;  $H$  and  $a$  are in cm, and  $\dot{E}$  in

kw. The power furnished to the source is plotted in Fig. IV.14 as a function of source diameter for two depths of immersion. It is seen that the amount of power is very large.

Finally, some experimental work in connection with the design of such a hose should be mentioned. Some difficulty may be encountered in computing  $x_w$  as given by Eq. (IV.21) if the hose wall is built of several layers of different materials or simply of nonhomogeneous material such as fabric, since the values of Young's modulus and Poisson's ratio are then not immediately available. For this purpose a testing rig was designed (Fig. IV.15) from which the change in volume of a certain hose length can be determined as a function of pressure. The graduate and hose shown in the figure are filled with water. Air pressure, throttled down to the desired value from the compressed air main is then allowed to act on the interface in the graduate. Expansion of the hose causes the water level to drop; a plot of volume change vs. pressure is thus obtained. The desired elastic constants can be then computed and  $x_w$  determined. This rig can also be used to determine the strength of the hose; for this purpose, the graduate is removed and the pressure applied directly at one end of the water-filled hose.

#### Summary: Comparison of these Designs

The merits of the different designs which have been described can now be compared; all the designs listed satisfy the requirements that the phase velocity be equal to the sound velocity in sea water and independent of frequency within the operating range indicated:

(1) The mass-controlled hose seems to be most practical. Even though it is not possible to compute the value of the lower frequency limit since the present analysis does not give information on the near field, i.e., on mass-loading by the surrounding water, one might expect that the operating range will extend to frequencies of the order of 1000 c/s and possibly of 100 c/s. In practice, there is no upper limit to the frequency range over which this source can be used without significant change in directivity pattern since the phase velocity is independent of frequency above the lower limit of the range of operating frequencies. If necessary, the frequency limit can be lowered further by mass-loading the hose wall by means of metal



Fig. IV.15. Apparatus for measuring the elastic constants and strength of hose wall materials.

ring segments attached to its outer wall surface. The design calls for a strong, thin plastic hose, of a material such as "Mylar," filled with sea water under considerable pressure to avoid cavitation. A pressure differential of 10 atmospheres will permit power of the order of 30 kw to be injected at the driving end without danger of cavitation on the transducer surface;\* such a hose might have a 1 ft. diameter and a wall thickness of 1/8 inch. The source could be driven by a conventional electromechanical transducer. However, in view of the low operating frequencies, it appears tempting to attempt to develop for this purpose a hydraulic transducer making use of some phenomenon of hydrodynamic instability.

(2) For frequencies of the order of one or a few hundred cycles/sec a thin plastic shell propagating longitudinal waves may be satisfactory; a drawback of this approach is that the displacements are mostly axial.

(3) In the same very low-frequency region the end-fire source could be in the form of a thin-walled hose filled with a gelatin-like substance. The hose serves a purely protective purpose. The device differs from the liquid-filled, stiffness-controlled hose in that the gelatin has sufficient cohesive strength so that the action of the hose is not necessary to maintain the phase velocity at the desired value. This device also suffers from the drawback that the displacements are mostly axial.

(4) The stiffness-controlled hose can be used in the frequency range above 2000 (and, possibly, 1000 c/s). In addition to the drawback of a relatively high lower-frequency limit, it possesses the undesirable feature that sea water cannot be used to fill the hose.

(5) In the frequency range above 6000 c/s a thin metal tube undergoing flexural vibrations would perform adequately.

- - - - -  
\* There is, of course, the possibility of cavitation on the outer wall surface near the driving end. If this occurs the segment of the source nearest the driving end does not radiate sound as it is shielded from the surrounding medium by a layer of cavitation bubbles. This essentially amounts to a reduction of the effective length of the source. This situation can be prevented by increasing the wall reactance.

Acknowledgments

The idea of an end-fire directive source was conceived by Professor F. V. Hunt. In addition to suggesting this work, he has contributed to every one of its phases with stimulating suggestions and discussions.

The experimental work was performed thanks to the patient and expert help of Mr. A. A. Janszen.

The lengthy numerical computations were carried out by Mrs. E. B. Bockelman.

## APPENDIX

Analysis of the End-Fire Source Problem  
by Means of the Green's Function

Statement of the Problem:

In Chapter II, the mathematical analysis of this problem was presented in greatly condensed form. Certain aspects of the analysis will be expanded here; in particular, the derivation of the Green's function and the evaluation of the Fourier integrals which express the Green's function and the distant field are discussed in detail. As mentioned in Chapter II, the expression for the distant field was obtained by Laird and Cohen (4) without the use of the Green's function. The manipulation which leads to Eq. (A.12) was presented by Levin and Schwinger (5).

The problem is to determine a velocity potential  $\psi(r, \phi, z)$  (or  $\psi(\bar{R})$ , where  $\bar{R}$  is a space vector) satisfying the wave equation

$$(\nabla^2 + k_0^2) \psi(\bar{R}) = 0 \quad (\text{A.1})$$

and Neumann boundary conditions

$$\left. \frac{\partial \psi(r, \phi, z)}{\partial r} \right|_{r=a} = 0 \quad \text{for } z < 0, z > L$$

$$\left. \frac{\partial \psi(r, \phi, z)}{\partial r} \right|_{r=a} = -\dot{u}(\phi, z) \quad \text{for } 0 < z < L \quad (\text{A.2})$$

The cylindrical surface extends to infinity, but the boundary condition is seen to be homogeneous in the regions  $-\infty < z < 0$  and  $L < z < +\infty$ . The validity of this assumption was discussed in Chapter II.

Derivation of the Green's Function

The Green's function satisfies, by definition, the following conditions

$$\begin{aligned} (\nabla^2 + k_0^2) G(\bar{R}, \bar{R}') &= -\delta(\bar{R} - \bar{R}') \\ G(\bar{R}, \bar{R}') &\rightarrow 0 \text{ as } |\bar{R}| \rightarrow \infty \end{aligned} \quad (\text{A.3})$$

where  $\delta(\bar{R} - \bar{R}')$  is the Dirac delta-function. In addition,  $G$  must be continuous at  $\bar{R} = \bar{R}'$  and its first derivative at that point must have a discontinuity compatible with the unit source condition.

Green's theorem applied to  $\psi$  and  $G$  states that

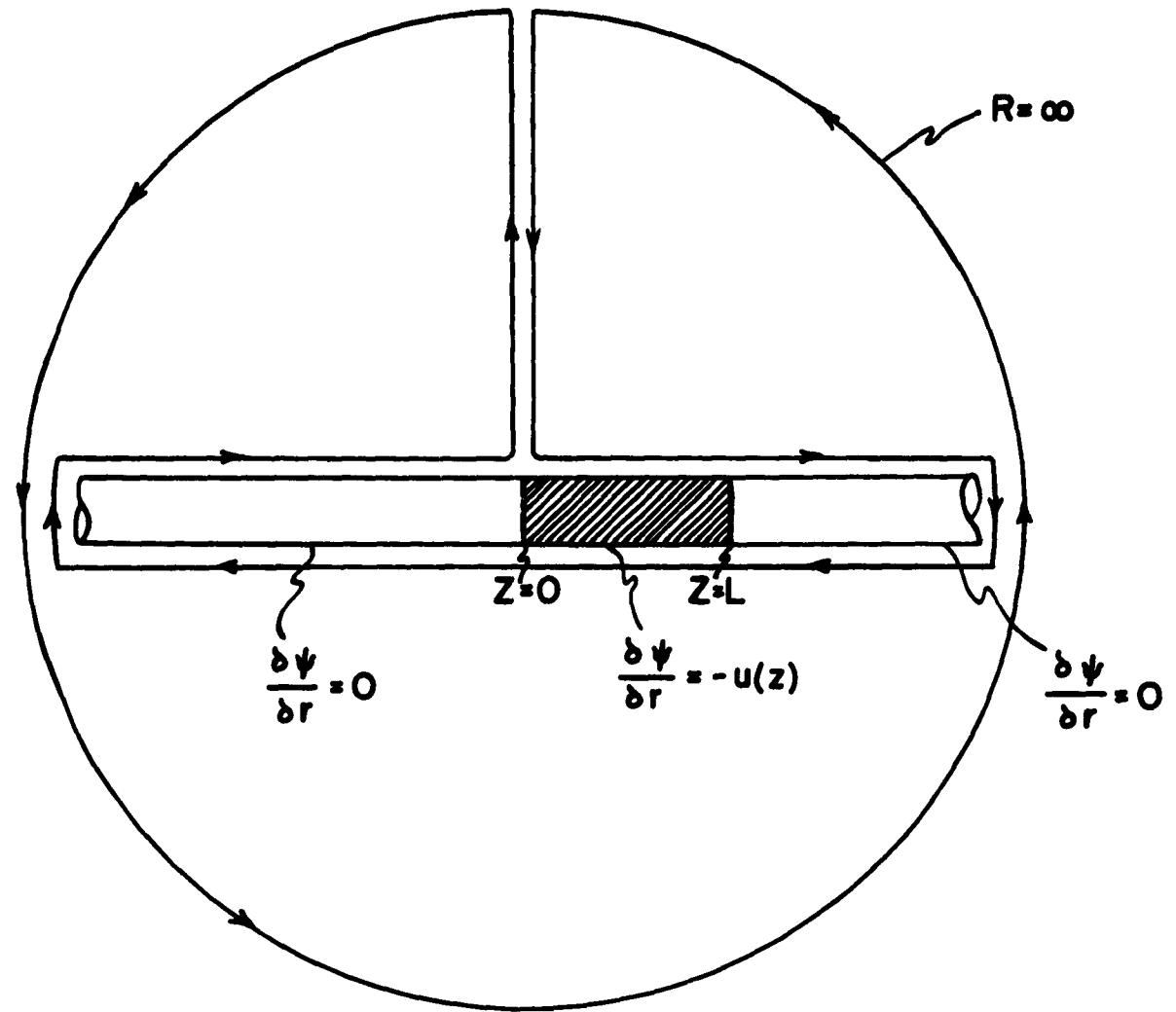
$$\begin{aligned} & \int_V [G(\bar{R}', \bar{R})(\nabla'^2 + k_0^2)\psi(\bar{R}') - \psi(\bar{R}')(\nabla'^2 + k_0^2)G(\bar{R}', \bar{R})] dV' \\ &= \int_S [G(\bar{R}', \bar{R}) \frac{\partial \psi(\bar{R}')}{\partial n'} - \psi(\bar{R}') \frac{\partial G(\bar{R}', \bar{R})}{\partial n'}] dS', \end{aligned} \quad (A.4)$$

where  $n'$  is the outward normal to the boundary of the region of integration, i.e., the normal pointing toward the cylindrical axis. The volume integral includes all space except the cylinder of radius  $a$ . The surface integral covers the cylindrical surface and a sphere of infinite radius, as well as the two adjoining surfaces linking the cylinder and the sphere (cf. Fig. A.1). By virtue of the radiation condition stated in the second of Eqs. (A.3), the surface integral over the infinite sphere is negligible. Since  $\psi(\bar{R}')$  satisfies the homogeneous Helmholtz equation (A.1), the first term of the volume integral is zero. Taking the above remarks into account, and substituting the first of Eqs. (A.3) in the integrand of the volume integral, Green's theorem now becomes

$$\begin{aligned} \int_V \psi(\bar{R}') \delta(\bar{R}' - \bar{R}) dV' &= a \int_{-\infty}^{\infty} \int_0^{2\pi} [-G(\bar{R}', \bar{R}) \frac{\partial \psi(\bar{R}')}{\partial r'} + \\ &\quad + \psi(\bar{R}') \frac{\partial G(\bar{R}', \bar{R})}{\partial r'}] \Big|_{r'=a} d\phi' dz' \end{aligned} \quad (A.5)$$

The volume integral integrates to  $\psi(\bar{R})$ . Turning to the surface integral, it is noted that  $[\frac{\partial \psi}{\partial r'}]_{r'=a}$  is given, Eq. (A.2) while  $[\psi(\bar{R}')]_{r'=a}$  is not known. It is therefore convenient to select a Green's function whose derivative vanishes on the cylindrical surface, thus eliminating from the surface integral in Eq. (A.5) the product involving the unknown boundary value of the potential, i.e.,  $[\psi(\bar{R}')]_{r'=a}$ . Hence, the Green's function sought must satisfy not only Eqs. (A.3) but also the boundary condition

$$[\frac{\partial G(\bar{R}', \bar{R})}{\partial r'}]_{r'=a} = 0 \quad (A.6)$$



$$\psi = (\bar{R}) = -a \int_0^{2\pi} \int_0^L G(\bar{R}', \bar{R}) u(\phi', z') dz' d\phi'$$

Fig. A.1. Path of integration of the surface integral in the statement of Green's theorem in Eq. A.5. The value of the integral is negligible over the infinite sphere, by virtue of the radiation condition; it is zero over the unshaded portions of the cylinder where the integrand vanishes by virtue of the homogeneous boundary conditions prevailing in this region; the two integrals over the two neighboring surfaces linking the sphere to the cylinder are of opposite sign, and therefore cancel.

Turning to Fig. A.1, it is seen that the surface integral vanishes (1) over the sphere of infinite radius, from the radiation condition; (2) over the adjoining surfaces linking the cylinder to the sphere, because the respective contributions to the integral are of opposite sign; and (3) over that portion of the cylindrical surface where homogeneous boundary conditions prevail. Hence, Green's theorem finally becomes, after substitution of the boundary condition Eq. (A.2), and making use of the definition of the Dirac delta function to evaluate the volume integral:

$$\Psi(\bar{R}) = a \int_0^L \int_0^{2\pi} G(\bar{R}', \bar{R})_{r'=\bar{a}} u(\phi', z') d\phi' dz' \quad (A.7)$$

This integral represents the formal solution of the problem.

Turning now to the actual derivation of the Green's function, the first of Eqs. (A.3) is written more explicitly in terms of cylindrical coordinates:

$$\begin{aligned} & \left[ \frac{1}{r} \frac{\partial}{\partial r} (r \frac{\partial}{\partial r}) + \frac{1}{r^2} \frac{\partial^2}{\partial \phi'^2} + \frac{\partial^2}{\partial z'^2} + k_o^2 \right] G(r, r', \phi - \phi', z - z') = \\ & = - \frac{\delta(r - r')}{r} \delta(\phi - \phi') \delta(z - z') \end{aligned} \quad (A.8)$$

Multiplying both sides of this equation by  $e^{j\zeta z}$ , and integrating over all values of  $z$ , this becomes

$$\left[ \frac{1}{r} \frac{\partial}{\partial r} (r \frac{\partial}{\partial r}) + \frac{1}{r^2} \frac{\partial^2}{\partial \phi'^2} + k_o^2 - \zeta^2 \right] G(r, r', \phi - \phi') = \frac{\delta(r - r')}{r} \delta(\phi - \phi') \quad (A.9)$$

where

$$G(r, r', \phi - \phi', \zeta) = \int_{-\infty}^{\infty} G(r, r', \phi - \phi', z) e^{j\zeta z} dz \quad (A.10)$$

is the Fourier transform of the Green's function. This transform is now expanded in a Fourier series in  $\phi$ :

$$G(r, r', \phi - \phi', \zeta) = \frac{1}{2\pi} \sum_{m=-\infty}^{\infty} e^{-jm(\phi - \phi')} G_m(r, r', \zeta) \quad (A.11)$$

Substituting this expression in Eq. (A.9), multiplying both sides by  $e^{+jmr\delta}$ , and integrating with respect to  $\phi$  from 0 to  $2\pi$ , the differential equation finally becomes

$$\left[ \frac{1}{r} \frac{d}{dr} \left( r \frac{d}{dr} \right) + k_o^2 - \zeta^2 - \frac{m^2}{r^2} \right] G_m(r, r', \zeta) = - \frac{\delta(r-r')}{r} \quad (A.12)$$

When  $r \neq r'$ ,  $G$  satisfies Bessel's equation. To represent outgoing waves,  $G_m$  must be a combination of Hankel and Bessel functions (5). A particular combination of these functions which satisfies Eq. (A.6) and, of course, Eqs. (A.3), is of the form

$$G_m(r, r', \zeta) = A_m H_m^{(2)}(\sqrt{k_o^2 - \zeta^2} r) [H_m^{(2)*}(\sqrt{k_o^2 - \zeta^2} a) J_m(\sqrt{k_o^2 - \zeta^2} r') - H_m^{(2)}(\sqrt{k_o^2 - \zeta^2} r') J_m(\sqrt{k_o^2 - \zeta^2} a)] \quad (A.13)$$

where  $r >$ ,  $r <$  denote the larger and smaller of the coordinates  $r, r'$  respectively. The coefficient  $A_m$  is determined from the condition that  $G$  must represent a unit source.  $G_m(r, r', \zeta)$  satisfies Eq. (A.12) which is of the standard form: \*

$$\left\{ \frac{d}{dr} [p(r) \frac{d}{dr} - q_+(r)] G_m \right\} = - \delta(r-r') \quad (A.14)$$

where in the present case,  $p(r) = r$ . The corresponding unit source condition is

$$\left. \frac{dG_m}{dr} \right|_{r=r'-0}^{r=r'+0} = - \frac{1}{p(r')} \quad (A.15)$$

The two values of the derivative which appear in this difference are obtained from Eq. (A.13):

$$\begin{aligned} \frac{\partial G}{\partial r} = A_m \sqrt{k_o^2 - \zeta^2} H_m^{(2)}(\sqrt{k_o^2 - \zeta^2} r') [H_m^{(2)*}(\sqrt{k_o^2 - \zeta^2} a) J_m(\sqrt{k_o^2 - \zeta^2} r') - \\ H_m^{(2)}(\sqrt{k_o^2 - \zeta^2} r') J_m(\sqrt{k_o^2 - \zeta^2} a), \text{ for } r = r' = r'_+ \end{aligned}$$

\*For a discussion of this equation and of Green's functions see, for example, reference 19.

$$\frac{\partial G}{\partial r} = A_m \sqrt{k_o^2 - \zeta^2} H_m^{(2)}(\sqrt{k_o^2 - \zeta^2} r') [H_m^{(2)'}(\sqrt{k_o^2 - \zeta^2} a) J_m'(\sqrt{k_o^2 - \zeta^2} r') - \\ H_m^{(2)'}(\sqrt{k_o^2 - \zeta^2} r') J_m'(\sqrt{k_o^2 - \zeta^2} a)], \text{ for } r = r' \leq a$$

(A.16)

Substituting these values in Eq. (A.15), and setting  $p(r') = r'$ , the unit source condition can be stated as follows:

$$\frac{dG_m}{dr} \begin{cases} r=r'+0 \\ r=r'-0 \end{cases} = A_m \sqrt{k_o^2 - \zeta^2} H_m^{(2)}(\sqrt{k_o^2 - \zeta^2} a) [H_m^{(2)}(\sqrt{k_o^2 - \zeta^2} r') J_m'(\sqrt{k_o^2 - \zeta^2} r') - \\ H_m^{(2)'}(\sqrt{k_o^2 - \zeta^2} r') J_m(\sqrt{k_o^2 - \zeta^2} r')] = -\frac{1}{r}. \quad (A.17)$$

After substitution of the identity

$$H_m^{(2)'}(x) J_m(x) - J_m'(x) H_m^{(2)}(x) = -\frac{2j}{\pi x} \quad (A.18)$$

Equation (A.17) can be solved for  $A_m$ :

$$A_m = \frac{-j\pi}{2H_m^{(2)'}(\sqrt{k_o^2 - \zeta^2} a)} \quad (A.19)$$

This determines the transform  $G_m$ , and hence  $G(\bar{R}, \bar{R}')$ . Combining Eqs. (A.10), (A.11) and (A.19) the Green's function can be written in the form of inverse Fourier transforms:

$$G(\bar{R}, \bar{R}') = -\frac{j}{8\pi} \sum_{m=-\infty}^{\infty} e^{-jm(\phi-\phi')} \int_{-\infty}^{\infty} \frac{H_m^{(2)}(\sqrt{k_o^2 - \zeta^2} r')}{H_m^{(2)'}(\sqrt{k_o^2 - \zeta^2} a)} [H_m^{(2)'}(\sqrt{k_o^2 - \zeta^2} a) J_m(\sqrt{k_o^2 - \zeta^2} r') - \\ H_m^{(2)}(\sqrt{k_o^2 - \zeta^2} r') J_m'(\sqrt{k_o^2 - \zeta^2} a)] e^{-j\zeta(z-z')} d\zeta \quad (A.20)$$

Specializing this expression for the cylindrical surface ( $r' = a$ ), we can set  $r' = r \leq a$  and  $r' = r \geq a$ . When the term in brackets is rewritten by means of

the relation in Eq. (A.18), the Green's function  $[G(R, R')]_{r'=a}$  can be stated as

$$G(R, R') \Big|_{r'=a} = -\frac{1}{4\pi^2 a} \sum_{m=-\infty}^{\infty} e^{-jm(\phi-\phi')} \int_{-\infty}^{\infty} \frac{e^{-j\zeta(z-z')}}{\sqrt{k_o^2 - \zeta^2}} \frac{H_m^{(2)}(\sqrt{k_o^2 - \zeta^2} r)}{H_m^{(2)'}(\sqrt{k_o^2 - \zeta^2} a)} d\zeta. \quad (A.21)$$

This Fourier integral can be readily evaluated in the distant field only, i.e. for large values of  $|R|$ . Using the asymptotic expression for the Hankel function of large argument,

$$H_m^{(2)}(\sqrt{k_o^2 - \zeta^2} r) \rightarrow j^m e^{j\frac{\pi}{4}} \sqrt{\frac{2}{\pi r}} \frac{e^{-j\sqrt{k_o^2 - \zeta^2} r}}{(k_o^2 - \zeta^2)^{\frac{1}{4}}}, \text{ as } r \rightarrow \infty, \quad (A.22)$$

the expression for the Green's function now becomes:

$$G(\bar{R}, \bar{R}') \Big|_{r'=a} = -\frac{e^{j\frac{\pi}{4}}}{4\pi^2 a} \sqrt{\frac{2}{\pi r}} \sum_{m=-\infty}^{\infty} e^{-jm(\phi-\phi')} j^m \int_{-\infty}^{\infty} \frac{\exp\{-j[\zeta(z-z') + \sqrt{k_o^2 - \zeta^2} r]\}}{(k_o^2 - \zeta^2)^{\frac{3}{4}} H_m^{(2)'}(\sqrt{k_o^2 - \zeta^2} a)} d\zeta \quad (A.23)$$

In studying the distant field it is expedient to switch to spherical coordinates. Hence

$$\begin{aligned} r &= R \sin \theta, \\ z-z' &= R \cos \theta, \end{aligned} \quad (A.24)$$

where  $R$  is measured from the point ( $z = 0, r = 0$ ), and where it is assumed that the length of the source is negligible compared to  $R$ . When these transformations are substituted in Eq. (A.23) the expression for the Green's function finally becomes:

$$\begin{aligned} G(\bar{R}, \bar{R}') \Big|_{r'=a} &= -\frac{e^{j\frac{\pi}{4}}}{4\pi^2 a} \sqrt{\frac{2}{\pi R \sin \theta}} \sum_{m=-\infty}^{\infty} e^{-jm(\phi-\phi')} j^m \\ &\int_{-\infty}^{\infty} \frac{\exp[-jR(\zeta \cos \theta + \sqrt{k_o^2 - \zeta^2} \sin \theta)]}{(k_o^2 - \zeta^2)^{\frac{3}{4}} H_m^{(2)'}(\sqrt{k_o^2 - \zeta^2} a)} d\zeta. \end{aligned} \quad (A.25)$$

The integral in this expression is of the form

$$I = \int_{-\infty}^{\infty} \Phi(\zeta) e^{-j\Theta'(\zeta, R)} d\zeta \quad (A.26)$$

This type can be readily evaluated by the method of stationary phase which will be applied here without discussing its implications (for further details of reference 20). Comparing Eqs. (A.25) and (26), it is seen that

$$\begin{aligned} \Phi(\zeta) &= [(k_0^2 - \zeta^2)^{\frac{3}{2}} H_m^{(2)}'(\sqrt{k_0^2 - \zeta^2} a)]^{-1} \\ \Theta(\zeta, R) &= R(\zeta \cos \theta + \sqrt{k_0^2 - \zeta^2} \sin \theta) \end{aligned} \quad (A.27)$$

The phase angle  $\Theta(\zeta, R)$  takes on a stationary value when its derivative

$$\frac{d\Theta}{d\zeta} = R[\cos \theta - \zeta(k_0^2 - \zeta^2)^{-\frac{1}{2}} \sin \theta] \quad (A.28)$$

vanishes, i.e. when

$$\zeta(R) = \bar{\zeta}(R) = k_0 \cos \theta. \quad (A.29)$$

This stationary value  $\Theta[\bar{\zeta}(R), R]$  of the phase angle, which will be designated by  $S(R)$ , is obtained by substituting  $\bar{\zeta}(R)$  in the latter of the two functions in Eq. (A.27):

$$S(R) = R k_0 \quad (A.30)$$

The corresponding value of the amplitude  $\Phi(\zeta)$  of the integrand is

$$\Phi(\bar{\zeta}) = (k_0 \sin \theta)^{-\frac{3}{2}} [H_m^{(1)}'(k_0 a \sin \theta)]^{-1} \quad (A.31)$$

An integral of the type given in Eq. (A.26) can be proved to be approximately equivalent to the complex quantity

$$I[R, T(R)] = e^{j\frac{\pi}{4}} \sqrt{\frac{2\pi}{T(R)}} \Phi(\bar{\zeta}) e^{-jS(R)} \quad (A.32)$$

where the function  $T(R)$  is defined as

$$T(R) = -\frac{8}{\delta^2} \frac{\Phi(\bar{\zeta})}{\bar{\zeta}} \quad (A.33)$$

For our integral, this is found to be, after some manipulation,

$$T(R) = \frac{R}{k_o \sin \theta} \quad (A.34)$$

Substituting this quantity, as well as  $\theta(\zeta)$  and  $S(R)$ , in equation (A.32), the integral becomes

$$I[R, T(R)] = e^{\frac{j\pi}{4}} \sqrt{\frac{2\pi}{R \sin \theta}} \frac{e^{-jk_o R}}{k_o H_m^{(2)}(k_o a \sin \theta)} \quad (A.35)$$

When this expression is substituted in Eq. (A.25), an explicit and quite simple expression for the Green's function in the distant field is finally obtained:

$$G(\bar{R}, \bar{R}') \Big|_{r'=a} = -\frac{j^{m+1}}{2\pi a} \frac{e^{-jk_o R}}{k_o R \sin \theta} \sum_{m=-\infty}^{\infty} \frac{e^{-jm(\phi-\phi')}}{H_m^{(2)}(k_o a \sin \theta)}, \text{ for large } |\bar{R}|. \quad (A.36)$$

It can be verified that this function satisfies Eqs. (A.3).

### Evaluation of the Distant Field

In order to evaluate the distant field, Eq. (A.21) for the Green's function is substituted in the formal expression, Eq. (A.7), of the distant field:

$$\psi(\bar{R}) = -\frac{1}{4\pi} \int_{-\infty}^{\infty} \int_{-\infty}^{\infty} \int_0^{2\pi} u(\phi', z') \sum_{m=-\infty}^{\infty} e^{-jm(\phi-\phi')} \frac{e^{-j\zeta(z-z')}}{\sqrt{k_o^2 - \zeta^2}} \frac{H_m^{(2)}(\sqrt{k_o^2 - \zeta^2} r)}{H_m^{(2)}(\sqrt{k_o^2 - \zeta^2} a)} d\phi' dz' d\zeta. \quad (A.37)$$

The function  $u(\phi', z')$  is now expanded as a Fourier series in  $\phi'$ :

$$\hat{u}(\phi', z') = \sum_{m=-\infty}^{\infty} a_m e^{-jm\phi'} \hat{u}_m(z') \quad (A.38)$$

The integration with respect to  $\phi'$  in Eq. (A.37) can now readily be performed by using the relation

$$\int_0^{2\pi} \dot{u}(\phi', z') e^{j m \phi'} d\phi' = 2\pi a_m \dot{u}_m(z') \quad (\text{A.39})$$

The integration with respect to  $z'$  is performed by noting that the Fourier transform  $\dot{u}_m(z')$  is given by the integral

$$\dot{u}_m(\zeta) = \int_{-\infty}^{\infty} \dot{u}_m(z') e^{j \zeta z'} dz' \quad (\text{A.40})$$

The expression (A.37) for the distant field is now reduced to a simple Fourier integral:

$$\psi(\bar{R}) = -\frac{1}{2\pi} \sum_{m=-\infty}^{\infty} a_m e^{-jm\phi} \int_{-\infty}^{\infty} \dot{u}_m(\zeta) \frac{e^{-j\zeta z}}{\sqrt{k_o^2 - \zeta^2}} \frac{H_m^{(2)}(\sqrt{k_o^2 - \zeta^2} r)}{H_m^{(2)'}(\sqrt{k_o^2 - \zeta^2} a)} d\zeta \quad (\text{A.41})$$

Using, as above, the asymptotic expression for the Hankel functions and spherical, instead of cylindrical, coordinates, the expression for the distant field finally becomes:

$$\begin{aligned} \psi(\bar{R}) = & -\frac{e^{j\pi/4}}{\pi} \frac{1}{\sqrt{2\pi R \sin \theta}} \sum_{m=-\infty}^{\infty} a_m j^m e^{-jm\phi} \int_{-\infty}^{\infty} \frac{\dot{u}_m \zeta}{(k_o^2 - \zeta^2)^{\frac{3}{2}} H_m^{(2)'}(\sqrt{k_o^2 - \zeta^2} a)} \\ & \exp \left\{ -jR[\zeta \cos \theta + \sqrt{k_o^2 - \zeta^2} \sin \theta] \right\} d\zeta, \text{ for large } |\bar{R}| \quad (\text{A.42}) \end{aligned}$$

This integral is again of the form (A.26). The only difference between the integral in Eq. (A.42) and the one in Eq. (A.25) is that in the former the amplitude of the integrand is multiplied by  $\dot{u}_m(\zeta)$ . It is seen from Eq. (A.32) that the value of the integral must be the same as that of the integral in Eq. (A.25), except for the fact that it is multiplied by  $\dot{u}_m(\zeta) = u_m(k_o \cos \theta)$ . Substituting this expression for the integral in Eq. (A.42), the value of the distant field is then finally found to be:

$$\psi(\bar{R}) = -\frac{j e^{-jk_o R}}{\pi k_o R \sin \theta} \sum_{m=-\infty}^{\infty} \frac{j^m a_m e^{-jm\phi} \dot{u}_m(k_o \cos \theta)}{H_m^{(2)'}(k_o a \sin \theta)}, \text{ for large } |\bar{R}| \quad (\text{A.43})$$

This potential function is related to the sound pressure as follows:

$$p(\bar{R}) = j\omega \rho_0 \psi(\bar{R}) \quad (\text{A.44})$$

The pressure field can now be computed for the proper radial velocity distribution on the cylindrical surface.

### Bibliography

N. B. The theory of the end-fire source has been developed in a series of Internal Reports of this Laboratory dated 26 January 1953, 16 February 1953, 28 April 1953, 28 April 1953, and 21 September 1953. The experimental data were presented in a series of talks given in March 1954 at the Naval Research Laboratory, Washington, D. C., the U.S.N. Underwater Sound Laboratory, Fort Trumbull, Connecticut, the Hudson Laboratories, Dobbs Ferry, New York; they were also discussed in condensed form at the Spring 1954 meeting of the Acoustical Society of America, New York, New York (paper no. N3, "An End-Fire Source," cf. synopsis in J. Acoust. Soc. Am., 26 (September 1954)).

1. M. C. Junger, "The Physical Interpretation of the Expression for an Outgoing Wave in Cylindrical Coordinates," J. Acoust. Soc. Am., 25, 40 (1953).
2. L. Cremer, "Theorie der Schalldämmung dünner Wände bei Schrägem Einfall," Akust. Z. 7, 81 (1942).
3. H. Kolsky, Stress Waves in Solids, (Clarendon Press, Oxford, 1953).
4. D. T. Laird and H. Cohen, "Directivity Patterns for Acoustic Radiation from a Source on a Rigid Cylinder," J. Acoust. Soc. Am., 24, 46 (1952).
5. H. Levine and J. Schwinger, "On the Radiation of Sound from an Unflanged Circular Pipe," Phys. Rev. 73, 383 (1948).
6. C. H. Papas, "Radiation from a Transverse Slot in an Infinite Cylinder," J. Math. Phys. 28, 227 (1950).
7. P. M. Morse, Vibration and Sound, (McGraw-Hill Book Co., New York, 1948).
8. R. M. Davies, "A Critical Study of the Hopkinson Pressure Bar," Trans. Royal Soc. (London) Series A, 240, 375 (1948).
9. A. N. Holden, "Longitudinal Modes of Elastic Waves in Isotropic Cylinders and Slabs," The Bell System Technical Journal 30, 956 (1951).
10. E. Giebe and E. Blechschmidt, "Experimentelle und Theoretische Untersuchungen Über Dehnungsschwingungen von Stäben und Röhren," Ann. Phys. 18, 417 (1933).

11. M. C. Junger and F. J. Rosato, "The Propagation of Elastic Waves in Thin-Walled Cylindrical Shells," *J. Acoust. Soc. Am.* 26, 709 (1954).
12. W. J. Thomson, "Transmission of Pressure Waves in Liquid Filled Tubes," *Proc. First National Congress Appl. Mech. (A.S.M.E.)*, New York, N. Y., 1953) pp. 927-933.
13. W. Kuhl, "Die Eigenschaften wassergefüllter Rohre für Widerstands- und Schallgeschwindigkeitsmessungen," *Acustica* 3, 111 (1953).
14. M. C. Junger, "The Effect of a Surrounding Fluid on Pressure Waves in a Fluid-Filled Elastic Tube," to be published in *J. Appl. Mech.* Paper no. 54-A-93, presented at Fall 1954 meeting of A.S.M.E. in New York, N. Y.
15. M. C. Junger, "Wave Propagation in Fluid-Filled Tubes," paper M9 to be presented at the Fall 1954 meeting of the Acoustical Society of America in Austin, Texas. *Synopsis J. Acoust. Soc. Am.* 27, 211 (1955).
16. V. A. Del Grosso and E. J. Smura, "Materials Suitable for Sound Applications," *Naval Research Laboratory, Report 4191* (Sept. 18, 1953).
17. M. C. Junger, "Radiation Loading of Cylindrical and Spherical Surfaces," *J. Acoust. Soc. Am.*, 24, 288 (1952).
18. K. Goesele, "Schallabstrahlung von Platten, Die zu Biegeschwingungen Angeregt Sind," *Acustica* 3, 243 (1953).
19. R. Courant and D. Hilbert, Methoden der Mathematischen Physik (Julius Springer, Berlin, 1931, Vol. I, Section V.14).
20. C. Eckart, "The Approximate Solution of One-Dimensional Wave Equations," *Rev. Modern Phys.* 20, 399 (1948).

Distribution

Chief of Naval Research  
Acoustics Branch (Code 411)  
Washington 25, D. C. (2 copies)

Director  
Naval Research Laboratory  
Technical Information Officer  
Washington 25, D. C. (6 copies)

Commanding Officer  
Office of Naval Research  
1030 E. Green Street  
Pasadena 1, California (1 copy)

Commanding Officer  
Office of Naval Research  
10th Floor  
The John Crerar Library Building  
86 E. Randolph Street  
Chicago 1, Illinois (1 copy)

Commanding Officer  
Office of Naval Research  
346 Broadway  
New York 13, N. Y. (1 copy)

Commanding Officer  
Office of Naval Research  
150 Causeway Street  
Boston, Mass. (1 copy)

Commanding Officer  
Office of Naval Research  
1000 Geary Street  
San Francisco, California (1 copy)

Commanding Officer  
Office of Naval Research  
Navy #100, Fleet Post Office  
New York, N. Y. (2 copies)

Office of Technical Services  
Department of Commerce  
Washington, D. C. (1 copy)

Armed Services Technical  
Information Agency  
Document Service Center  
Knott Building  
Dayton 2, Ohio (5 copies)

Commander  
U. S. Naval Ordnance Laboratory  
Sound Division  
White Oak, Maryland (1 copy)

Director  
U. S. Navy Underwater Sound  
Reference Laboratory  
P. O. Box 3629  
Orlando, Florida (1 copy)

Commanding Officer and Director  
U. S. Navy Electronics Laboratory  
San Diego 52, California (1 copy)

Commanding Officer and Director  
U. S. Navy Underwater  
Sound Laboratory  
Fort Trumbull  
New London, Connecticut (1 copy)

Commander  
Naval Air Development Center  
Johnsville, Pennsylvania (1 copy)

Chief  
Bureau of Ships (Code 847)  
Navy Department  
Washington 25, D. C. (1 copy)

National Bureau of Standards  
Sound Section  
Washington, D. C. (1 copy)

Office of the Chief Signal Officer  
Signal Corps  
Pentagon  
Washington 25, D. C. (1 copy)

David Taylor Model Basin  
Carderock, Maryland (1 copy)

Superintendent  
U. S. Navy Postgraduate School  
Physics Department  
Monterey, California  
Attn: Prof. L. E. Kinsler (1 copy)

Commanding Officer  
Air Force Cambridge Research  
Laboratory  
230 Albany Street  
Cambridge 39, Mass. (1 copy)

Distribution (cont'd)

National Science Foundation  
1520 H Street, N. W.  
Washington, D. C. (1 copy)

The Catholic University of America  
Department of Physics  
Washington 17, D. C. (1 copy)

Brown University  
Department of Physics  
Providence 12, Rhode Island (1 copy)

Western Reserve University  
Department of Chemistry  
Cleveland, Ohio  
Attn: Dr. Ernest Yeager (1 copy)

Massachusetts Institute of Technology  
Acoustics Laboratory  
Cambridge 39, Massachusetts (1 copy)

Princeton University  
Department of Electrical Engineering  
Princeton, New Jersey (1 copy)

University of California  
Department of Physics  
Los Angeles, California (1 copy)

Chief, Physics Division  
Office of Scientific Research  
Hq., ARDC, P.O. Box 1395  
Baltimore, Maryland (1 copy)

Commanding General  
Wright-Patterson Air Force Base  
Dayton, Ohio (1 copy)

Hudson Laboratories  
Columbia University  
145 Palisades Street  
Dobbs Ferry, New York (1 copy)

Lamont Geological Laboratories  
Columbia University  
Torre Cliffs  
Palisades, New York (1 copy)

Woods Hole Oceanographic Institution  
Woods Hole, Massachusetts  
Attn: Mr. Vine (1 copy)

Director  
Defense Research Laboratory  
University of Texas  
Austin, Texas (1 copy)

Director  
Ordnance Research Laboratory  
The Pennsylvania State University  
State College, Pennsylvania (1 copy)

Bell Telephone Laboratories  
Murray Hill, New Jersey (1 copy)

Los Alamos Scientific Laboratory  
P. O. Box 1663  
Los Alamos, New Mexico  
Attn: Dr. G. L. Campbell (1 copy)

U. S. Atomic Energy Commission  
Library Section  
Technical Information Branch,  
P. O. Box E  
Oak Ridge, Tennessee  
Attn: Dr. I. A. Warheit (1 copy)

Chief, Office of Ordnance Research  
Box CM, Duke Station  
Durham, North Carolina (1 copy)